Dissertation

submitted to the

Combined Faculties of the Natural Sciences and Mathematics

of the Ruperto-Carola-University of Heidelberg, Germany,

for the degree of

Doctor of Natural Sciences

Put forward by

Xudong Gao

born in: Harbin, China

Oral examination: February 6, 2020

LOW-MASS STELLAR EVOLUTION TRACED WITH NON-LTE ABUNDANCES

— Dissertation —

XUDONG GAO

Supervisors:	Dr Karin Lind
	Dr Anish Amarsi
Referees:	Dr Karin Lind
	Prof Dr Norbert Christlieb
Additional Examiners:	Prof Dr Ralf Klessen
	Prof Dr Johanna Stachel

Abstract

The detailed chemical composition of stellar atmospheres can reveal the structure and evolution of the stellar interiors, otherwise hidden from direct site, as well as the structure and evolution of our entire Galaxy. The advent of several large-scale stellar spectroscopic surveys promises breakthroughs in our understanding of the physical processes that shape stellar surface abundances. However, the full potential of these extremely large and precise surveys is not yet being reached, as standard elemental abundance determinations today are based on the simplifying and incorrect assumption that the stellar atmosphere is in local thermodynamic equilibrium (LTE).

In this thesis I have employed non-LTE radiative transfer methods to tackle two outstanding astrophysical problems. The first problem is related to the chemical homogeneity in the open clusters, which for example is very important to understand how disrupted clusters have formed the Galactic disk and pinpoint the birth location of field stars. Abundance trends with stellar effective temperature have been found in all the analysed elements, indicating that the chemical abundance varies along with evolutionary phase past the turn-off. The overall agreement between our measured abundance patterns and the predictions by the stellar models with atomic diffusion and mixing, implies that the process of atomic diffusion poses a non-negligible effects during the main-sequence phase, which leads to the inhomogeneities in the abundances of open clusters.

The second problem is related to lithium evolution in low-mass main-sequence stars. The primordial elemental abundances predicted by Standard Big Bang nucleosynthesis (SBBN) generally show good agreement with observations. However, a glaring exception is the cosmic abundance of lithium, which SBBN estimates to be three times higher than what is observed in the atmospheres of metal-poor stars in the Galactic halo (i.e. stars on the so-called Spite Plateau). This long-recognized discrepancy has become known as the Cosmological Lithium Problem. In this thesis, I present observational evidence, based on a state-of-the-art non-LTE spectroscopic analysis of more than 100,000 stars from the large-scale spectroscopic "Galactic

Archaeology with HERMES"(GALAH) survey, that the surface lithium abundances of these Spite Plateau do not in fact reflect their initial (SBBN) lithium abundances; rather, they have been depleted by a factor of three. This further strengthens the case for an astrophysical solution to the cosmological problem, reconciling tension with predictions of the SBBN.

Zusammenfassung

Die detaillierte chemische Zusammensetzung von Sternatmosphären kann die Struktur und Entwicklung der Sterninnern, die dem direkten Betrachter verborgen sind, sowie die Struktur und Entwicklung unserer ganzen Galaxie offenlegen. Das Aufkommen zahlreicher groß angelegter spektroskopischer Durchmusterungen von Sternen verspricht Durchbrüche in unserem Verständnis physikalischer Prozesse, die die Elementhäufigkeiten an der Sternoberfläche beeinflussen. Das vollständige Potential dieser äußerst großen und präzisen Durchmusterungen ist derzeit jedoch noch nicht erreicht, da die derzeit üblicherweise benutzten Bestimmungen der Elementhäufigkeiten auf der vereinfachenden und inkorrekten Annahme beruhen, dass sich die Sternatmosphäre im lokalen thermodynamischen Gleichgewicht (local thermodynamic equilibrium, LTE) befindet.

In der vorliegenden Dissertation habe ich Strahlungstransportmethoden verwendet, die von der Annahme des LTE abweichen (non-LTE), um zwei ausstehende astrophysikalische Probleme anzugehen. Das erste Problem hängt mit der chemischen Homogenität von offenen Sternhaufen zusammen, welche zum Beispiel sehr wichtig ist, um zu verstehen, wie aufgelöste Sternhaufen die galaktische Scheibe geformt haben, und um die Geburtsorte von Feldsternen zu lokalisieren. Tendenzen der Häufigkeit mit der effektiven Temperatur von Sternen wurden für alle untersuchten Elemente gefunden, was darauf hindeutet, dass die chemische Häufigkeit entlang der Evolutionsphase nach dem Abzweigen variiert. Das grundsätzliche Übereinstimmen zwischen unseren gemessenen Häufigkeitsverteilungen und den Vorhersagen von Sternenmodellen mit atomarer Diffusion und Durchmischung zeigt, dass der Prozess der atomaren Diffusion einen nicht vernachlässigbaren Effekt während der Hauptreihenphase darstellt, welcher zu Inhomogenitären in den Elementhäufigkeiten offener Sternhaufen führt.

Das zweite Problem befasst sich mit der Entwicklung von Lithium in Hauptreihensternen mit geringer Masse. Die ursprüngliche Elementhäufigkeit, die durch die Standard Big Bang Nukleosynthese (SBBN) vorhergesagt wird, zeigt gerell eine gute Übereinstimmung mit den Beobachtungen. Die komsiche Elementhäufigkeit

von Lithium ist jedoch eine eklatante Ausnahme, da die SBBN diese drei mal höher bestimmt als Beobachtungen in Sternatmosphären von metal-armen Sternen der galaktischen Halo (d.h. Sternen entlang des sogenannten Spite-Plateaus). Diese langzeit bekannte Diskrepanz ist als das Kosmologische Lithium Problem bekannt geworden. In dieser Dissertation präsentiere ich empirische Beweise, die auf hochmodenen spectroskopischen non-LTE Analysen von mehr als 100,000 Sternen der groß angelegten spektroschopischen "Galactic Archaeology with HERMES"(GALAH) Durchmusterung berufen, und zeigen, dass die Oberflächen-Lithiumhäufigkeiten an des Spite-Plateaus in der Tat nicht deren anfängliche (SBBN) Lithiumhäufigkeiten wiederspiegeln; vielmehr wurden sie um das Dreifache erschöpft. Dies bestärkt die Möglichkeit einer astrophysikalischen Lösung des kosmlogischen Problems, indem die Spannungen mit den Vorhersagen der SBBN in Einklang gebacht werden können.

Contents

CONTENTS

CONTENTS

List of Figures

List of Tables

Acknowledgements

My deepest gratitude goes first and foremost to my PhD supervisor Karin Lind, who trust me and gave me this precious chance to study at MPIA. I can still remember the mixed feeling, when I came to the institute on the first day, a bit anxiety and excited. Everything was new to me and I knew nothing. Thanks to her patient guidance and constant encouragement, I feel that I have grown up a lot and learned the scientific thinking from her. I also appreciate all the helpful suggestions on my research from her.

Second, I would like to express my gratitude to Anish Amarsi, who is not only my co-supervisor but also a very good friend to me. Thanks to his enthusiastic help with my research and concern in life, I could have made this far and completed my thesis.

I also would like to thank all the other people in the Lind group: Sven, Ása and Diane. They always gave me great help and advice whenever I came across some problems. I really appreciate to be a member of this creative and lovely group.

Last but not least, I shall extend my thanks to all the other colleagues and IMPRS students at MPIA. It was really a great time to study with them and learn from them in this wonderful institute.

Acknowledgements

Chapter 1

Introduction

1.1 Accurate surface chemical abundances

To most of the astronomers, the only information we collect from stars is the electromagnetic radiation. By breaking up the radiation into its constituent wavelengths we can obtain the typical spectrum. Moreover, many valuable properties of stars, such as their chemical composition, effective temperature, surface gravity, etc., can be derived from analysis of stellar spectra. To decode the stellar spectra and extract reliable information with confidence, it is of considerable importance to construct more realistic stellar atmosphere that can generate an accurate model of emergent spectrum and develop detailed and powerful numerical methods.

1.1.1 Stellar atmosphere

The stellar atmosphere is very important to quantitative spectroscopy, since most of features of the stellar spectrum originate there. Generally, the stellar atmosphere of late-type stars can be divided into several basic layers, i.e. photosphere, chromosphere and corona. It is a plasma composed of many kinds of particles, namely atoms, ions, free electrons, molecules and photons. Note that even for the same species of atoms, ions or molecules, they can have be different due to the different excitation state. To fully describe the system, we need to construct a general distribution function including the kinetics (position and momentum) of all the particles, which will have enormous unknown parameters to be determined. To reduce the complexity of the problem and provide the most general dynamics of a stellar atmosphere, one can simply consider the moments of the distribution

function, resulting in the usual hydrodynamic equations (see e.g. Mihalas & Mihalas 1984; Castor 2004). However, it is still extremely complex to be fully solved in most cases. To further simplify the problem, one can consider the stellar atmosphere as a stationary (i.e. $\partial/\partial t = 0$) and static medium (velocity $= 0$) in a one-dimensional situation (all quantities are in the radial r-coordinate), the transport of energy via convection can be parameterized by the mixing-length theory (see e.g. Mihalas 1978). These are the common assumptions applied in the atmospheric modelling of late-type stars (see e.g. Kurucz 1970; Gustafsson et al. 2008). Then the stellar atmosphere can be characterized by the three equilibrium equations as follow,

$$\frac{\mathrm{d}P}{\mathrm{d}r} = -\rho GM_\star/r^2 \approx -\rho GM_\star/R_\star^2 = -\rho g, \text{hydrostatic equilibrium}, \qquad (1.1)$$

$$F_{rad} + F_{conv} = \sigma T_{\mathrm{eff}}^4, \text{radiative equilibrium}, \qquad (1.2)$$

where P the pressure, ρ the mass density, g the gravity acceleration, F_{rad} the raidiative flux, F_{conv} the convective flux, σ the Stefan-Boltzmann constant and T_{eff} the so-called effective temperature. Based on all the above equations, the gravity acceleration g and the effective temperature T_{eff} are three basic parameters in the problem of the simplified stellar atmosphere.

Another assumption that most atmosphere modelling of late-type stars usually applied is local thermodynamic equilibrium (LTE), which simplifies the problem enormously. In the context of LTE, all the particle distribution functions can be evaluated locally with given temperature and number density (of all excitation and ionization stages for a given chemical composition), characterized by the following three equations:

Maxwellian velocity distribution,

$$f(v)\mathrm{d}v = (m/2\pi kT)^{3/2}\exp(-mv^2/2kT)\mathrm{d}v, \qquad (1.3)$$

where m is the particle mass and k the Boltzmann constant.

Boltzmann excitation equation,

$$n_j/n_i = (g_j/g_i)\exp[-(E_j - E_i)/kT], \qquad (1.4)$$

where g_i is statistical weight of level of i and E_i the excitation energy level.

Saha ionization equation,

$$\frac{N_{I+1}}{N_I} = \frac{(2\pi m_e kT)^{3/2}}{N_e h^3}\frac{2u_{I+1}}{u_I}\exp(\chi_I/kT), \qquad (1.5)$$

where N_I is the total number density of ionization stage I and N_e the electron density; $u_I = \sum_i g_i \exp(-E_i/kT)$ is the partition function of species I; χ_I is the ionization potential of ion I.

In practice, energy levels of atoms/ions can depart from their LTE value, when the radiative rates in the atomic transitions dominate over the collisional rates and the radiation field depart from the equilibrium This is particularly true in the upper layers of photosphere, since the photons significantly escape from a star, breaking down the detailed balance in radiative transition collisions. Conversely, deep in the atmosphere, departures from LTE are insignificant as collision (high particle densities) and radiation (no photons escape) tend to maintain the local equilibrium.

Once the equations describing the particle properties have been determined, the key problem left in the stellar atmosphere modelling is to solve the radiative transfer equation, which can be understood as a kinetic equation for photons, which describes the changes of the radiation field due to the interaction between photons/radiation and particles/matter. In order to construct the equation and describe the processes of interaction between radiation and matter, several quantities will be introduced first:

Specific intensity I_ν: describes the energy transported by radiation/photons with frequencies in the range (ν, $\nu + d\nu$) in a unit time interval t, across a unit area perpendicular to the direction of propagation **n**, into a unit solid angle. The mean intensity of radiation J_ν, can be derived by integrating over the solid angle. (angle-averaged)

Absorption coefficient κ_ν: describes the amount of energy removed from the radiation field (a beam of specific intensity) by particles/matter at unit frequency range, solid angle, area, and time. In addition to the true absorption process, i.e., a photon is absorbed and destroyed from the incident beam, the scattering process also contributes to the absorption coefficient.

Emission Coefficient j_ν: describes the amount of energy released by the material in the form of radiation at unit frequency range, solid angle, area, and time.

In general, there are three types of microscopic processes that induce an absorption and emission of photons: (1) absorption - an absorption of a photon accompanied by a transition of an atom/ion to a higher energy state; (2) spontaneous emission - transition to lower state accompanied by emission of photon with energy corresponding to the energy difference between the atomic/ionic levels; and (3) stimulated emission - an interaction of an atom/ion with a photon accompanied by an emission of another photon with identical properties. Note that a transition

to a lower state also can occur in the case of stimulated emission. The stimulated emission is usually treated as negative absorption.

The general form of the radiative transfer equation in a one-dimensinal plane-parallel atmosphere, assuming a time-dependent situation, then can be expressed as,

$$\mu \frac{dI_\nu}{dr} = j_\nu - \kappa_\nu I_\nu, \tag{1.6}$$

which expresses the difference of specific intensity before and after a radiation beam passing through an elementary volume of matter on the left hand side, and the difference of the energy emitted and absorbed in this volume on the right hand side. Where $\mu \equiv \cos\theta$, θ is the angle between direction of radiation propagation and the normal to the stellar surface. This equation can be changed to an advantageous form by dividing κ_ν,

$$\mu \frac{dI_\nu}{d\tau_\nu} = I_\nu - S_\nu, \tag{1.7}$$

where $d\tau_\nu \equiv -\kappa_\nu dr$ is the optical depth, which can be simply regarded as the e-folding distance for the decay of the specific intensity caused by absorption (may change significantly with frequency); $S_\nu \equiv j_\nu / \kappa_\nu$ is the source function, which represents the radiative energy emitted per unit optical depth. When the system/medium approaches to the thermal equilibrium, such as, in the deep atmosphere, where no photons escape, the source function equals the Planck function ($S_\nu = B_\nu$), where

$$B_\nu = \frac{2h\nu^3}{c^2} \frac{1}{e^{h\nu/kT} - 1} \tag{1.8}$$

Departure from the LTE - A two level atom scheme A two-level atom is the simplest case but provides a good physical understanding of line formation problems in the stellar atmosphere. The source function in a two-level atom can be generally expressed as a linear function of the mean intensities,

$$S_\nu = (1 - \epsilon)\bar{J} + \epsilon B_\nu \tag{1.9}$$

where $\bar{J}$ is frequency-averaged mean intensity of radiation, ϵ can be understood as a destruction probability, i.e., the probability that an absorbed photon is destroyed by the collision process rather than being re-emitted (by spontaneous emission). The first term on the right hand side of the equation stands for the emission following a previous absorption of a photon, while the second term represents the thermal creation of a photon.

Fig. 1.1 shows the source function versus optical depth for a two-level atom in a homogeneous semi-infinite atmosphere. In the context of homogeneous, it means
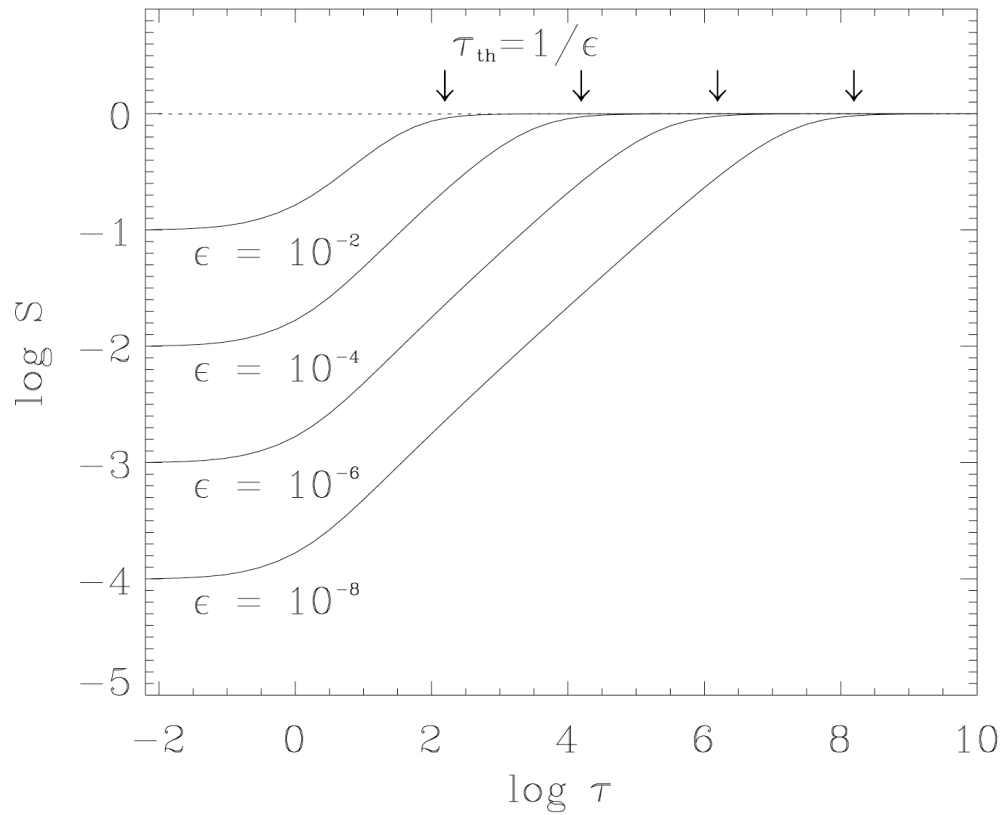
Figure 1.1: **Source function for a two-level atom in a constant property semi-infinite atmosphere, and for various values of the destruction parameters. Figure Credit:** Hubeny & Mihalas (2014)

all the medium properties should be depth-independent. We can see that the source function begin to deviate from the Planck function at a certain depth ($\tau \approx 1/\epsilon$), the point is called the thermalization depth. Below the thermalization depth it is essentially equal to the Planck function B_ν. The source function keeps decreasing above the thermalization depth and is equal to $\epsilon^{1/2}B_\nu$ at the surface.

As mentioned above, the departure from LTE only arise around the boundary/surface due to the escape of photons, making the source function drop down below the Planck function. As the photons start to escape from the surface, all microscopic processes will no longer be balanced. Because the absorption rate strongly depend on the number of photons, whereas the spontaneous emission rate does not. Therefore, the number of radiative excitations will be lower than the number of de-excitations, resulting in the overpopulated in the lower level and underpopulated in the upper level with respect to LTE. However, this still cannot explain the reason why the source function start to deviate from the Planck function in large enough optical depth ($\tau \approx 10^6$).

Escape probability/Intrinsic broadening Let us assume a photon is created at a large optical depth from the surface. The created photon has a frequency near a line center, then we can expect the photon will never escape from the atmosphere, since it will be destroyed by collisional process. However, in reality, the absorption probability is not absolutely equal to 1. The absorption profile $\phi(x)$ is a Voigt function that is a convolution of the natural broadening, collisional broadening (Stark and Van der Waals) and Doppler broadening (thermal motions). It is a sharply peaked function of frequency around $x = 0$.

In a very frequent event of this case, the photon will still make many consecutive scattering with the frequency staying close to the line center; during these scatterings the photon mean free path is too small to make large move in the physical space. However, some infrequent transition can take place when it is re-emitted in the wing of the profile, thus the opacity will drop suddenly and the photon can transfer a large distance. Since the mean optical depth is contributed by the line-wing photons, whose mean free path can vary a lot from the core photons to the wing photons, it is reasonable to understand why the thermalization depth can be so large, which indicates that deviate from LTE can happen in the large optical depth as well. The photon below the thermalization depth ($\tau = 1/\epsilon$) means that after experiencing $1/\epsilon$ scattering, the photon does not escape from the surface and is destroyed by collisional processes.

1.1.2 NLTE line formation

LTE models: LTE is a standard assumption for constructing the stellar atmosphere in the late-type stars. As a result, all atomic level populations can be determined locally by the Saha-Boltzmann equation, Eq. 1.4 and Eq. 1.5; the absorption and emission coefficient can also be expressed as known functions of temperature and electron density (or pressure). Therefore, in the context of LTE, all the stellar parameters can be solved simultaneously based on the basic structural equations (Eq. 1.1 - Eq. 1.7). For example, Gustafsson et al. (2008) published a grid of LTE model atmospheres by the computer program MARCS for late-type stars. For each combination of stellar parameters (T_{eff}, $\log g$ and [Fe/H]), a table of temperature and electron density in all optical depth will be provided.

Why non-LTE is so important in the line formation? However, as mentioned above, departure from LTE (non-LTE) can take place when the radiative rates dominate over the collision rates, which typically becomes significant in the higher photosphere. If the line opacity of a specific element is large, the corresponding observed spectrum will be formed in the high atmosphere where the particle density is low, one can expect the non-LTE effect would be very important to be considered in the line formation. It is important to realize that for any given type of stars, there is always some wavelength range/spectral lines of which non-LTE effect are significant. Therefore if one requires a high accuracy of element abundances in the spectral analysis, the non-LTE effect would be very necessary to be addressed.

How does non-LTE influence the line formation in the atmosphere: We can understand how non-LTE influence the line formation in an extremely simple case of the so-called LTE grey model. The simplification of the model is to assume the absorption coefficient is independent of frequency ($\kappa_\nu \equiv \kappa$). Based on the LTE assumption, $S_\nu = B_\nu = J_\nu$, where the mean intensity J_ν can be understood as the number of photons absorbed at the frequency ν per unit optical depth, and S_ν or B_ν represents the number of photons emitted at the corresponding frequency per unit optical depth.

The radiative equation in the grey atmosphere can be completely and rigorously solved by following the radiative equilibrium ($J = B$), which yields an analytic expression of temperature structure,

$$T(\tau) = [\frac{3}{4}(\tau + \frac{2}{3})]^{\frac{1}{4}} T_{\text{eff}} \tag{1.10}$$

where the temperature in the grey atmosphere varies monotonically as a function of optical depth.

In fact, the mean intensity J_ν does not have to equal to B_ν for all frequencies as the LTE breaks down. Let us consider the extreme case how the low and high frequency region behave in the surface layer of a grey atmosphere ($\tau = 0$). For the high frequency region ($h\nu/kT \gg 1$), Planck function can be written as Wien equation,

$$B_\nu \approx \frac{2h\nu^3}{c^2} e^{-h\nu/kT} \qquad (1.11)$$

For the low frequency region ($h\nu/kT \ll 1$), Planck function can be changed as Rayleigh-Jeans equation,

$$B_\nu \approx \frac{2k\nu^2}{c^2} T \qquad (1.12)$$

The mean intensity at the surface can be derived from the Eddington-Barbier (source function being a linear function of optical depth),

$$J_\nu(\tau = 0) \approx \frac{1}{2} S_\nu(\tau = 1) \qquad (1.13)$$

As the frequency locates in the high/Wien regime, the Planck function, which is very sensitive to T (Eq. 1.10), result in B_ν at the surface will be significantly lower than B_ν at the thick optical depth ($\tau = 1$). On the other hand, the mean intensity J_ν at the surface is approximately a half of $B_\nu(\tau = 1)$ according to Eq. 1.13. Thus, $J_\nu > B_\nu$ in the high frequency regime at the surface, which means that more photons are absorbed than emitted at high frequency ν; in other words, this will result in the so-called superthermal radiation at these wavelengths since the extra absorbed photons increase the internal energy/temperature of the material. In the context of non-LTE, the superthermal radiation will make the number of radiative excitations and ionizations exceed the number of de-excitations and recombinations. It will produce overionization in the lower atomic energy levels to some extent with respect to LTE, while the upper level will be overpopulated. If any spectral line of an element locates in this range, this will result in overexcitation and overionization with respect to LTE and a redistribution of the particles to higher excitation/ionization stages. Spectral lines everywhere that originate from such under-populated lower levels are therefore typically weaker than the LTE assumption would predict and a higher abundance is needed in NLTE to match the same line strength (positive NLTE abundance correction).

Conversely, for low frequencies, the Planck function B_ν is linearly proportional to T and decreases slowly to the surface, leading to $J_\nu < B_\nu$. As a result, more photons are emitted than absorbed at low frequency ν. The subthermal radiation at these wavelengths will cause overpopulation in the lower atomic energy levels to some extent with respect to LTE. In this case, lower non-LTE abundances are

enough to form the same line strength as LTE abundances (Non-LTE abundance correction is negative).

As was discussed above, we can see that in LTE line formation, the two state parameters, i.e., temperature and electron density, are sufficient to describe the physical state at any given position. However, in some situations, the LTE assumption can break down and will yield misleading results without considering non-LTE corrections. Non-LTE effects are tightly related to the temperature structure/ opacity of the chosen element. The non-LTE corrections can behave quite differently at different frequencies even in the same stellar atmosphere.

How to calculate non-LTE line formation: To calculate non-LTE line formation, the atmospheric structure is usually assumed to be known based on previous calculation in LTE and is kept fixed during this procedure. Due to the non-local nature, Saha-Boltzmann equation is not applicable and the population ratios for a chosen atom/ion are determined by the statistical equilibrium,

$$n_i \sum_{j \neq i} (R_{ij} + C_{ij}) = \sum_{j \neq i} n_j (R_{ji} + C_{ji}) \tag{1.14}$$

where R_{ij} and C_{ij} is the radiative and collisional transition rate from energy level i to level j, respectively. The left hand side of the equation represents the total number of transition out of energy level i, while the right hand side stands for the total number of transition into energy level i from all the other possible levels. The problem becomes more numerically complex because all transitions of a given system need to be considered and iteratively solved in Eq. 1.14 together with the equation of radiative transfer. In practice, the populations of energy levels of the studied species are allowed to depart from LTE; the rest of the elements is treated in LTE to simplify the numerical implementation.

1.1.3   Analysis method of observed spectra

Spectrum Synthesis

Spectroscopic analysis is the process of extracting stellar properties from the observed spectra. This involves comparison to synthetic stellar spectra, and the first step is to determine the input physics. It means the basic assumptions that are adopted to describe the medium. In general, for a 1D plane-parallel static atmosphere (hydrostatic and radiative equilibrium), the initial input free parameters are effective temperature (T_{eff}), surface gravity ($\log g$) and chemical compositions. Strictly speaking, the values of all individual chemical species are necessary to

provide. In practice, one usually adopts solar abundances or scale part or all abundances with respect to the solar value.

Generally, due to the deficiency of 1D atmosphere, two more parameters, the so-called microturbulence ξ and macroturbulence v_{mac}, should be used for describing the small and large scales non-thermal motions. They are very convenient parameters to account for the additional broadening caused by the velocity variation in the atmosphere. Their values are constrained by comparing the theoretical predictions and observations. However, a more realistic and fundamental physics assumption should be considered, i.e., 3D hydrodynamic model atmosphere, to get rid of them and increase the accuracy of parameter determinations further. Unfortunately, the 3D hydrodynamic simulations are much more complicated and computational expensive than the 1D hydrostatic simulations. Such modelling is beyond the scope of the present work.

Additionally, one has to take into account the local projected rotational velocity $vv \sin \imath$ as a free parameter, due to its contribution to the rotational broadening effect of the spectrum.

Once the input physics has been determined, the state of equations in stellar atmosphere can be solved by adopting appropriate stellar atmosphere code/ numerical methods. In our project, we use the pre-calculated grid of model atmosphere MARCS (Gustafsson et al. 2008) and take the stellar structure by interpolating the model grid to generate the synthetic spectra.

With all the parameters are specified by the model, i.e., temperature, gas and electron density, and atomic level populations, one can compute the corresponding emergent spectrum with a wavelength-by-wavelength solution of the radiative transfer equation. Note that to be able to compare to the observed spectrum, the final synthetic profile need to undergo a convolution with Doppler broadening by non-thermal large-scale motions and rotational broadening of the star. In reality, instrumental broadening also needs to be convoluted with the net spectrum due to the finite spectrum resolution of a spectrograph.

Spectrum Fitting

The spectrum fitting is the final procedure of picking the synthetic spectrum and finding the best set of stellar parameters that can fit the observed spectrum best. However, there are different ways to perform the actual fitting and approach the final best-fit parameters. In this thesis, we determine and fit all the parameters simultaneously by using a χ^2 fitting procedure, which are proceeding iteratively.

After the initial guess of all the input parameters, the first synthetic profile is produced. In the comparison step, by comparing the selected fitting lines that are sensitive to the changes of stellar parameters, the new values of input parameters are generated for constructing the new model atmosphere state by interpolating the model grid and new synthetic spectrum. This process is repeated until the χ^2 fitting is convergent to some acceptable value.

After extracting stellar parameters from the observed spectrum, one can determine individual element abundances by fitting their absorption lines. In principle, the structure of atmosphere should be constructed and unique for a certain set of chemical composition. In order to be consistent, the same abundances have to be kept when forming the spectrum synthesis. However, some of elements do not influence the state of atmosphere significantly and thus can be changed to any reasonable value. Therefore, when carrying out the analysis of individual element, the stellar parameters can be fixed in this process. Usually, a spectrum will include multiple absorption lines for each element, however, only the absorption features that are strong and not blended by other element lines will be used and fitted simultaneously. More details can be checked in Prieto (2016).

1.2 Mixing processes in low mass stars

From the previous section, we have understood a physics problem in stellar atmosphere modelling that for any type of star spectra there is always a wavelength range where non-LTE effects need to be taken into account. Even though we can construct more realistic stellar atmosphere and develop more detailed numerical methods to improve the accuracy of the predicted spectrum, the surface chemical abundances we obtained from a stellar spectrum are only strictly representative for the evolutionary phase of the star when it was observed. Do surface abundances truly reflect the initial abundances in stars? If not, how do the surface abundances evolve with time in different type of stars?

In standard stellar models, mixing can only be triggered by convection, which makes the predicted surface abundances strongly constrained by a function of stellar mass, composition, and age. There is a general agreement between observations and standard stellar models. However, in some cases, more mixing in these models are expected to explain the data, for instance, the surface lithium abundances in low mass stars. To have a better understanding of the information we decode from the spectra, we need to figure out the possible mixing processes in stars. Since all the projects in this thesis only focus on late-type stars, therefore we only focus on the

mixing in low mass stars here.

1.2.1 Atomic diffusion

Strictly speaking, atomic diffusion belongs to a physical process of element separation rather than mixing process. Heavier elements tend to sink due to the effects of gravitational settling, leading to lower abundances ratios with respect to hydrogen at the surface. Radiative acceleration can lead to the opposite situation, i.e., overabundances at the surface. Michaud (1970) first introduced radiative acceleration and diffusion to explain the abundance anomalies, as discovered by enhanced lines strength of metals in the observed spectra of Ap stars (slow rotating A stars).

Radiative acceleration is caused by the exchange of momentum and energy between the stellar plasma and the radiation field, coming from the interactions between photons and neutral or partially ionized species. One can expect the radiation acceleration to counteract the action of gravity acceleration and drive ions upwards (Richer et al. 1998; Turcotte et al. 1998).

For a given element, to describe how it migrates with respect to others, one needs to determine how gravity and radiative acceleration compete with each other in stars. Assuming a simple 1D plane-parallel atmosphere without considering magnetic field and redistribution of momentum, the radiative acceleration g_{rad} of a given species with atomic weight A_i can be expressed as a integral of all the momentum exchanged with photons by all individual interactions per unit time, divided by the mass of species A_i (Michaud et al. 2015):

$$g_{\mathrm{rad}} = \frac{1}{m_{A_i}c} \int_0^\infty \sigma_\nu F_\nu d\nu \tag{1.15}$$

where $F_\nu d\nu$ represents the net outward radiation flux in the frequency range $d\nu$, $m_{A_i} = A_i m_p$ is the mass of the species and σ_ν is the total absorption cross section, which can be regarded as a combination of all the atomic transitions, i.e., the contributions from bound-bound σ_{bb}, bound-free σ_{bf} and free-free σ_{ff} transitions.

From the above equation, we can see that the radiative acceleration depends on the atomic properties and could be different from ions to ions, depending on thermal conditions and opacity of each ions relative to the total opacity. It could lead to the diffusion process occuring selectively or in different extent for different species/ions. By introducing the radiative acceleration into the diffusion processes, the diffusion

velocity of a trace element with atomic weight A_i and charge Z would be:

$$v_D = D_{ip}[-\frac{\partial \ln c_i}{\partial r} + \frac{A_i m_p}{kT}(g_{\mathrm{rad,i}} - g) + \frac{(Z_i + 1)m_p g}{2kT} + k_T \frac{\partial \ln T}{\partial r}] \qquad (1.16)$$

The velocity is defined as positive in the direction of increasing radius. The first term on the right hand side is the typical chemical diffusion caused by the concentration gradient, which is seldom dominant in stars since the equilibrium abundance gradients are hardly achieved. The second term is the gravitational settling term modified by the radiative acceleration. The third term represents the correction due to the presence of electric field. The forth term is the thermal diffusion because of the temperature gradient in stellar plasma. The dependence on $g_{\mathrm{rad,i}}$ and Z_i shows that the diffusion velocity also varies among ions of a given species.

The (ion-proton) diffusion coefficient D_{ip} usually cannot be expressed accurately by simple analytical expression (Chapman & Cowling 1970), since the medium cannot be assumed fully ionized in a stellar atmosphere. More accurate evaluations from the numerical calculation can be found in recent studies (e.g. Michaud & Proffitt 1993; Richer & Michaud 1993; Thoul et al. 1994; Proffitt 1994).

To obtain a rough estimate of characteristic timescale of atomic diffusion, one can neglect all the terms in Eq.1.16 but gravity, the diffusion velocity turns to be:

$$v_D \approx -g t_D = D_{ip}[\frac{A_i m_p}{kT}(-g)] \qquad (1.17)$$

Then the time to settle gravitationally (t_{sg}) over the distance of one scale height can be estimated as:

$$t_{\mathrm{sg}} = \frac{H}{v_D} \approx \frac{(kT)^2}{g^2 D_{ip} A_i m_p^2} \qquad (1.18)$$

where the scale height $H \approx kT/m_p g$. The g^2 dependence of the timescale is the main factor that makes the diffusion more significant in white dwarfs (Paquette et al. 1986) and neutron stars (Brown et al. 2002) compared to main-sequence stars (Michaud 1977; Turcotte et al. 1998; Michaud et al. 2004). Additionally, the time scale of diffusion would be much shorter for main-sequence stars with shallow convection zones than for giants or main-sequence stars with deep convection zones (Pinsonneault 1997).

Fig. 1.2 shows how the surface abundance vary across the different evolutionary phases calculated by the stellar evolution code MESA with atomic diffusion and extra mixing in the surface layers (Dotter et al. 2017). The extra mixing includes a density dependent turbulent mixing and envelope overshoot mixing. The main difference between the two panels is that the models with radiative acceleration show more significant variations around the turn-off stage than the models without considering
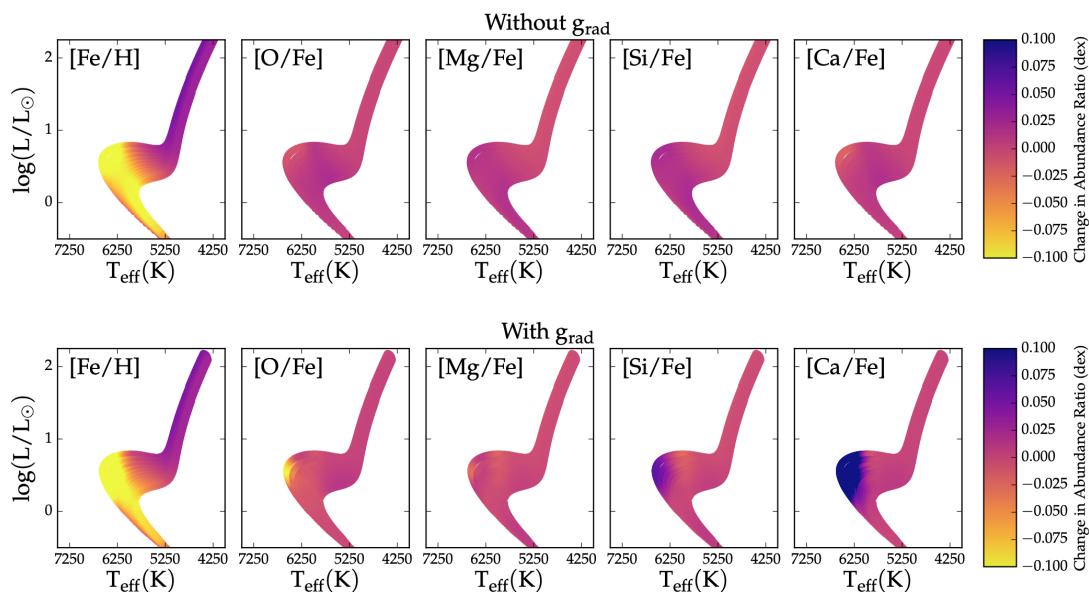
Figure 1.2: **Evolution of surface abundance ratios in the H-R diagram for stellar models with atomic diffusion and turbulent mixing.** The top panel shows stellar models without considering $g_{\rm rad}$ while the bottom panel shows models with $g_{\rm rad}$. All the models start with $[\text{Fe/H}]_{init} = -0.5$ and evolve from 5 to 15 Gyr. The leftmost column shows the variation of Fe with respect to H while the other columns show variation of elements with respect to Fe in different evolutionary phases. **Figure Credit:** Dotter et al. (2017)

radiative acceleration. The models show that surface abundances are modified by diffusion and mixing in radiative regions over the life-time of the star. The largest differences are found around the turn-off point, where the convective envelopes are thinnest, and the initial composition is restored again along with the growth of the convective zone in giants. In other words, stars were born with the same chemical composition, can show different surface abundances in different evolutionary phases. This will complicate chemical tagging, a method that is used to identify the dispersed star clusters through their unique chemical patterns (Dotter et al. 2017).

Stellar age is very important for studies of stellar and galactic evolution (Fuhrmann 2004; Soderblom 2010). The most common method used to estimate stellar age is isochrone fitting, where the measurable physical quantities of stars are compared to age-dependent isochrones from stellar structure models (e.g. Edvardsson et al. 1993; Jørgensen & Lindegren 2005; Maxted et al. 2015). However, the estimated ages from isochrone fitting could have large uncetainties, especially for giant and main-sequence stars. On the other hand, it could result in a biased age estimate due to the imperfection of stellar models. Fig. 1.3 shows the comparison of several computed isochrones from nondiffusive and diffusive models (Michaud et al. 2004). Both sets of models are normalized to the Sun value. It is clear to see that the diffusive isochrones always have cooler turn-offs, fainter subgiant branches and bluer giant branches than those nondiffusive isochrones at the same age. By matching the isochrones from the nondiffusive and diffusive grids with similar turn-off and subgiant luminosities, the reduction in ages from diffusive models can be up to 12%. Since diffusive processes can change stellar structure, which in turn modifies the morphologies of isochrones, therefore, it is necessary to be considered in the determination of stellar ages.

More details about the application of atomic diffusion will be talked about in Chapter 5.

1.2.2 Rotational mixing

Except for microscopic diffusive processes, there are many macroscopic flows that compete with atomic diffusion. It is valuable that stellar models attempt to include such mixing to meet constraints from observed abundance anomalies in stars. Among all of the macroscopic flows, the meridional circulation induced by rotation is widely used in models involving atomic diffusion when the differential rotation can be neglected or very small (Tassoul & Tassoul 1982; Tassoul 2000).

Meridional circulation can be understood by considering a star as a nearly solid
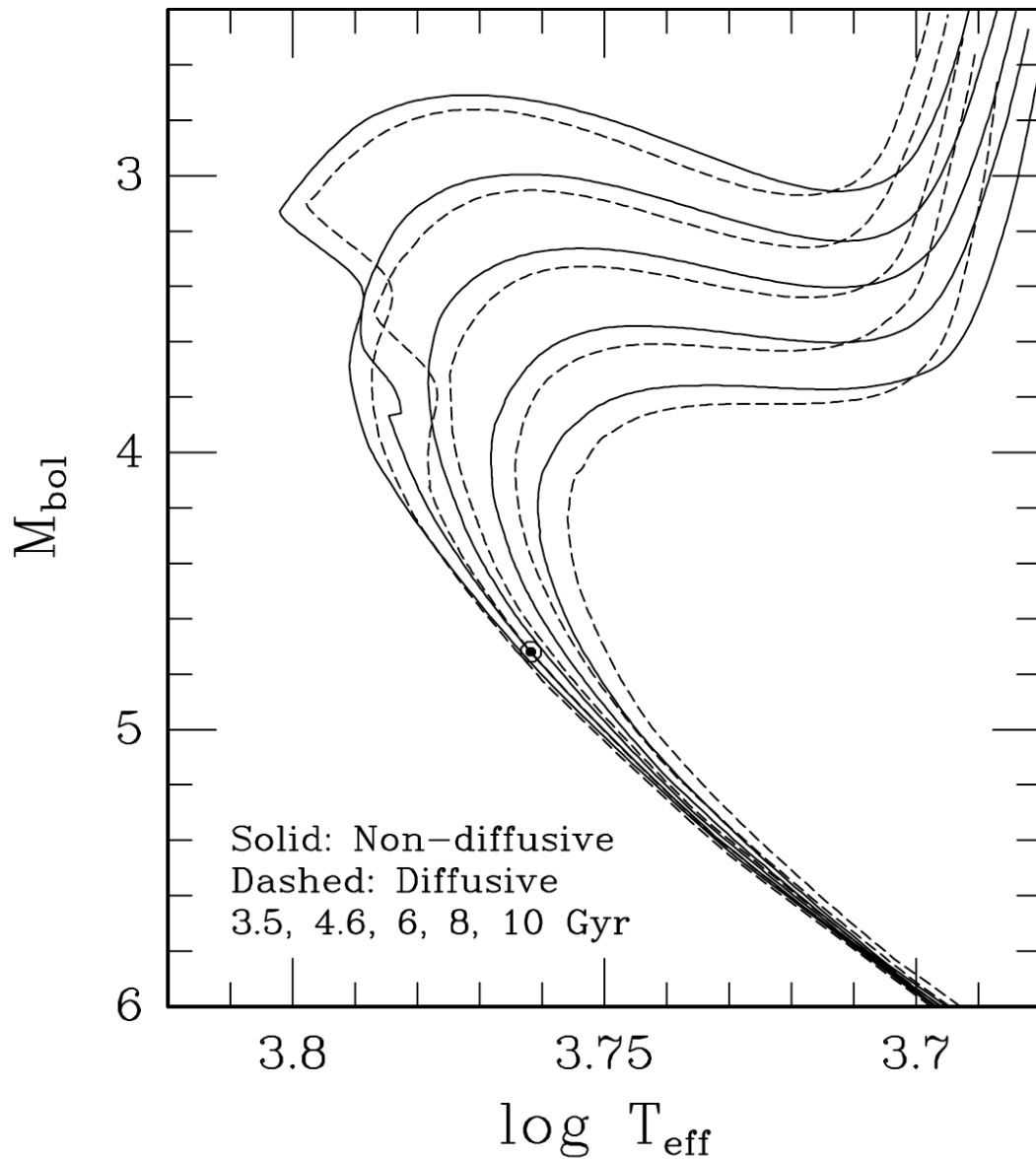
Figure 1.3: **Comparison of nondiffusive and diffusive isochrones for solar metallicity and the indicated ages.** The location of the Sun is given by the circled dot. Both sets of models are normalized to match the solar constraints. **Figure Credit:** Michaud et al. (2004)
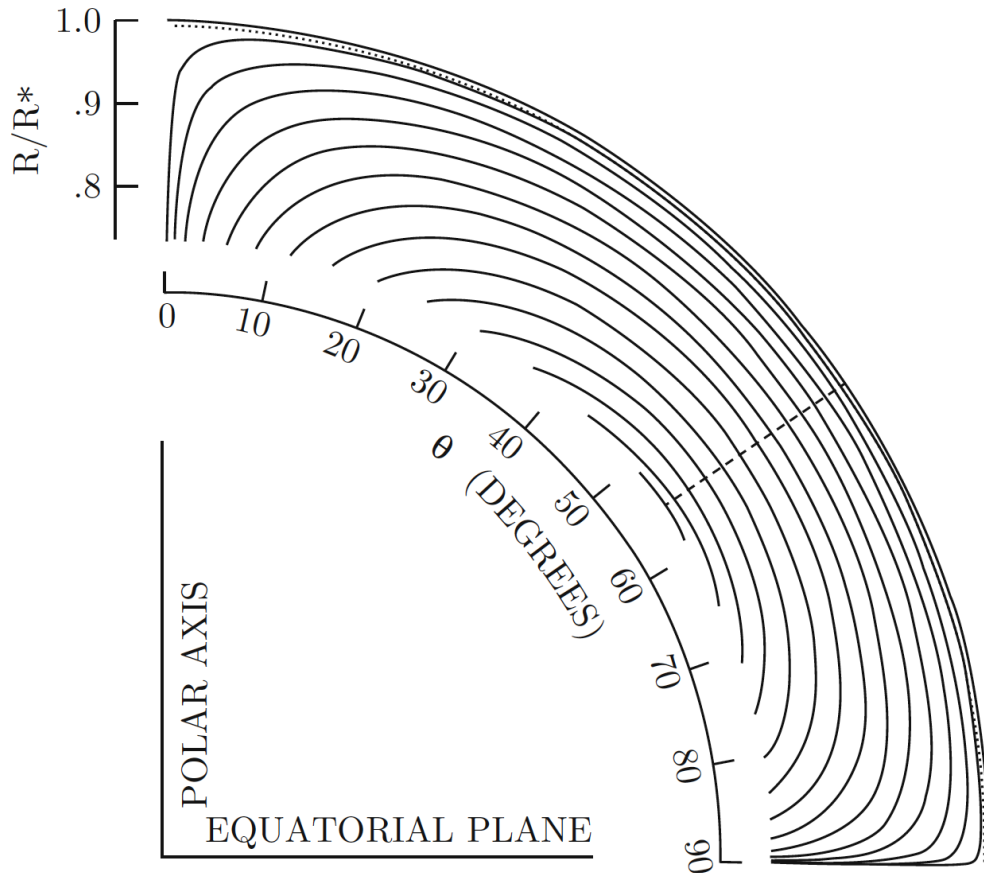
Figure 1.4: **Streamlines of the meridional circulation velocity field flow from the pole region toward the equator region.** The dotted line represents the position of the bottom of surface convection zone for the 1.8 $M_\odot$ star and the dashed line indicates the angle where the vertical component of the velocity changes sign, the circulation velocity is upward near the pole. Note that the circulation currents do not penetrate into the surface convection zone, but run along its base from the pole toward the equator. **Figure Credit:** Tassoul & Tassoul (1982)

body rotator. The surfaces of constant gravitational potential are not spherical, but the star is distorted by the centrifugal force that stretches the radial distance to a given surface more at the equator than at the pole. At a given equipotential surface, one would expect the polar region to be hotter than the equatorial plane, since the energy propagates a shorter distance along the rotation/polar axis. The temperature imbalance on the equipotential surface is very unstable and will lead to a global circulation, i.e., the matter tends to rise and cool by expansion in the pole region, while the matter tends to sink and warm up by contraction in the equator region. (Charbonneau et al. 1989)

Fig. 1.4 illustrates the streamlines of the meridional circulation velocity field, i.e., flowing from the pole toward the equator. The dotted line represents the position of the bottom of surface convection zone for the $1.8 \, M_\odot$ star and the dashed line indicates the angle where the vertical component of the velocity changes sign (the circulation velocity is upward near the pole). Note that the circulation currents do not penetrate into the surface convection zone, but run along its base from the pole toward the equator. Charbonneau & Michaud (1988) carried out a simulation of how lithium (Li) can be influenced by meridional circulation on the main-sequence of stars. It is shown that meridional circulation can carry the lithium down to depths at which lithium can be burned ($T \approx 2.6 \times 10^6 \, K$) in the equatorial region, while Li-depleted material would be brought up toward the surface in the polar region through advection by meridional circulation. Stars in the mass range $1.2 \, M_\odot \leq M_\star \leq 2.0 \, M_\odot$ and having equatorial rotational velocities larger than $30 - 35 \, \mathrm{km \, s^{-1}}$ should destroy most of their lithium on the zero-age main-sequence (ZAMS). However, in their calculation the effects of atomic diffusion was not been taken into account.

To have a detailed understanding of the interaction between atomic diffusion and meridional circulation is essential to help us understand stellar abundances. Charbonneau & Michaud (1991) tried to explain the so-called "lithium dip" (the general picture can be seen in Fig. 1.5, more details will be discussed in Chapter 3) in F-type stars of open clusters by applying the meridional circulation fields on atomic diffusion. The competition between the velocities of diffusion and meridional circulation below the surface convection zone determines how the abundance evolve. They carried out a 2D numerical simulation to calculate lithium abundances at the age of the Hyades and compared with the observation values. One can separate lithium pattern observed in the Hyades into three regions: above $T_{\mathrm{eff}} = 6900 \, K$, lithium is maintained in the convection zone and shielded from burning by the large radiative acceleration; below $T_{\mathrm{eff}} = 6900 \, K$, meridional circulation becomes important and stars to increase the effect of lithium burning, leading to the lithium

gap; as T_{eff} further decreases, rotation velocities decrease and the mass in the convection zones increases result in the surface lithium abundance less affected by meridional circulation. The agreement is satisfactory for the lithium pattern of the Hyades. However, this model fails to provide an explanation of the further drop of lithium abundance below $T_{\text{eff}} = 6000\,K$, since the rotation is too slow there.

Turbulence could be caused by shear flow instabilities sustained by differential rotation in radiative zones (Zahn 1992). Generally, as stars evolve, differential rotation with depth can be generated, both by structural evolution and angular momentum loss (mass loss, spin-down by magnetic torque). Turbulence occurs when the angular velocity gradient on equipotential surfaces becomes large enough to overcome the stabilizing effects of density stratification.

The flows of turbulence are made by a wide spectrum of macroscopic advective motions and could be extremely irregular. However, their net effect on particle transport could be simply modeled as a diffusion process (Schatzman 1969), then the diffusive velocity of a trace element Eq. 1.16 can be changed as:

$$v_D = (D_{ip} + D_T)[-\frac{\partial \ln c_i}{\partial r}] + D_{ip}[\frac{A_i m_p}{kT}(g_{\text{rad,i}} - g) + \frac{(Z_i + 1)m_p g}{2kT} + k_T \frac{\partial \ln T}{\partial r}] \quad (1.19)$$

where in the simplest case turbulent diffusion can be expressed as $D_T = \nu Re$, Re is the Reynolds number and ν is the molecular viscosity. The first bracket on the right represents the purely diffusive motion from the equilibrium abundance gradient. The coefficient of the term includes a contribution from both atomic diffusion and turbulent diffusion. Turbulent diffusion is usually assumed to be the same below the convection zone for all the species (Proffitt & Michaud 1991).

In a stratified atmosphere, turbulence is expected to be anisotropic, namely, there are many more horizontal modes of turbulence than vertical modes, since vertical modes need to work against gravity whereas horizontal modes do not. Strong horizontal turbulence can transform the meridional advection into a relatively inefficient diffusive transport in the vertical direction (Charbonneau & Michaud 1991; Chaboyer & Zahn 1992). Then a more general transport equation can be obtained by replacing the turbulent diffusion coefficient D_T of Eq. 1.19 as $D_T = D_{\text{eff}} + D_v$, where D_{eff} stands for a combination of the meridional advection and the horizontal turbulence parameterized as an effective diffusion transport coefficient and D_v denotes the transport coefficient caused by the vertical part of shear turbulence. The new transport equation can show the direct interaction between atomic diffusion and meridional circulation modified by the presence of shear turbulence. As a consequence, a transport of angular momentum and chemical composition can be further calculated in stars.
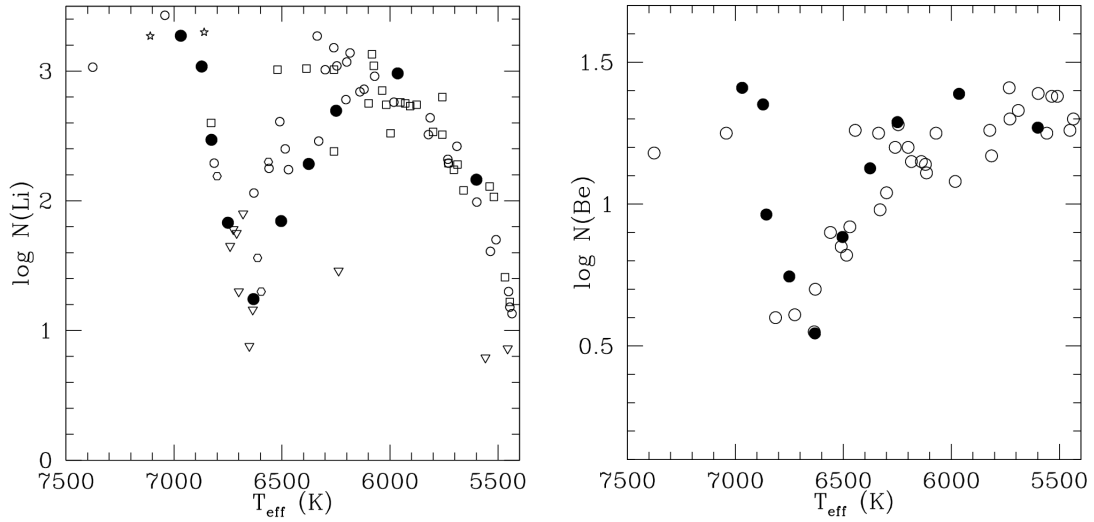
Figure 1.5: **Comparison between the computations of lithium (left) and beryllium (right) depletion and the observational values of the open cluster Hyades.** The filled circles on each panel represent the model computations at the age of Hyades for 10 stellar masses (From left to right in turn are 1.55, 1.5, 1.45, 1.35, 1.3, 1.25, 1.2, 1.1, 1.0 $M_{\odot}$). The inverted triangles on the left panel represent the upper limits. The other open symbols denote the observation values from different studies. Open circles on the right panel represent observations from Boesgaard & King (2002). **Figure Credit:** Théado & Vauclair (2003)

Théado & Vauclair (2003) showed the importance of the feedback effect of diffusion-induced μ-gradients on the meridional circulation in low-mass stars. As a result of the gravitational settling mainly of helium, a gradient of μ can be established in the outer radiative zone, which will lead to μ-currents to overcome rotational mixing (Ω-currents). The effect of differential rotation was also been taken into account in the general context. Then they carried out a 2D numerical simulation of the considered processes for a set of stars with mass ranging from 1.0 to 1.55 $M_\odot$ and the metallicity of the Hyades ([Fe/H] = 0.12). The comparison between the simulated lithium and beryllium depletion and the observational values can be seen in Fig. 1.5.

For hotter stars ($T_{\text{eff}} > 6500 , M \geq 1.3 M_\odot$), two disconnected meridional circulation loops were formed: one goes from the pole to the equator in the deeper radiative zone; while the other one goes in the opposite direction (from the equator to the pole). The element transport/mixing was suppressed by the rapidly increased μ-currents (due to the diffusion-induced μ gradient) in the region between the two circulation loops. In the relatively low-mass stars on the hot side of the lithium dip (1.3 and 1.35 $M_\odot$ in their simulation), the frozen region is still not thick enough to prevent the combined effects of the microscopic diffusion and the rotational mixing (μ-currents cannot become the same order of magnitude of Ω-currents), which leads to the depletion of lithium. This frozen region becomes larger inside the star for the higher stellar mass (1.45 and 1.5 $M_\odot$). The reason is that the higher effective temperature and thiner convective zone makes the timescale of diffusion decreases. The more efficient the diffusion, the more rapidly the μ-currents increase. Therefore, the lithium depletion is less important in the more massive stars in the cluster.

For the stars on the cool side of the lithium dip ($T_{\text{eff}} < 6500 , M \leq 1.3 M_\odot$), there is only one cell of circulation. The frozen region cannot be established at the age of the Hyades due to the inefficient diffusion. The lithium depletion starts to become smaller with the decreasing effective temperature, due to the weak rotation-induced mixing caused by the decrease of rotational velocity. For Stars cooler than $6000 \, \text{K}$, the depth of the convection zone becomes large enough to play an important role in the lithium destruction. Observations of beryllium abundances in the Hyades also show a similar behavior with lithium abundances and have a good agreement with the expected values in the model (More details will be discussed in Chapter 3).

1.2.3 Internal gravity waves

Rotational mixing has been well studied and implemented in stellar evolution models as described in the last section. However, these rotating models have been

controversial by failing to reproduce some observations. For instance, the solar rotation profile inferred from helioseismology is nearly flat from the core to the surface, indicating the the rotation of the Sun can be regarded as a quasi solid body rotator (Brown et al. 1989; Couvidat et al. 2003; García et al. 2007); while models including meridional circulation and turbulence predict large angular velocity gradients (differential rotation) at the age of the Sun (Pinsonneault et al. 1989; Chaboyer et al. 1995; Garaud 2002). Another difficulty on rotating models is to well reproduce the cold side of the lithium dip in low-mass stars of the clusters. The rotational braking mechanisms will spin down the surface efficiently on the cooler stars with deeper convective zones, driving much more destruction of lithium than the observed data. These contradictions indicate that there may have another instability become important in the transport of angular momentum and chemical elements to compete with rotational mixing in low-mass stars.

Internal gravity waves have been regarded as a potential mechanism for the internal transport of angular momentum and chemical elements mixing in low-mass stars. The idea that internal gravity waves (IGWs) generated at the base of the convective envelope (by turbulence) can transport particles and momentum within radiative zones was first proposed by Press (1981). Evolutionary models that encompass gravity waves as an important source of angular momentum transport have been developed in solar-type stars to explain the rotation profile and lithium content of the Sun (Schatzman 1993; Kumar & Quataert 1997; Talon et al. 2002; Charbonnel & Talon 2005a, 2008).

Talon & Charbonnel (2003) developed a stellar models including the effects of atomic diffusion, rotation and internal gravity waves to reproduce the lithium dip in Hyades cluster. In the framework of their model, the transport of angular momentum and chemical elements are dominated by different physical processes that are associated with three effective temperature ranges ($T_{\mathrm{eff}} > 6900\,\mathrm{K}$, $6600\,\mathrm{K} < \mathrm{T_{eff}} < 6900\,\mathrm{K}$, $T_{\mathrm{eff}} < 6600\,\mathrm{K}$).

Generally, IGWs can extract angular momentum from the stellar interior as the surface convection zone rotates slower than the interior. The generation of IGWs and its efficiency in extracting angular momentum from stellar interiors depend on the depth of convective envelope, which changes strongly with the effective temperature (Talon & Charbonnel 2005). Fig. 1.6 shows the T_{eff}-dependence of angular momentum transport driven by IGWs in main-sequence stars around the Li dip. It appears that on the hot side of the dip (more massive stars with $T_{\mathrm{eff}} \geq 6700\,\mathrm{K}$), IGWs are not activated and can be ignored for momentum transport, while the wave-driven momentum transport starts from the cool side of the dip and becomes fully efficient with decreasing T_{eff} shown as a plateau. The momentum

transport driven by IGWs reduces rotational mixing in low-mass stars, resulting in the rise of the surface lithium abundances. The simulated lithium abundance from their models with IGWs show a good agreement with observations, both regarding the behavior of lithium dip and the lithium content of the Sun (Charbonnel & Talon 2005a)

The high and constant efficiency on angular momentum transport by IGWs shown in Fig. 1.6 (the plateau with $T_{\text{eff}} < 6300\,\text{K}$) could be responsible for the so-called "Spite plateau" in metal-poor halo stars, of which lithium abundance is remarkably constant with a small dispersion and three times lower than the primordial Li abundance from CMB observations (Talon & Charbonnel 2004). In this regime, stars can become a quasi solid body rotator on a short timescale due to the efficient transport of angular momentum dominated by IGWs. As a consequece, the surface lithium depletion is independent of the initial angular momentum distribution, leading to a low dispersion of the lithium abundances from star to star (at a given T_{eff}). Conversely, more lithium depletion with larger dispersion can be expected in more massive stars ($T_{\text{eff}} > 6300\,\text{K}$) as the efficiency of IGWs decreases and differential rotation can be maintained by the effect of meridional circulation and turbulence with different initial angular momentum.

Except for the mixing processes we have mentioned, there is also an extensive catalogue of other instabilities that can also cause transport of angular momentum and chemical elements, such as, magnetic fiels, mass loss and accretion. More details of theoretical models of chemical elements mixing can be found in reviews (e.g. Michaud & Charbonneau 1991; Pinsonneault 1995, 1997; Michaud et al. 2015).

1.3 The GALactic Archaeology with HERMES (GALAH) survey

The Galactic Archaeology with HERMES (GALAH) survey is a large high-resolution spectroscopic survey targeting about one million stars, taken with the High Efficiency and Resolution Multi-Element Spectrograph (HERMES) instrument on the Anglo-Australian Telescope. HERMES collects light from a circular 2-degree Field (2dF) through the automated positioner system into 400 fibres, of which 8 fibres belong to fiducial fibres applied to align and guide the observing field on the provided targets, and the remaining 392 fibres are used for science observations. (Lewis et al. 2002). HERMES spectrograph provides two resolution modes (a nominal resolution mode with a resolving power of R≈28,000; a higher resolution
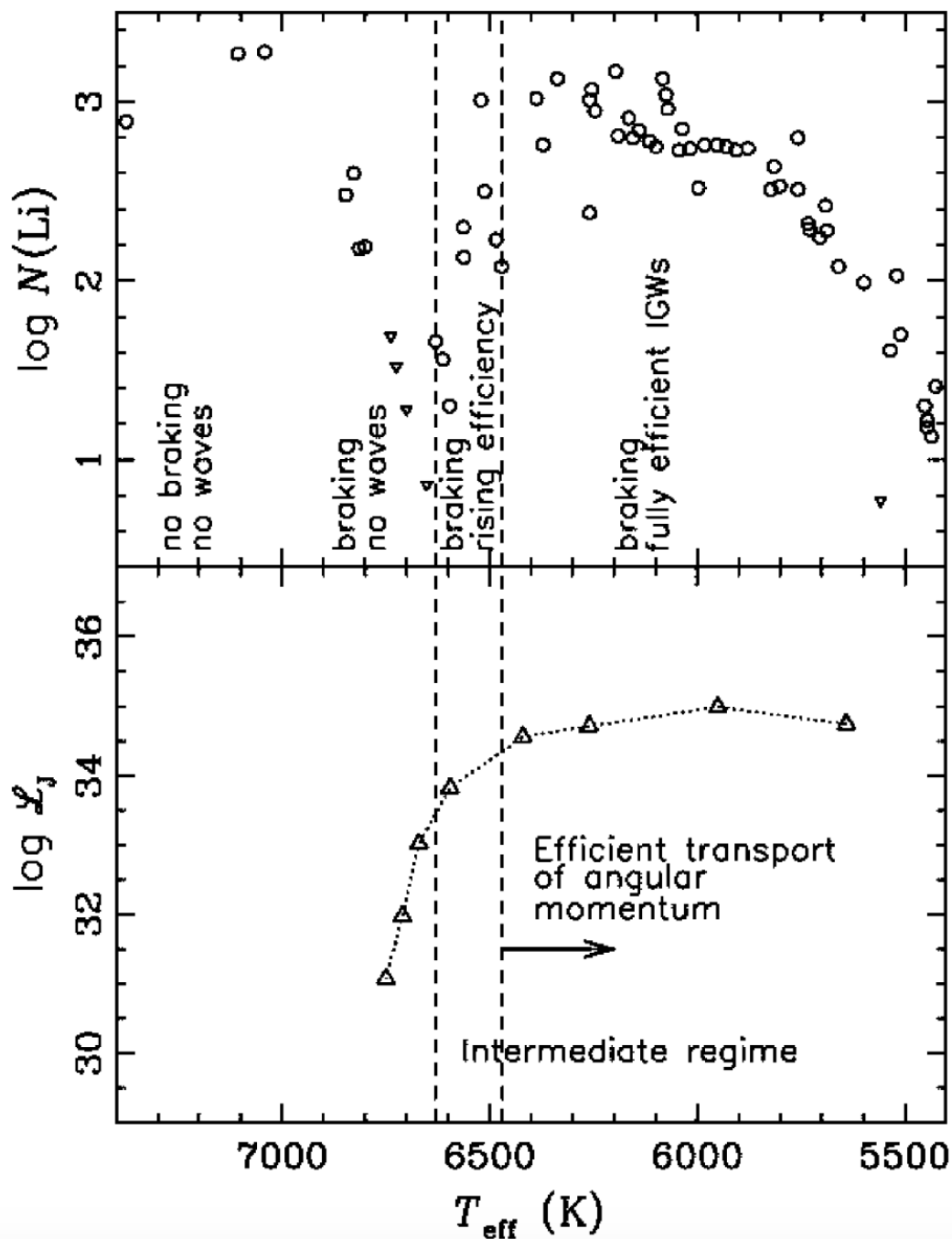
Figure 1.6: **Top panel: Lithium surface abundances versus effective temperature in the Hyades cluster.** Approximate T_{eff} dependence of surface rotational braking, in which rotational mixing become significant for the formation of the lithium dip, has been shown. Bottom panel: T_{eff} dependence of angular momentum transport induced by IGWs. **Figure Credit:** Talon & Charbonnel (2003)

mode with a resolving power of R≈42,000) in four non-contiguous optical wavelength bands between 4713 and 7887 including the blue, green, red and infrared channels (Kos et al. 2017). The wavelength ranges are chosen to cover enough measurable lines and maximize the information for determining at least 25 elements including light proton-capture elements, α-elements, odd-Z elements, iron-peak elements and n-capture elements from the light and heavy s-process and the r-process (Li, C, O, Na, Al, K, Mg, Si, Ca, Ti, Sc, V, Cr, Mn, Fe, Co, Ni, Cu, Zn, Y, Zr, Ba, La, Nd, Eu).

The selection criteria for general targets are based on a simple magnitude-limit function corresponding to $12 \leq V \leq 14$, where V magnitude are calculated from the Two Micron All Sky Survey (2MASS) JHK photometry (Skrutskie et al. 2006). The survey plans to observe about one million stars in the nominal resolution mode, covering about half of the accessible sky with galactic latitude $|b|$ larger than $10°$ and declination between $-80° < \delta < +10°$. Given this observational selection, 75 percent of targets are expected to belong to the Galactic thin disc, and 24 percent belong to the thick disc, with the rest of sample consist of nearby halo stars and bright red giants (Martell et al. 2017).

GALAH survey is mainly designed and served for Galactic Archaeology, which aims to unravel the formation and evolutionary history of the Milky Way. To built up the current Galactic structures, i.e., the disk, the bulge and halo of the Milk Way we see at redshift equals to zero, the history events of star-forming aggregates and galaxies accretion/mergers need to be well recognized. Unfortunately, after dispersing from the initial star-forming clusters or host galaxies, most of the dynamical information of these stars has been lost through heating and migration processes. Nevertheless, another potential approach to reveal our Galaxy history is through common chemical composition of stars. Chemical tagging was proposed to recognize those dispersed remnant stars and associate them to common star-forming aggregates or accreted galaxies through their identical and unique chemical abundance patterns (Freeman & Bland-Hawthorn 2002; Venn & Hill 2008; De Silva et al. 2009; Bland-Hawthorn et al. 2010). With the support of GALAH survey, a large data set with precise enough stellar parameters and detailed elemental abundances could be determined, which will allow chemical tagging techniques to be carried out confidently.

In addition to the primary scientific goal for Galactic archaeology, other research areas, such as, stellar physics, star clusters, interstellar medium and stellar populations in the Magellanic Clouds could be benefit greatly from the GALAH data. A thorough discussion about the GALAH survey science goals can be checked in De Silva et al. (2015). Moreover, due to the wide sky coverage of the GALAH survey, it

provide important synergies with other large-scale surveys. Especially for the synergy with the Gaia mission (Gaia Collaboration et al. 2016), the overlap data set between GALAH and Gaia will have high-precision astrometric measurements (parallaxes and proper motions) from the Gaia and high accurate elemental abundances from the GALAH spectroscopy, assembling an extremely powerful resource for the study of star formation and chemical evolution in the Galaxy (Martell et al. 2017). All the data in this thesis are contributed by the GALAH survey.

Chapter 2

Verifying abundance trends in the open cluster M67 using non-LTE modelling

The following chapter contains a slightly modified version of an article that was published in Monthly Notices of the Royal Astronomical Society in December 2018 (Gao et al. 2018)

2.1   Introduction

In Chapter 1, we have briefly introduced a technique known as chemical tagging (Freeman & Bland-Hawthorn 2002), which is used for Galactic Archaeology. The stellar abundance pattern over many elements is analogous a stellar DNA profile, leading to reflect the chemical state of their progenitor clouds (De Silva et al. 2009). With the chemical tagging approach, it would be useful for distinguishing the history events of large star-forming aggregates and accreted galaxies and reconstructing the disk, bulge and halo of the Galaxy from the dispersed stars. For example, Kos et al. (2018) have successfully identified two new members of the Pleiades, located far from the cluster centre, with chemical tagging, and recovered seven observed clusters in chemical space by using t-distributed stochastic neighbour embedding (t-SNE).

To fulfill this chemical tagging in Galactic Archaeology, we need to collect enough stars from each initial star-forming group and derive precise enough stellar parameters and elemental abundances. Fortunately, a large amount of high quality

27

observed data will be provided by massive high resolution spectroscopic surveys such as the GALAH (De Silva et al. 2015), Gaia-ESO (Gilmore et al. 2012) and APOGEE (Majewski et al. 2017), WEAVE (Dalton et al. 2012), 4MOST (de Jong et al. 2012). Another condition is that dispersed stars should be formed in chemically homogenous aggregates, which could encourage for recognizing and recovering the dispersed star-forming events by their identical chemical signatures with small spread. Open clusters become good targets to test this idea, since they are assumed to be formed in a single burst of star formation from a chemically homogeneous and well-mixed molecular cloud (e.g. De Silva et al. 2006, 2007; Pancino et al. 2010; Magrini et al. 2014; Feng & Krumholz 2014). Their member stars should be coeval, and share the same initial bulk chemical compositions, differing only in their initial stellar masses.

However, on the observational side, chemical abundance variations along the evolutionary phases in open clusters have been found, namely, in the same open cluster, the surface abundances measured in (unevolved) dwarf stars are apparently offset compared to those measured in (evolved) giant stars (e.g. Villanova et al. 2009; Schuler et al. 2009; Önehag et al. 2014; Martin et al. 2017). Moreover, these abundance trends with evolutionary stage cannot be simply explained by the standard stellar evolution model, in which convection is the only internal mixing process.

Atomic diffusion is one possible explanation for these surface abundance trends (Michaud et al. 1984), which can perturb the surface abundances of dwarfs with shallow convection zones: different chemical species will be underabundant or overabundant to varying degrees in the stellar atmosphere, depending on the competing effects of gravitational settling and radiative acceleration. In low-mass stars, the general trend is quite similar for most element species, i.e., surface abundances start to decrease during the main-sequence and reach a minimum at the turn-off. The amplitude of the abundance variation between the main sequence and the turn-off depends on the efficiency of radiative acceleration for different species. Furthermore, once the star leaves the turn-off point and starts climbing the red giant branch, the deeper convection zone will bring the material from the interior and restore the original composition in the atmosphere.

Systematic abundance trends with evolutionary stage have also been measured in a number of globular clusters, which can be well described by using atomic diffusion models with extra turbulent mixing below the convection zone (e.g. Korn et al. 2007; Lind et al. 2009b; Nordlander et al. 2012; Gruyters et al. 2014, 2016). However, these globular clusters are old, and only probe the low metallicity regime ($-2.3 <$ [Fe/H] < -1.5). They also show anti-correlations in some light elements, which is thought to be produced by intra-cluster pollution by short-lived stars of

the first cluster generation (e.g. Prantzos & Charbonnel 2006). In contrast, open clusters probe the metallicity and age range typical of the Galactic disk, and are not expected to have experienced such internal pollution. Thus, the stellar surface compositions of open cluster members should truly reflect the primordial abundances from the proto-cluster, unless they have been altered by evolutionary effects.

Messier 67 (M67, or NGC 2682) is an ideal open cluster to study such evolutionary effects with a well determined reddening $(E(B-V) = 0.041)$ and distance modulus ($\mu = 9.70 - 9.80$; Sarajedini et al. 2009; Yakut et al. 2009). For most open clusters, main-sequence and turn-off stars are difficult for spectroscopic studies due to their relatively faint magnitudes, while M67 can allow a detailed spectroscopic study of stars at different evolutionary stages, even for its main sequence stars. M67 has been widely studied, with the various studies obtaining slightly different results. For example, the averaged metallicities ([Fe/H]) ranges from -0.04 to $+0.05$ (Hobbs & Thorburn 1991; Tautvaišiene et al. 2000; Yong et al. 2005; Randich et al. 2006; Pasquini et al. 2008; Pace et al. 2008), while determinations of the cluster age vary between 3.5 to 4.8 Gyr (Yadav et al. 2008; Önehag et al. 2011). Considering the uncertainties in the different studies, they are all consistent with the conclusion that chemical composition and age of M67 are similar to those of the Sun. Some studies have therefore searched for solar twin candidates from this cluster (Pasquini et al. 2008; Önehag et al. 2011, 2014). It also has even been suggested that this is the original birthplace of the Sun (Önehag et al. 2011), but this has been challenged (Pichardo et al. 2012; Gustafsson et al. 2016).

Previous studies of abundance trends in M67 have been based on small samples (e.g. Tautvaišiene et al. 2000; Yong et al. 2005; Randich et al. 2006; Pace et al. 2008; Pancino et al. 2010). In particular, Önehag et al. (2014) found that heavy element abundances in dwarf stars are reduced by typically 0.05 dex or less, compared to those in subgiants. Atomic diffusion has already been suggested as the underlying cause for the abundance trends in M67 (Önehag et al. 2014; Bertelli Motta et al. 2017; Souto et al. 2018); it is worth noting that, for the mass range of M67 (less than about $2\,M_\odot$), intermediate and heavy elements will not be influenced by nuclear reactions associated with dredge-up (Smiljanic et al. 2016); the light elements Li, Be, and B can be destroyed during the course of the first dredge-up.

However, in order to use the surface abundance trends to make quantitative statements about atomic diffusion processes, the measured surface abundances must be accurate. To date, most abundance analyses have employed the simplifying assumption of local thermodynamic equilibrium (LTE) for the gas in the stellar atmosphere. In reality, conditions in the line-forming regions are such that radiative transitions typically dominate over collisional transitions; the non-thermal radiation

field thus drives the gas away from LTE. Thus, to measure surface abundances to better than 0.05 dex, departures from LTE must be taken into account (e.g. Asplund 2005, and references therein). Moreover, the errors arising from the assumption of LTE are systematic, and can therefore result in spurious abundance trends which, if taken to be real, can lead to incorrect conclusions about stellar and Galactic physics. For example, recent studies in open clusters show a remarkable enhancement of Na abundance compared with field stars, however, this Na-enhancement is only an artefact of non-LTE effects, which have been shown by MacLean et al. (2015).

In the present study we carry out a detailed non-LTE abundance analysis of lithium, oxygen, sodium, magnesium, aluminium, silicon, and iron, across 66 M67 members. We employ a homogeneous data set drawn from GALAH survey (De Silva et al. 2015), to study how departures from LTE can influence the observed abundance trends in M67. By comparing the trends against recent stellar models that include atomic diffusion, we investigate how departures from LTE influence interpretations about the efficiency of mixing processes in stellar atmospheres.

2.2 Observational data and sample selection

The spectroscopic observations of target stars in M67 were taken from the GALAH survey. The stars in the GALAH survey were observed with the HERMES spectrograph (Sheinis et al. 2015) mounted on the Anglo-Australian Telescope (AAT). The spectra provided by HERMES are in fixed format with four noncontiguous wavelength bands, 471.3-490.3 nm (Blue), 563.8-587.3 nm (Green), 647.8-673.7 nm (Red), and 758.5-788.7 nm (IR). HERMES is designed to operate at two resolution modes for GALAH. During the normal operation, HERMES observes with a resolving powers of $R \sim 28,000$. A higher resolution of $R \sim 42,000$ was used during part of the GALAH pilot survey (Martell et al. 2017). This study is based only on spectra taken in the higher resolution mode (i.e. $R \sim 42,000$). The observations were carried out during the period of 7-14 February 2014. The exposure time ranges from 3600 s to 7200 s. The spectra were reduced using the dedicated GALAH reduction pipeline (Kos et al. 2017), with 2dfdr and IRAF used to perform bias subtraction, flat fielding, wavelength calibration and spectral extraction. The sky background was subtracted from each individual observation. Observed spectra of the same object with different observation dates were stacked for higher signal-to-noise (SNR). All the targets satisfy SNR > 50 in Green, Red and IR arms.

In Fig. 2.1 we show the colour-magnitude diagram (CMD) for the observed M67

sample (stars with $8.8 < V < 14$). The original candidate list was sourced from the precise optical photometry available from Stetson's database of photometric standard fields [1]. Fig. 2.1 shows the M_J, $(J - K)_0$ CMD for the stars using the Two Micron All Sky Survey photometry (Skrutskie et al. 2006) with a M67 distance modulus of 9.70 and reddening $E(B - V) = 0.041$ mag. We determined the radial velocities and spectroscopic stellar parameters as described in Sect. 2.3.3. To refine the membership selection, we iteratively rejected 2σ outliers in radial velocity. We also excluded two probable members that are cooler than $4500\,\mathrm{K}$, since our approach to determining spectroscopic parameters (based on unblended H and Fe lines) is not reliable at these cool temperatures. Finally, we retained all the stars within 3σ in [Fe/H] as our final sample, thereby rejecting another 8 probable foreground objects of similar radial velocity as the cluster. The abandoned and retained stars are shown in different symbols in Fig. 2.1.

In Fig. 2.3 we show histograms of the radial velocity and metallicity distributions of the final sample of stars, together with a Gaussian fit with $< \mathrm{RV} >= 34.31\,\mathrm{km\ s^{-1}}$ and $\sigma = 0.78\,\mathrm{km\ s^{-1}}$, which is consistent with the result from Geller et al. (2015) ($\mathrm{RV} = 33.64 \pm 0.96\,\mathrm{km\ s^{-1}}$). We also made a cross-match of our targeted stars in SIMBAD (Wenger et al. 2000) by using the coordinates to identify the corresponding objects within a radius of 2 arcsec. We found four stars in our final sample (marked as grey hexagon in Fig. 2.1) that are listed as spectroscopic binaries in SIMBAD; we excluded these binaries in the sample. Furthermore, by checking the positions of all the left stars in the isochrones (see Fig. 2.2), we excluded two stars that could be blue stragglers whose temperature are significantly hotter than the other turn-off stars. The coolest dwarf that might well be an unresolved binary has been removed, which lies well above the isochrones in $\log g$. We also see that six stars stand out in Fig. 2.1 as likely red clump stars. The final stellar sample contains 66 stars with high resolution spectra, including turn-off, subgiant, red-giant, and red-clump stars, as well as a single solar-like main-sequence star.

2.3 Abundance analysis

The spectra were analysed using a modified version of the GALAH analysis pipeline, which is developed for a full scientific analysis of the GALAH survey and has been applied to determine stellar parameters and abundances in a number of recent studies (e.g. Sharma et al. 2017; Wittenmyer et al. 2017; Duong et al. 2018). The

---

[1]`http://www.cadc-ccda.hia-iha.nrc-cnrc.gc.ca/en/community/STETSON/standards/`
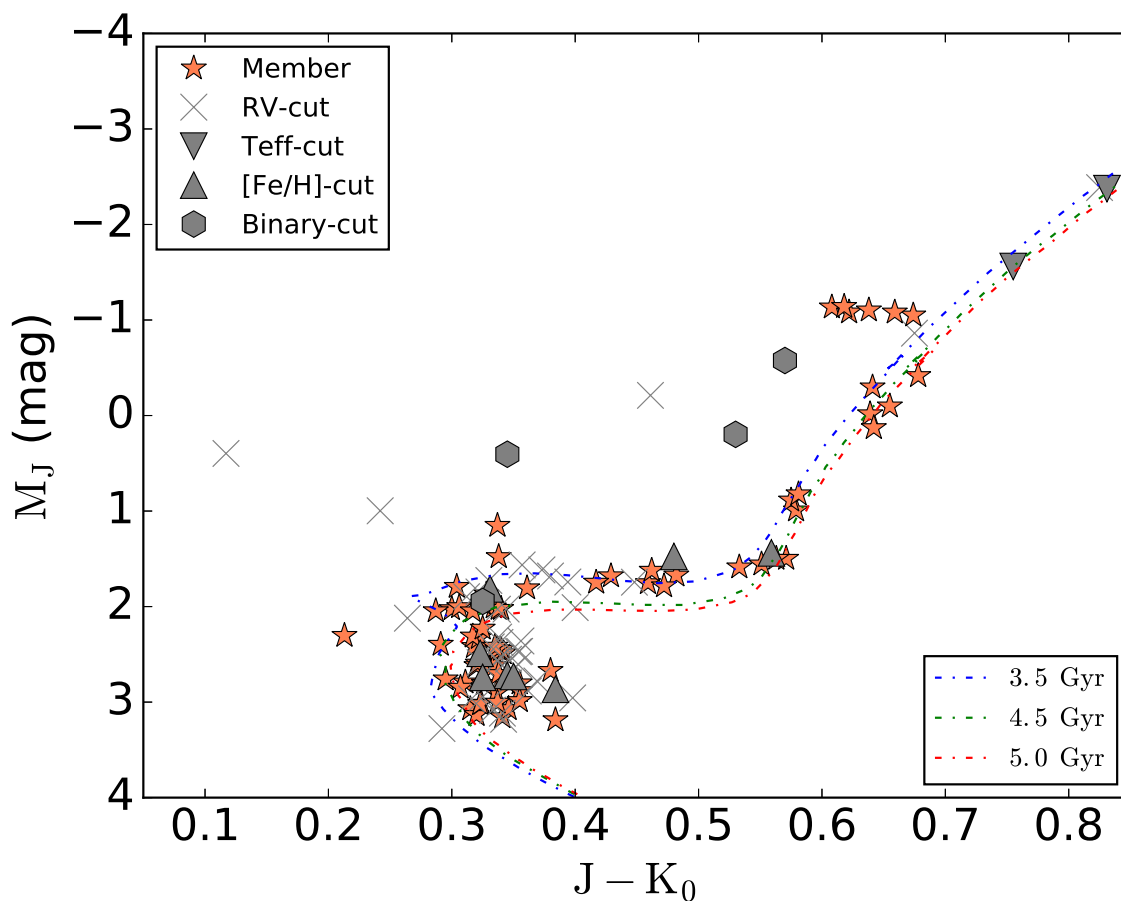
Figure 2.1: **Colour-Magnitude Diagram of the open cluster M67 generated by using the photometric data from 2MASS (Skrutskie et al. 2006) with a distance modulus of 9.70 and reddening** $E(B - V) = 0.041$ **mag.** The excluded stars are represented by different grey symbols for different selection processes. The cluster members selected and used in this study are marked as filled red star symbols. The spectroscopic binaries found in our final sample are shown as grey hexagon. Solar abundance isochrones corresponding to an age of $3.5\,\mathrm{Gyr}$, $4.5\,\mathrm{Gyr}$ and $5.0\,\mathrm{Gyr}$ are shown as dot-dashed lines in different colours.
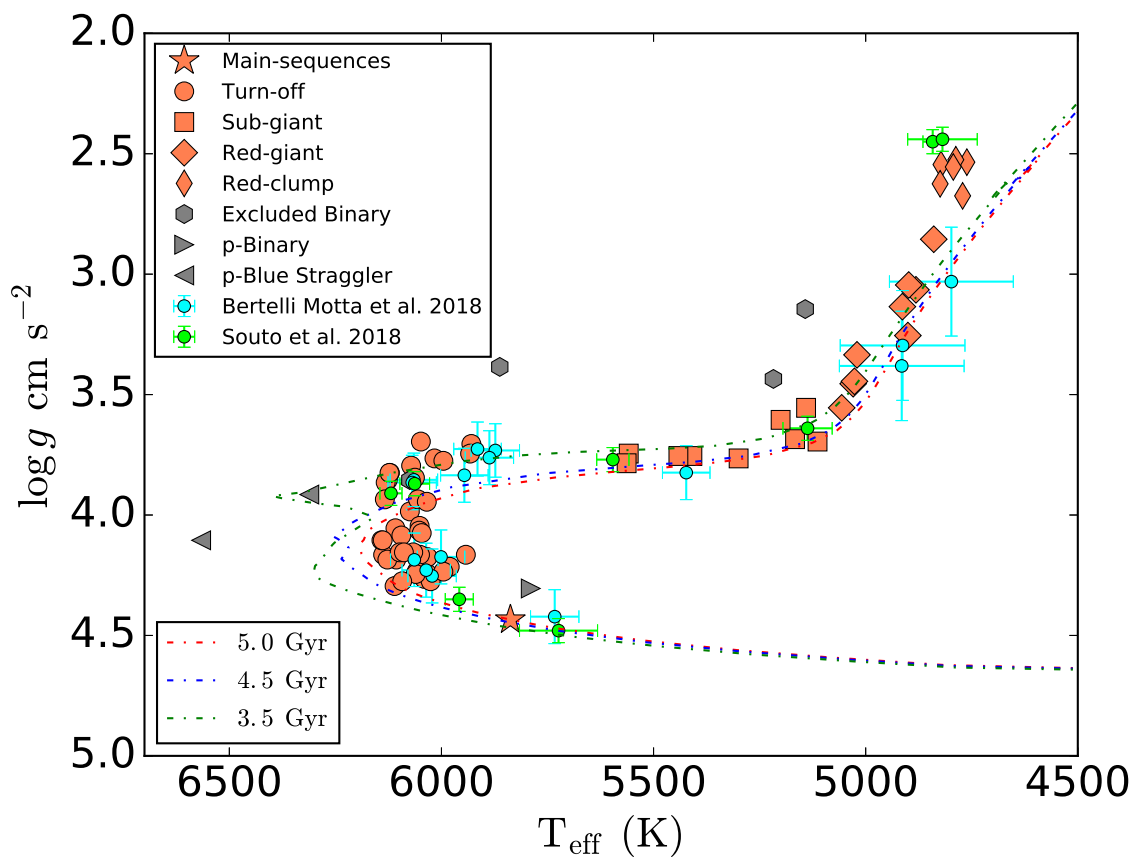
Figure 2.2: **Theoretical isochrones of M67 with solar metallicity and different ages.** The sample stars are divided into main-sequence, turn-offs, subgiants and giants represented by different symbols. The excluded binaries, possible blue stragglers and unresolved binary are also displayed. The effective temperature and gravity of the targeted stars has been offset by 59 K and 0.22 dex, respectively. Results from Bertelli Motta et al. (2018) and Souto et al. (2018) are also shown for comparsion.

pipeline and the results for the full survey sample are further described and evaluated in GALAH's second data release paper (Buder et al. 2018). The input data for this pipeline includes: the reduced observed spectra and corresponding measurement errors (Sect. 2.2); initial guesses for the stellar atmosphere parameters and radial velocity; reference solar abundances; and a list of atomic and molecular lines. The spectra, which have been radial velocity corrected as described in Kos et al. (2017), were first continuum-normalised using straight lines over 3-60 wide segments in all four arms. Wavelength regions contaminated by telluric or sky lines were removed (Buder et al. 2018). The radiative transfer and abundance analysis was carried out using the automated spectrum analysis code SPECTROSCOPY MADE EASY (SME; Piskunov & Valenti 2017). We detail aspects of this pipeline in the remainder of this section.

2.3.1   Atmosphere grids

The spectral line synthesis with SME is based on MARCS model atmospheres (Gustafsson et al. 2008) with atmospheric parameters spanning effective temperatures $2500 \leq T_{\mathrm{eff}}/\mathrm{K} \leq 8000$, surface gravities $-0.5 \leq \log_{10}(g/\mathrm{cm\,s^{-2}}) \leq 5.0$, and metallicities $-5.0 \leq [\mathrm{Fe/H}] \leq 1.0$. Spherical models were used for $\log g \leq 3.5$ and plane-parallel models were otherwise used. The standard chemical composition grid was adopted, which uses the solar chemical composition of Grevesse et al. (2007), scaled by [Fe/H], and with an enhancement to -elements of $0.1\,\mathrm{dex}$ for $[\mathrm{Fe/H}] = -0.25$, $0.2\,\mathrm{dex}$ for $[\mathrm{Fe/H}] = -0.5$, $0.3\,\mathrm{dex}$ for $[\mathrm{Fe/H}] = -0.75$, and $0.4\,\mathrm{dex}$ for $[\mathrm{Fe/H}] \leq -1.0$.

2.3.2   Non-LTE grids

For non-LTE calculations in SME, instead of solving the non-LTE radiative transfer equations directly, grids of pre-computed departure coefficients $\beta = n_{\mathrm{NLTE}}/n_{\mathrm{LTE}}$ as functions of optical depth were employed instead, as described in Piskunov & Valenti (2017). When performing the spectral fitting for stellar parameter determinations, as well as the spectral fitting for chemical abundance determinations, the grids of pre-computed departure coefficients (for each stellar model and target abundance) were read in and interpolated based on a given stellar model and non-LTE abundance. Then the corresponding departure coefficients were applied to the corresponding LTE level populations to synthesise the lines.

The non-LTE departure coefficient grids for all the elements were taken from

recent non-LTE radiative transfer calculations based on 1D hydrostatic model MARCS atmospheres (i.e. consistent with the rest of the analysis). The calculations themselves, and/or the model atoms, were presented in the following studies:

- lithium: Lind et al. (2009a)

- oxygen: Amarsi et al. (2015) (model atom)

- sodium: Lind et al. (2011)

- magnesium: Osorio & Barklem (2016)

- aluminium: Nordlander & Lind (2017)

- silicon: Amarsi & Asplund (2017) (model atom)

- iron: Amarsi et al. (2016b)

A brief overview of the model atoms are presented here: Energy levels and radiative data were taken from various databases, as appropriate or applicable: NIST (Reader et al. 2012), TOPbase (Peach et al. 1988), TIPbase (Bautista 1997), and the Kurucz online datebase (Kurucz 1995). Inelastic collisional processes, between the species in question and either free electrons or neutral hydrogen atoms, can be a major source of uncertainty in non-LTE analyses (e.g. Barklem 2016a). The oxygen, sodium and magnesium aluminium grids benefit from X+e inelastic collision data based on the R-matrix method (e.g. Burke et al. 1971; Berrington et al. 1974), while the collision data for aluminium is calculated by using the Breit-Pauli distorted wave (Badnell 2011). Both methods are more reliable than commonly used alternatives, such as the van Regemorter recipe (van Regemorter 1962).

Furthermore, more realistic cross-sections for inelastic collisions with neutral hydrogen (X+H) are included in the calculations of all the element grids, which is in turn more reliable than the commonly used Drawin recipe (Steenbock & Holweger 1984; Lambert 1993). To be more specific, for Li, the rate coefficients for inelastic collisions with neutral hydrogen were accounted for (Belyaev & Barklem 2003; Barklem et al. 2003); for O, the rate coefficients were treated by the formula from Drawin (1968) with a correction followed by Lambert (1993); for Na, the rate coefficients were adopted from Barklem et al. (2010); for Mg, the rate coefficients were based on the accurate calculations from Barklem et al. (2012); for Al, the rate coefficients were taken form the computation of Belyaev (2013); for Si, the rate coefficients of low and intermediate levels were used from Belyaev et al. (2014); for Fe I, the rate coefficients were calculated with the asymptotic two-electron method,

which was applied to Ca+H in Barklem (2016b). Since the reactions between Fe II and hydrogen are not very prominent, thus for Fe II, the collision excitation with hydrogen was still implemented by the old recipe of Drawin (1968).

2.3.3   Spectroscopic stellar parameters

To avoid degeneracy issues that result from having too many free model parameters, the analysis separates the determination of the surface elemental abundances from the rest of the stellar parameters, namely the atmospheric parameters $T_{\rm eff}$, $\log g$, [Fe/H], as well as projected rotational velocities $v \sin \iota$, and line-of-sight radial velocity RV. In addition, microturbulence ξ and macroturbulence $v_{\rm mac}$ are standard parameters in 1D atmosphere analysis used to model the impact of convective motions on the spectral lines (e.g. Gray 2005, Chapter 17). In principle, ξ could be set as a free parameter when fitting the spectrum, but we find that this parameter has similar values for similar stars. Additionally, macroturbulence and projected rotation $v \sin \iota$ have a degenerate influence on spectral line broadening and cannot been disentangled, especially for the slowly rotating cool stars. Therefore, in this project we applied fixed values for ξ, which are obtained from an empirical relation as a function of $T_{\rm eff}$ (see Fig. 2.4), while we treated $v \sin \iota$ as a free parameter with a rotational broadening profile (e.g. Gray 2005, Chapter 18) and set $v_{\rm mac}$ as zero. During this procedure, the synthetic spectra were also convolved with a Gaussian instrumental profile of varying resolution over each arm, which is the dominant source of broadening.

The stellar parameters were determined simultaneously, by fitting (via χ^2 minimisation) the observed profiles of Sc I, Sc II, Ti I, Ti II, Fe I, and Fe II lines that were unblended and that had reliable atomic data, as well as two of the Balmer lines: H and H. The benefit of this approach is that, for example, both the temperature sensitive Balmer line wings and the excitation-balance of neutral iron-peak species strongly influence the effective temperature determination; similar statements can be made for the inferred surface gravity and metallicity (Sect. 2.3.2). In this process, iron was treated in non-LTE (Amarsi et al. 2016b), unless otherwise stated. The non-LTE effects on iron lines are small, for late-type stars of solar-metallicity (e.g. Lind et al. 2012) and we find this choice has only a small influence on the values of the other stellar parameters (the mean differences in $T_{\rm eff}$ and $\log g$ under the assumption of LTE and non-LTE are 3.5 K and 0.01 dex, respectively).

As described in GALAH's second data release paper (Buder et al. 2018), a bias in surface gravity of 0.15 dex and a bias in metallicity of 0.1dex is found for purely spectroscopic SME results when compared to results including interferometric,
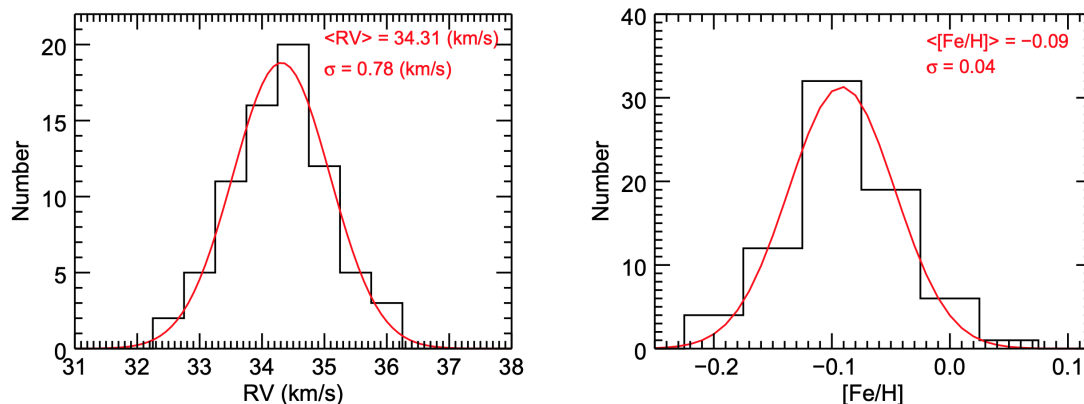
Figure 2.3: **Histogram of the radial velocity and metallicity distributions of the final members selected in M67.** The corresponding Gaussian fit to the distributions are also been shown in red lines.
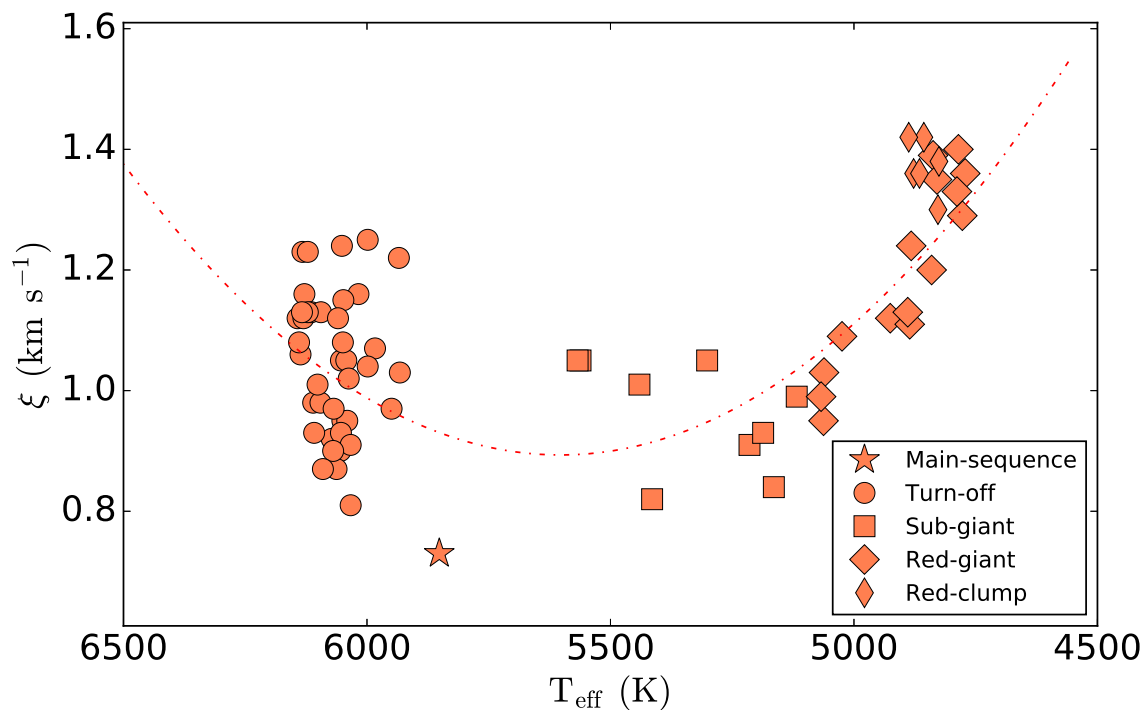
Figure 2.4: **Microturbulence ξ as a function of effective temperature, when treated as a free parameter in stellar parameters calculation.** This distribution was fitted by an empirical quadratic polynomial, in order to determine the relation between these two parameters that was subsequently enforced.

astrometric, and/or asteroseismic constrains. These offsets were applied to all survey targets in Buder et al., in a similar fashion to other large spectroscopic surveys, such as in APOGEE (Holtzman et al. 2015, Sect. 5) and RAVE (Kunder et al. 2017, Sect. 6).

In this study, we chose to use only the Sun as our reference star, because our cluster stars are very close to solar metallicity. By analyzing a high resolution solar spectrum (Sect. 2.3.5), we find that our analysis pipeline requires positive offsets in T_{eff}, $\log g$ and [Fe/H] of 59 K, 0.22 dex and 0.09 dex respectively, to match the reference solar values. We apply these offsets to our spectroscopic parameters before determining chemical abundances.

Since our sample spans a large range in stellar parameters, we could have attempted to design a more sophisticated calibration method involving more reference stars. However, our simple method has the advantage of preserving the relative parameter differences found by spectroscopy and therefore do not strongly influence the derived abundance trends. Our assumption is thus that the internal precision of our spectroscopic method is reliable enough to comment on abundance trends.

As a sanity check, in Fig. 2.2 we compare our effective temperatures and surface gravities with theoretical cluster isochrones. The three stellar evolutionary tracks and isochrones have been produced using the Padova database (Bressan et al. 2012; Chen et al. 2014; Tang et al. 2014), with solar metallicity ($Z = 0.0142$), but different ages of $t = 3.5$ Gyr, $t = 4.5$ Gyr (close to that of the Sun), and $t = 5.0$ Gyr. The parameters of the stars fall into the reasonable region of the isochrone tracks, without any further calibrations.

2.3.4 Spectroscopic abundances

In principle, GALAH spectra can allow for up to 30 elements to be determined, but here we only focus on those for which we have non-LTE grids for. Having obtained the optimal stellar parameters (Sect. 2.3.3), elemental abundances for lithium, oxygen, sodium, magnesium, aluminium, and silicon were then inferred; the abundance of iron was also re-inferred, using only iron lines. The trace element assumption was employed here: i.e. that a small change to the abundances of the particular element being studied has a negligible impact on the background atmosphere and hence the optimal stellar parameters. Thus, the stellar parameters were kept fixed, and the only free parameters were the elemental abundances. The synthesis of the spectral lines incorporated non-LTE departure coefficients

(Sect. 2.3.2).

Unsaturated, unblended lines are preferred as abundance indicators. For partially blended lines in the list, synthetic spectra are fitted in an appropriate selected spectral region that neglects the blended part of the line. Likewise, the abundances were calculated from those lines using χ^2 minimised synthetic fits. All of the lines used in the abundance analysis and their detailed information are presented in Buder et al. (2018). Fig. 2.5 shows the comparison between observed and best-fit synthetic line profiles of Na, Mg and Si in both LTE and non-LTE for three stars coming from different groups: turn-offs, subgiants and giants. During these fittings, only abundance is set as a free parameter. Abundance difference between non-LTE and LTE synthesis can be substantial, even though all the fits look similar with each other.

2.3.5 Solar reference

In order to obtain accurate abundance ratios of these late-type stars with respect to the Sun, it is important to determine solar abundances in a consistent manner (e.g. García Pérez et al. 2006). However, we do not have access to a high-quality HERMES solar spectrum observed in the high-resolution mode. Instead, we used the very high-resolution ($R \sim 350,000$) Kitt Peak solar flux atlas of Brault & Neckel (1987). The solar analysis proceeded in the same way as for our M67 targets. The resulting spectroscopic parameters are generally in good agreement with the standard solar values; the spectroscopic T_{eff} is lower by $59\,\text{K}$, $\log g$ is lower by $0.22\,\text{dex}$, and [Fe/H] is lower by $0.09\,\text{dex}$, as we already mentioned in Sect. 2.3.3. The above offsets were applied to the subsequent solar abundance analysis, as well as to the abundance analysis of all the M67 stars.

We list the final inferred solar abundances in Table 2.1. Our solar abundances are in good agreement with those of Grevesse et al. (2007), the most discrepant elements being magnesium, which is $0.09\,\text{dex}$ higher in our non-LTE analysis. Our solar abundances are also very similar to the 1D non-LTE ones presented in Scott et al. (2015b,a); all of our values agree with theirs to within $0.04\,\text{dex}$.

2.3.6 Error estimation

To estimate the overall precision of atmospheric parameters, we reanalyse all the individual spectra of the 63 stars in our sample that have multiple observations, typically two or three. We compute the maximum difference in atmospheric
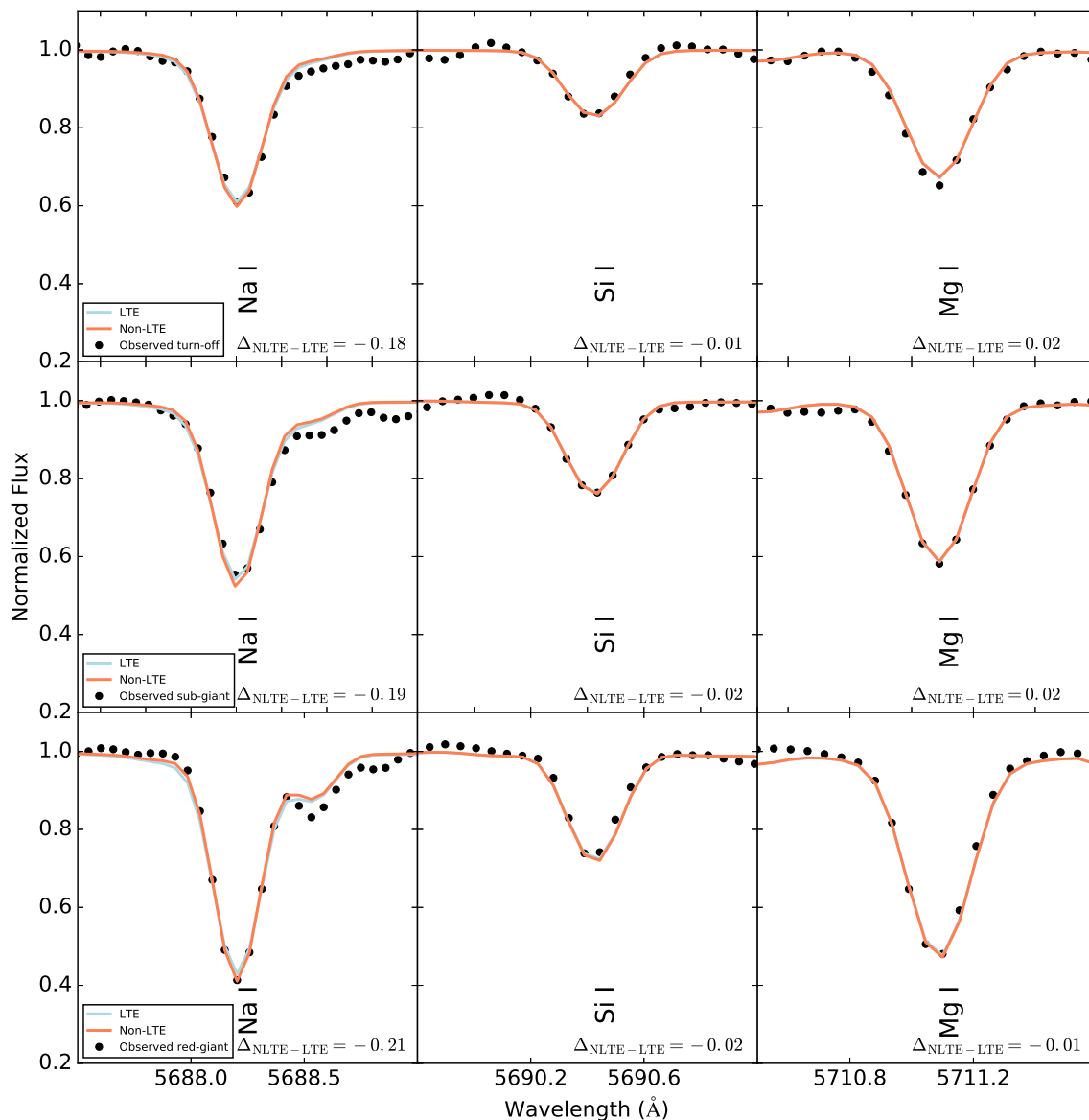
Figure 2.5: **Typical best-fit synthetic LTE and non-LTE line profiles of Na, Mg and Si compared with the observed spectra of three stars in different evolutionary stage; a turn-off, a subgiant and a giant.** Only abundance is set as a free parameters in these fittings. Abundance differences between non-LTE and LTE synthesis are showed in the labels.

parameters obtained from individual spectra and adopt the mean values as representative for the entire sample, since we find that these values are fairly independent of S/N and stellar parameters. We finally sum these errors in quadrature with the formal covariance errors returned by SME to obtain the final overall error (effective temperature 40 K, surface gravity 0.14 dex and metallicity 0.07 dex).

The influence of the uncertainties in the atmospheric parameters on our final abundance determinations was assessed by varying each time only one of atmospheric parameters by the amount of their estimated uncertainties. We finally added all the individual errors associated with the three contributors quadratically to obtain the total error in abundances. These internal errors are applied to produce the error bars in the following Fig. 2.7, Fig. 2.8, Fig. 2.9 and Fig. 2.10. Note that the abundance uncertainties may be underestimated, since we have not taken into account systematic uncertainties.

2.4 Results

In order to detail the results of our work, we first divide our sample into turn-off stars ($T_{\mathrm{eff;\,DW}} > 5800\,\mathrm{K}$), subgiant stars ($5100\,\mathrm{K} < T_{\mathrm{eff;\,SUB}} < 5800\,\mathrm{K}$), and giant stars ($T_{\mathrm{eff;\,RGB}} < 5100\,\mathrm{K}$); in Fig. 2.6 we plot the mean [X/H] abundances for the three groups. In Fig. 2.7 and Fig. 2.8 we plot LTE and non-LTE abundances of individual M67 stars as a function of effective temperature. We discuss different aspects of these plots in the remainder of this section.

Table 2.1:: Comparison of solar abundances with respect to the standard composition of MARCS model atmospheres.

Element	Non-LTE	LTE	Grevesse et al. (2007)
Li	1.00 ± 0.04	0.99 ± 0.04	1.05 ± 0.10
O	8.69 ± 0.09	8.87 ± 0.10	8.66 ± 0.05
Na	6.16 ± 0.03	6.33 ± 0.04	6.17 ± 0.04
Mg	7.62 ± 0.02	7.59 ± 0.02	7.53 ± 0.09
Al	6.43 ± 0.02	6.46 ± 0.02	6.37 ± 0.06
Si	7.46 ± 0.02	7.47 ± 0.02	7.51 ± 0.04
Fe	7.44 ± 0.03	7.42 ± 0.03	7.45 ± 0.05
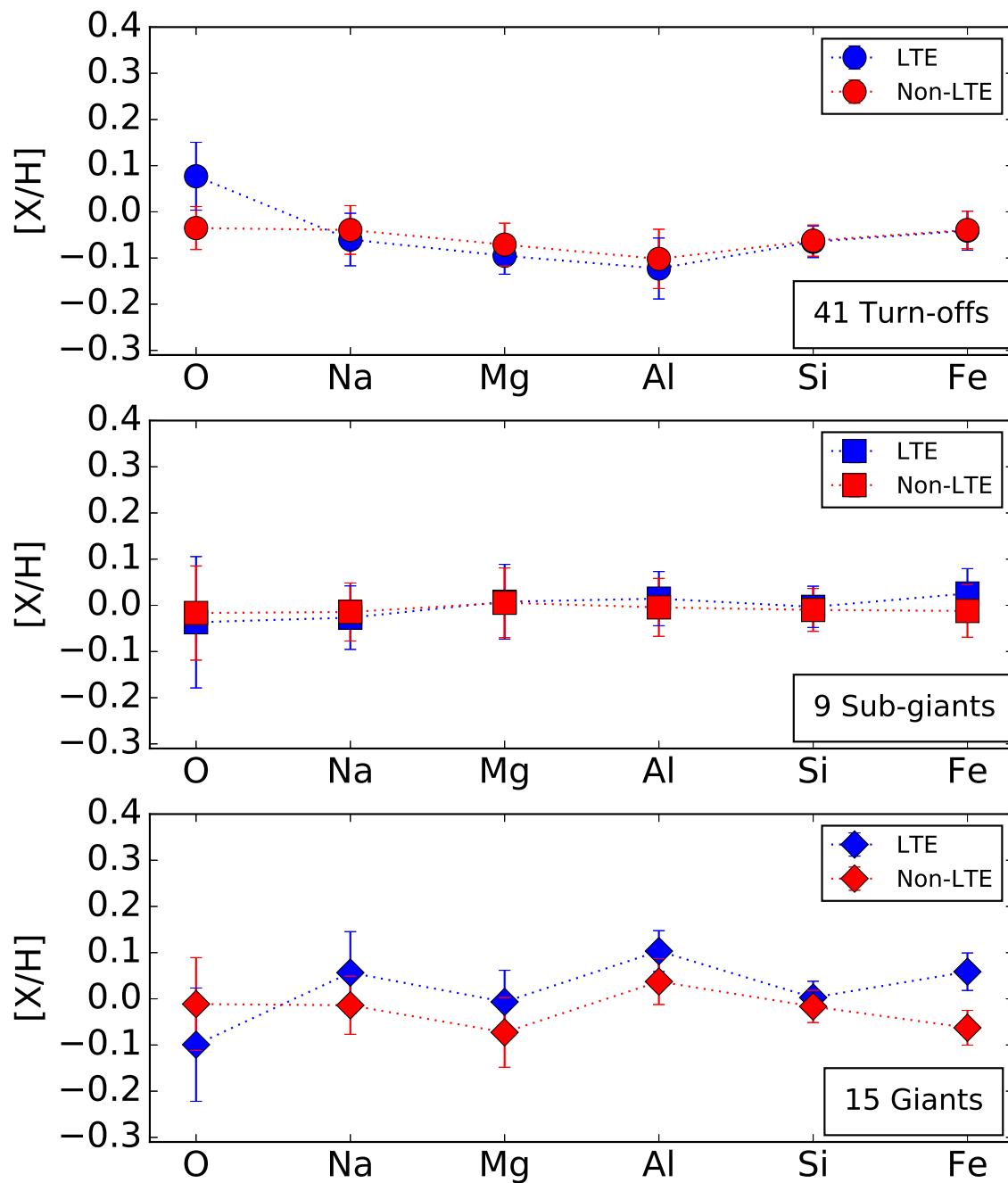
Figure 2.6: **Abundance patterns of turn-off, subgiant and giant stars in our final sample.** LTE/non-LTE [X/H] values were calculated consistently by treating iron in LTE/non-LTE when determining the stellar parameters, and by using our LTE/non-LTE solar reference values. Each symbol represents the mean abundance [X/H] of that group stars, and the error bars correspond to the standard deviation in that group.
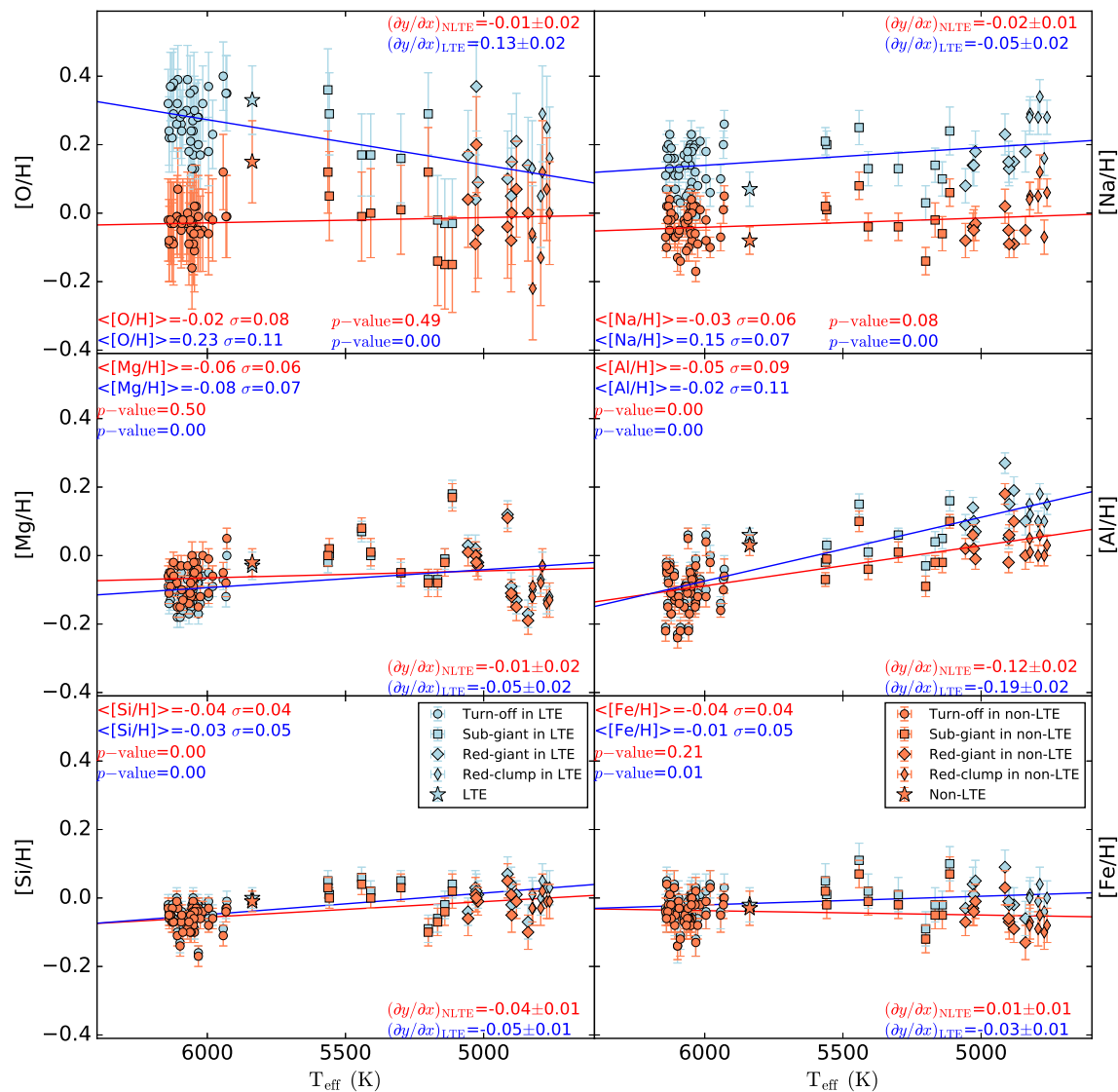
Figure 2.7: **LTE and non-LTE abundances as a function of effective temperature for individual member stars of M67.** All LTE and non-LTE abundances shown here were calculated by treating iron in non-LTE when determining the stellar parameters, and were put onto a relative ([X/H]) scale using our non-LTE solar reference. Stars with different evolutionary states are marked using different symbols. The p-values of the trends in LTE and non-LTE are shown in the legends, where a small value (typically p-value $\lesssim 0.05$) is indicative that the trend is significant with respect to the scatter. Beyond that, we also list all the gradients (times by 1000) of weighted linear fitting lines with the standard errors.
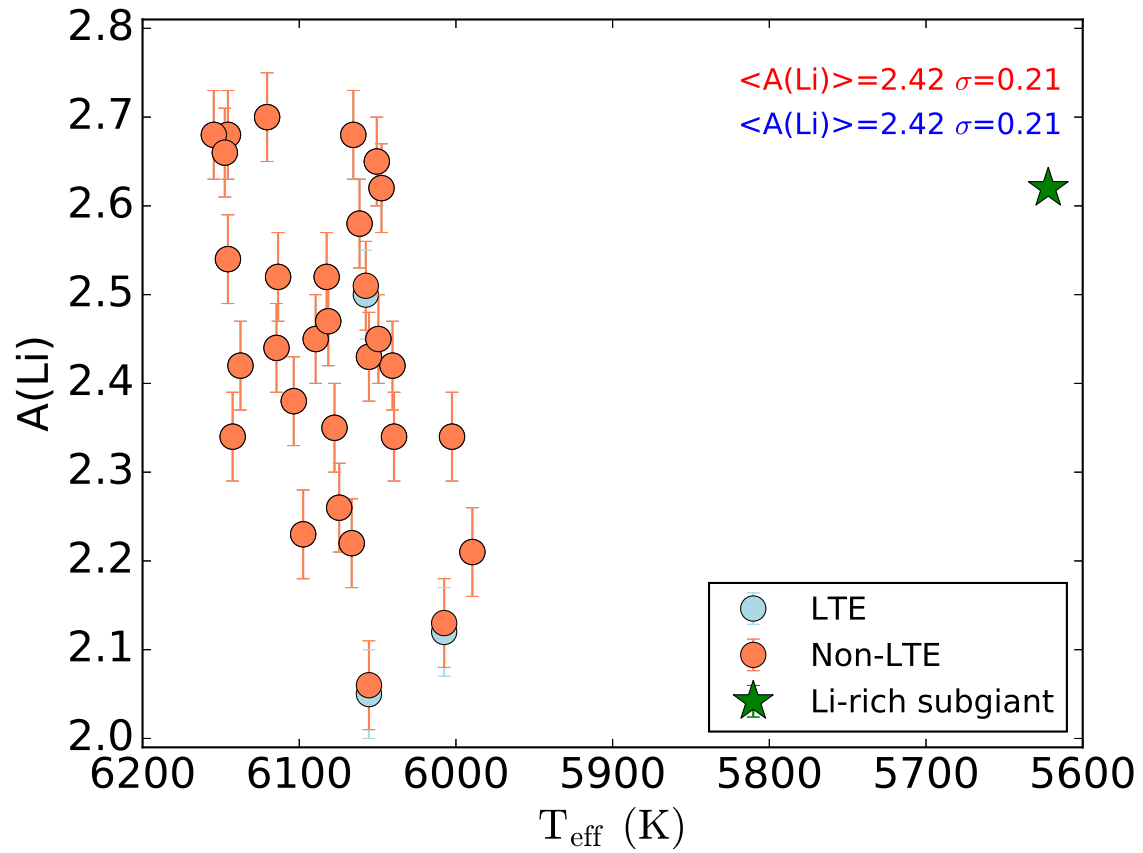
Figure 2.8: **Absolute abundance distributions of lithium as a function of effective temperature.** A lithium-rich subgiant located in a binary system, which we ruled out via our our radial velocity criterion, is marked using an asterisk.

2.4.1 Influence of departures from LTE

In Fig. 2.6 we compare the mean LTE and non-LTE [X/H] abundances for three groups of cluster stars: turn-off stars, subgiant stars, and giant stars. These were calculated consistently by treating iron in LTE/non-LTE when determining the stellar parameters, and by using our LTE/non-LTE solar reference values. Note that part of the absolute NLTE effect on chemical abundances is therefore cancelled and only the differential NLTE effects with respect to the Sun are shown in this plot.

For the turn-off stars, under the assumption of LTE, we find a large overabundance in [O/H] of more than 0.15 dex, compared to the other species. This is caused by the non-LTE effect for O I increasing in magnitude with increasing effective temperature. However, under non-LTE, the abundance ratios [X/H] for all elements are generally consistent with each other at slightly sub-solar values. For the subgiant stars, both LTE and non-LTE abundance results are generally consistent with each other. This group also gives results that are closer to the expected solar abundances (i.e. [X/H] = 0) than the other two groups. For the giant stars, the non-LTE abundances are generally lower than the LTE values, and slightly more consistent with a uniform solar composition.

In Fig. 2.7 we show LTE and non-LTE abundances as a function of effective temperature for individual member stars of M67. Here, both LTE and non-LTE abundances were calculated by treating iron in non-LTE when determining the stellar parameters, and were put onto a relative ([X/H]) scale using our non-LTE solar reference. This illustrates the departures from LTE in the absolute abundances, as a function of effective temperature. We discuss the departures from LTE for different elements separately, in the following subsections.

- **Lithium:**

Lithium abundances were determined from the resonance Li I 670.8 nm doublet. For lithium-poor stars (A(Li) < 2), it was impossible to obtain lithium abundances, because of the very weak line strength. Most stars cooler than 5900 K fall into this category, as they have suffered strong lithium depletion; an added complication in cooler stars is that the doublet is seriously blended with a nearby Fe I line. We found one exception at $T_{\text{eff}} \approx 5600$ K, a lithium-rich subgiant (Sect. 2.4.2). This star was among those that were rejected as members via the radial velocity criterion. The lithium abundances in the sample are largely insensitive to departures from LTE (see Fig. 2.8), and the mean Li abundances for non-LTE and LTE calculations are identical and have the same standard deviation: A(Li) = 2.42 ± 0.21.

The scatter around the mean lithium abundances (for those warmer stars in which the doublet could be measured) is large (0.21 dex). This observed spread in our lithium abundance for stars around the solar mass range has also been reported by other M67 studies (Pasquini et al. 2008; Pace et al. 2012). The fundamental parameters of these turn-off stars (mass, metallicity and age) should be similar; it is possible however that they were born with different initial angular momenta, which is one of the key parameters for rotational mixing, leading to different lithium depletions between these otherwise similar stars (Pinsonneault 2010).

All of the turn-offs in the M67 sample in which we detect lithium have effective temperatures larger than $T_{\rm eff} \approx 5900\,$K; in these hot turn-off layers, the combination of overpopulation in the Li ground state and superthermal source function make the non-LTE abundance corrections approximately zero for this line (e.g. Lind et al. 2009a).

- **Oxygen:**

Oxygen abundances were determined from the O I infra-red triplet, with its three components located at $777.19\,$nm, $777.42\,$nm, and $777.54\,$nm, respectively. The mean non-LTE and LTE abundances of oxygen are $[\mathrm{O/H}]_{\rm NLTE} = -0.02 \pm 0.08$ and $[\mathrm{O/H}]_{\rm LTE} = 0.23 \pm 0.11$. The difference between the oxygen abundances using non-LTE and LTE synthesis are large ($\Delta_{\rm non-LTE-LTE} \approx -0.25\,$dex). The small line strengths in giant stars and imperfect correction for telluric contamination result in larger star-to-star scatter compared to the other elements studied here, even when LTE is relaxed.

The departures from LTE are mainly due to photon losses in the lines themselves, which leads to an overpopulation of the metastable lower level, and the increased line opacity strengthens the line in non-LTE (e.g. Kiselman 1993; Takeda 2003; Amarsi et al. 2016a). As clearly seen in Fig. 2.7, the non-LTE abundance corrections are larger in turn-offs (at higher $T_{\rm eff}$) than in giants (at lower $T_{\rm eff}$). This is expected, because the oxygen triplet gets stronger with effective temperature, increasing the photon losses in the lines themselves and hence making the departures from LTE more severe.

- **Sodium:**

Sodium abundances were determined from the Na I doublet, its components located at $568.26\,$nm and $568.82\,$nm. Additionally, the Na I ($475.18\,$nm) line was available for a part of the sample. The mean non-LTE and LTE abundances of sodium are

$[\text{Na/H}]_{\text{NLTE}} = -0.03 \pm 0.06$ and $[\text{Na/H}]_{\text{LTE}} = 0.15 \pm 0.07$. Non-LTE effects evidently play an important role in Na line formation and cause a substantial negative correction ($\Delta_{\text{non-LTE-LTE}} \approx -0.18\,\text{dex}$).

The departures from LTE in optical Na I lines are largely driven by photon suction in strong lines, in particular the Na D resonance lines (Na I 588.9 nm and Na I 589.5 nm). A recombination ladder from the Na II reservoir tends to cause overpopulations of lower states and subthermal source functions, resulting in negative abundance corrections that are strongest for saturated lines (e.g. Lind et al. 2011).

- **Magnesium:**

Magnesium abundances were determined from three lines; Mg I (473.30 nm), the Mg I (571.11 nm), and the Mg I (769.16 nm). The mean non-LTE and LTE abundances of magnesium are $[\text{Mg/H}]_{\text{NLTE}} = -0.06 \pm 0.06$ and $[\text{Mg/H}]_{\text{LTE}} = -0.08 \pm 0.07$. Although the impact of departures from LTE is not very pronounced on the mean abundances, it is interesting to note there is still a clear influence on the abundance trends. This is because the giants tend to have negative abundance corrections, whereas the turn-offs tend to have positive abundance corrections.

The physical non-LTE effect is different in turn-offs and giants. In turn-off stars, the photoionisation rates for the lower Mg I levels are substantial, which can lead to overionisation, resulting in positive non-LTE abundance corrections. In contrast, in giant stars, Mg I lines (especially the Mg I 571.11 nm line) suffer from photon losses, making the abundance corrections negative (e.g. Osorio et al. 2015; Bergemann et al. 2017).

- **Aluminum:**

Aluminium abundances were determined using the doublet: Al I (669.6 nm) and Al I (669.8 nm). The mean non-LTE and LTE abundances of aluminium are $[\text{Al/H}]_{\text{NLTE}} = -0.05 \pm 0.09$ and $[\text{Al/H}]_{\text{LTE}} = -0.02 \pm 0.11$. The very weak aluminium lines in turn-offs cause a substantial abundance scatter. In addition, the doublet falls in a spectral region where the wavelength calibration of HERMES is of lower quality, which manifests itself in poor synthetic fits to the observed spectral lines. To improve this defect, we set radial velocity as a free parameters when carrying out spectra synthesis of aluminium; this unfortunately further contributes to the abundance scatter.

The non-LTE abundance correction are always negative and become much more severe in giants than the corrections in turn-offs. The negative sign of the corrections is due to photon suction effects, resulting in overpopulations of lower levels and subthermal source functions. These effects are strongest in giants. Towards warmer effective temperatures, the non-LTE effect starts to change: a larger supra-thermal UV radiation field means that a competing overionisation effect becomes more efficient. As such, the non-LTE abundance corrections are much less less severe in turn-offs (Nordlander & Lind 2017).

- **Silicon:**

Five silicon lines were used to determine silicon abundances: Si I (566.55 nm); Si I (569.04 nm); Si I (570.11 nm); Si I (579.31 nm), and Si I (672.18 nm). The mean non-LTE and LTE abundances of silicon are $[\text{Si/H}]_{\text{NLTE}} = -0.04 \pm 0.04$ and $[\text{Si/H}]_{\text{LTE}} = -0.03 \pm 0.05$.

The non-LTE abundance corrections for Si lines are not very pronounced, however they are always negative in this sample. Generally, photon losses in the Si I lines drives overpopulation for the lower levels and underpopulation for higher levels, which strengthen the lines in non-LTE.

- **Iron:**

Iron abundances were determined from a selection of Fe I and Fe II lines, that are listed in Buder et al. (2018). The mean non-LTE and LTE abundances of iron are $[\text{Fe/H}]_{\text{NLTE}} = -0.04 \pm 0.04$ and $[\text{Fe/H}]_{\text{LTE}} = -0.01 \pm 0.05$. Non-LTE effects cause a small negative correction ($\Delta_{\text{non}-\text{LTE}-\text{LTE}} \approx -0.03\,\text{dex}$).

Since Fe II lines are almost immune to non-LTE effects in late-type stars (at least, in 1D hydrostatic model atmospheres such as those used in this work – in 3D hydrodynamic model atmospheres this is not always the case; e.g. Amarsi et al. 2016b, Table 3), the main contribution to the difference between the mean abundances under the assumption of LTE and non-LTE comes from the Fe I lines. The traditional non-LTE effect for Fe I lines is overionisation; at solar-metallicity, however, this effect is relatively small, and photon losses in the Fe I lines as well as a general photon-suction effect are more important. We therefore see slightly negative abundance corrections. The effects are more severe in giants, where these intermediate-excitation Fe I lines are stronger.

2.4.2 Lithium-rich subgiant

Among the full sample of stars observed in the M67 field, we discovered a subgiant star (S95) with a very high lithium abundance A(Li) = 2.6 (see Fig. 2.8). However, because of its radial velocity, RV = 38.5 km s^{-1}, which is high compared to the cluster mean (see Fig. 2.3), we regard this star as a potential non-member and have excluded it from the discussion of cluster abundance trends. No other subgiant star in the sample has such a high lithium abundance, and severe lithium depletion is expected at this evolutionary stage after leaving the main sequence turn-off (Balachandran 1995; Pace et al. 2012). By checking the position and magnitude information, this star has been confirmed as a spectroscopic binary in the SIMBAD.

Canto Martins et al. (2006) also reported a lithium-rich subgiant star S1242 with (A(Li) = 2.7). S1242 has been verified as a member of a large eccentricity binary system in M67, with a faint low-mass dwarf companion providing negligible contribution to the luminosity (Sanders 1977; Mathieu et al. 1990). Canto Martins et al. (2006) proposed that high chromospheric activity and unusually high rotational velocity of S1242 may be induced by tidal interaction, which could help the star conserve its lithium abundance from the turn-off stage. Interestingly, Önehag et al. (2014) also found a lithium-rich subgiant star S1320 with A(Li) = 2.3. This subgiant has been included in their membership, since they did not find any evidence that this star has been contaminated by a companion. It is worth to follow up these stars, as the identification of these stars should prove useful for providing insight into the processes in binaries that can affect the surface abundances.

2.4.3 Abundance trends

As illustrated in Fig. 2.7, we have found abundance trends with effective temperature for some elements. The trends are more pronounced when LTE is assumed; furthermore, the scatter around the mean for oxygen becomes more pronounced when LTE is assumed. Even under the assumption of non-LTE, however, there still exist some systematic abundance differences between turn-offs, subgiants and giants, as can be seen in Fig. 2.7.

To determine if there is a significant correlation between element abundance and effective temperature, we calculate p-values in the linear regression analysis by assuming there is no correlation between these two parameters in the null hypothesis. The p-values of the trends are shown in the legends of Fig. 2.7, where a small value (typically p-value $\lesssim 0.05$) is indicative that the trend is significant with respect to the scatter. We can thus say that, under the assumption of LTE, the trends in

surface abundance against effective temperature are significant with respect to the scatter, for all of the species shown in Fig. 2.7. In contrast, under the assumption of non-LTE, the trends for oxygen, sodium, magnesium and iron are not significant with respect to the scatter, while for aluminium and silicon the trends remain significant. We further note an obvious deviation from the linear trend in the behaviour of Mg abundance with effective temperature; subgiants appear overabundant with respect to the linear trend and red giants underabundant.

In summary, non-LTE analysis tends to flatten the trends with effective temperature seen in LTE, which reduces the scatter in mean abundance for all the elements, when the full sample is considered. The remaining residual trends may reflect other systematic errors still present in the analysis or be intrinsic to the cluster. We shall consider this in more detail in Sect. 2.5.

2.5 Discussion

2.5.1 Comparison with atomic diffusion models

Atomic diffusion is a continuous process whose influence immediately below the outer convection zone causes surface abundance variations during the main-sequence phase of a star. At the turn-off point, where the convective envelope is the thinnest, the settling of elements reaches a maximum. As the star evolves along the subgiant branch and red giant branch, the surface abundances begin to recover gradually to the initial value due to the enlarged surface convection zone, except for those light elements that are affected by nuclear processing.

The metals in our Sun are thought to be underabundant relative to the initial bulk composition, by about 0.04 dex (e.g. Asplund et al. 2009). Turcotte et al. (1998) demonstrated that the diffusive process is dominant at the end of the main-sequence phases of solar-type stars, thus the turn-off stars in M67 with comparable age to the Sun may show even larger effects of atomic diffusion. Larger effects are also expected in warm metal-poor stars, because of their older ages and thinner surface convection zones (Michaud et al. 1984).

Our sample includes stars in different evolutionary states, including main-sequence, turn-off, subgiant, red-giant and red-clump stars. It is therefore of interest to compare our results with those predicted by stellar evolutionary models that include atomic diffusion. We adopted the surface abundances that were calculated in Dotter et al. (2017) with solar metallicity, initial masses ranging from $0.5 M_\odot$ to

$1.5 \mathrm{M}_\odot$ and ages of $t = 4.0 \, \mathrm{Gyr}$, $t = 4.5 \, \mathrm{Gyr}$ and $t = 5.0 \, \mathrm{Gyr}$, respectively. The stellar evolutionary models (MIST; Dotter 2016; Choi et al. 2016) have included atomic diffusion, overshooting mixing and turbulent diffusion. Furthermore, the models are calculated with radiative acceleration, which acts differently on different chemical species and can thus potentially explain different abundance trends for the different elements under consideration.

In Fig. 2.9 and Fig. 2.10, we overplot the stellar evolutionary models on our results for the surface abundances versus effective temperature and gravity, respectively. Since Al has been neglected in the model output, models of Al are not shown in the model-data comparison. We note that Al is expected to behave similarly to the other elements (see e.g. Bertelli Motta et al. 2018). We thus overplot the models of Mg on the Al measurements instead. Since the zero-points of the models are not relevant here, and we are more interested in the effect of atomic diffusion on their relative surface abundances, small arbitrary offsets have been applied to all the model abundances so as to generally match our abundance measurements for the turn-off stars.

Fig. 2.10 most clearly illustrates the evolutionary effects predicted by the models; the model abundances decrease on the main-sequence with increasing mass to reach a minimum around the turn-off; the severity of this depletion is age-dependent, being more severe for older ages. Moving to later evolutionary stages (lower surface gravity and effective temperature), the elements are brought back up to the surface by convective mixing (i.e. the first dredge-up), and the surface abundance depletion becomes less severe. At the base of the red giant branch, the surface abundances are restored to the original composition; the models actually predict a slight increase in the surface abundances over the initial values as a result of hydrogen being consumed during central H-burning.

We now highlight some interesting aspects evident from the comparison between our observed abundances and the model predictions in Fig. 2.10. We note that the initial decrease with increasing mass cannot be tested with our data, since there are too few main sequence stars. However, there is a satisfying morphological agreement with the models in the dredge-up pattern from the turn-off to the subgiant branch. However, our abundance measurements of the red-giant and red-clump stars (with effective temperature less than $5100 \, \mathrm{K}$) do not fit the predicted trend very well, even considering the abundance errors, for all elements except possibly Al. One possible reason for this discrepancy could be that the stellar parameters for these giant stars are poorly determined (see Fig. 2.2). Problems in the main stellar parameters will propagate the systematic offsets to the individual stellar abundances. However, this can not be the single contribution to explain this discrepancy, since the systematic

offsets propagating to different elements may have different correction directions.

2.5.2 Comparison to other studies

In this section, we compare our abundance results to previous high-resolution studies of M67. Table 2.2 summarises the target selection and spectroscopic quality for seven literature studies. We also include the mean abundance ratios determined in those studies. We compare these results, which were mainly based on equivalent-widths and under the assumption of LTE, with our own results, which are based on spectral line fitting and under non-LTE.

Our mean [Fe/H] value in non-LTE for M67 is consistent with the value of Tautvaišiene et al. (2000), Önehag et al. (2014) and Bertelli Motta et al. (2018), but is slightly lower than those determined from the other studies shown in Table 2.2. Generally all the results are comparable with solar metallicity to within their respective errors. However, some disagreements between other measured abundances from different studies do exist.

Overall, our abundance ratios in non-LTE are close to solar, and are systematically lower than those studies wherein only giants have been analyzed, namely Tautvaišiene et al. (2000), Yong et al. (2005), Pancino et al. (2010) and Friel et al. (2010). The abundance results that are mainly based on unevolved stars from Randich et al. (2006), Pace et al. (2008), Önehag et al. (2014), Bertelli Motta et al. (2018) and Souto et al. (2018) are more consistent with those presented in this work.

The differences in the abundances determined in this work and those presented elsewhere could be the result of a variety of factors, including the choice of atmospheric model, abundance calculation code, the determined stellar parameters, the choice of $\log gf$ values and line lists, the choice of solar reference abundances and non-LTE effects. In this work, all of the abundances are determined by spectrum synthesis, which are more reliable and accurate, especially when the lines are blended, than the traditional equivalent width analysis. We note, too, that our results benefit from being based on the largest sample of high-quality spectra yet published, covering turn-off, subgiant star, red giant and red clump stars compared with other studies, whose abundances are derived based on a smaller number of objects.

We compare the results of Önehag et al. (2014) with those presented in this work in Fig. 2.11. Önehag et al. (2014) analysed 14 turn-offs and subgiants using high resolution spectra ($R \approx 50,000$), an analysis based on equivalent-widths and under the assumption of LTE. Their abundances were derived for each spectral
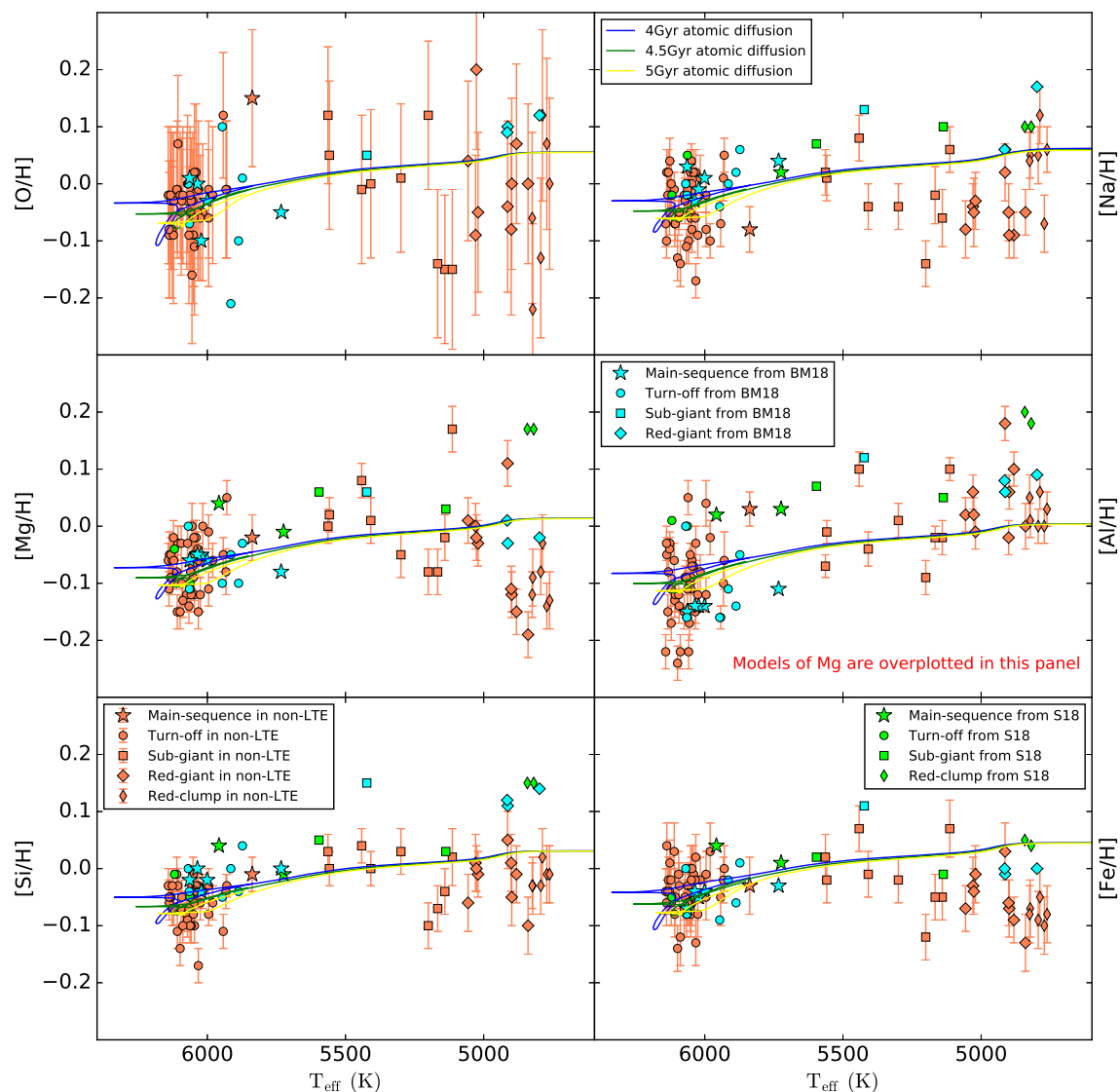
Figure 2.9: **Non-LTE Abundances [X/H] as a function of effective temperature for individual M67 stars.** We overplot surface abundance isochrones from atomic diffusion models with solar metallicity and different evolution ages. Al is not shown in the model-data comparison, since it has been neglected in the model output. Instead, we overplot the models of Mg on the Al measurements. We also overplot the abundance results from Souto et al. (2018) and Bertelli Motta et al. (2018). Stars in different evolutionary states are marked with different symbols.
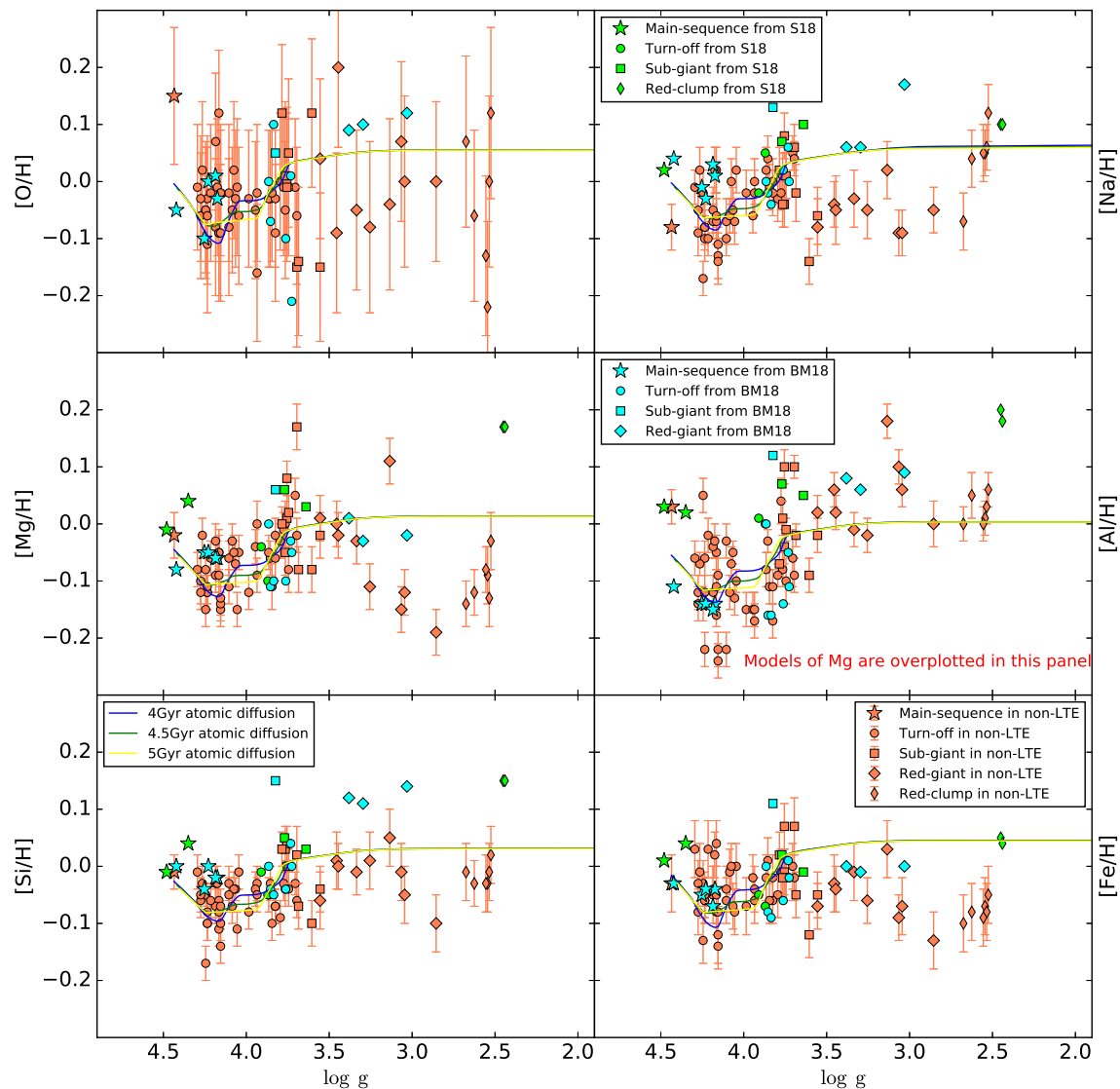
Figure 2.10: **Non-LTE Abundances** [X/H] **as a function of** $\log g$ **for individual M67 stars.** We overplot surface abundance isochrones from atomic diffusion models with solar metallicity and different evolution ages. Al is not shown in the model-data comparison, since it has been neglected in the model output. Instead, we overplot the models of Mg on the Al measurements. We also overplot the abundance results from Souto et al. (2018) and Bertelli Motta et al. (2018). Stars in different evolutionary states are marked with different symbols.

Table 2.2:: The comparison of average abundances in common for M67 based on high resolution spectroscopy. The total number of stars analyzed in each study is given by #.

	#	R	SNR	[Fe/H]	[O/Fe]	[Na/Fe]	[Mg/Fe]	[Al/Fe]	[Si/Fe]
NLTE[1]	66	42000	50–150	−0.04 ± 0.04	+0.04 ± 0.09	−0.03 ± 0.05	+0.00 ± 0.05	+0.01 ± 0.07	+0.02 ± 0.03
T00[2]	9	30000–60000	≥ 100	−0.03 ± 0.03	+0.02 ± 0.06	+0.19 ± 0.06	+0.10 ± 0.04	+0.14 ± 0.04	+0.10 ± 0.05
Y05[3]	3	28000	30–100	+0.02 ± 0.14	+0.07 ± 0.05	−0.30 ± 0.10	+0.16 ± 0.08	+0.17 ± 0.05	+0.09 ± 0.11
R06[4]	10	45000	90–180	+0.03 ± 0.03	+0.01 ± 0.03	+0.05 ± 0.07	+0.00 ± 0.02	−0.05 ± 0.04	+0.02 ± 0.04
P08[5]	6	100000	≃ 80	+0.03 ± 0.04	−0.07 ± 0.09	−0.02 ± 0.07	-	−0.03 ± 0.11	−0.03 ± 0.06
P10[6]	3	30000	50–100	+0.05 ± 0.02	+0.04 ± 0.10	+0.08 ± 0.09	+0.27 ± 0.04	+0.03 ± 0.02	+0.10 ± 0.02
F10[7]	3	30000	150–180	+0.03 ± 0.07	−0.16 ± 0.05	+0.13 ± 0.10	+0.05 ± 0.03	+0.11 ± 0.07	+0.18 ± 0.04
Ö14[8]	14	50000	150	−0.02 ± 0.04	−0.02 ± 0.05	+0.02 ± 0.03	+0.02 ± 0.02	+0.02 ± 0.04	−0.01 ± 0.02
BM18[9]	15	47000	–	−0.02 ± 0.05	+0.02 ± 0.09	−0.06 ± 0.04	−0.02 ± 0.02	−0.04 ± 0.07	+0.05 ± 0.04
S18[10]	8	22500	120–956	+0.00 ± 0.04	–	+0.06 ± 0.04	+0.04 ± 0.06	+0.07 ± 0.05	+0.04 ± 0.04

Notes. (1) This work (2) Tautvaišiene et al. (2000) analysed 6 red-clump stars and 3 giant stars. (3) Yong et al. (2005) analysed 3 red-clump stars. (4) Randich et al. (2006) analysed 8 dwarfs and 2 slightly evolved stars. (5) Pace et al. (2008) analysed 6 main-sequence stars. (6) Pancino et al. (2010) analysed 3 red-clump stars. (7) Friel et al. (2010) analysed 3 red-clump stars. (8) Önehag et al. (2014) analysed 14 stars whose 6 are located on the main-sequence, 3 are at the turn-off point, and 5 are on the early subgiant branch. (9) Bertelli Motta et al. (2018) analysed 15 stars whose 5 are located on the main-sequence, 6 are at the turn-off phase, 1 are on the subgiant branch and 3 are on the red-giant branch. (10) Souto et al. (2018) analysed 8 stars, including two main-sequence stars, two turn-off stars, two subgiants and two red-clump stars

line individually relative to those of the solar proxy M67-1194. Our mean chemical abundances are typically lower than the ones from Önehag et al. (2014). However, in that work as well as our own, we find that the abundances in subgiants are enhanced relative to those in turn-offs. This enhancement is smaller in the results of Önehag et al. (2014) than in this work; this may be because the subgiants used in that work are located very close to the turn-off, whereas here they span the full subgiant branch. These overall increasing abundances from turn-offs to subgiants could be a signature for possible diffusion process (Sect. 2.5.1).

Recent studies by Bertelli Motta et al. (2018) and Souto et al. (2018) both investigated the presence of atomic diffusion effects in M67 by analysing the member stars across different evolutionary phases. We overplot their results in Fig. 2.9 and Fig. 2.10. Their inferred abundance patterns show an overall agreement with the atomic diffusion models from Dotter et al. (2017) and their abundance distributions for turn-off and subgiant stars are generally consistent with our non-LTE results, with some notable exceptions. We note that the other two studies show no evidence of low abundances for red giants compared to less evolved stars, as seen in our data for O, Na, Mg, and Fe. This reinforces our suspicion that our giant star abundances are not accurate (see Sect. 2.5.1)

Looking at individual elements, the measured [O/H] from Bertelli Motta et al. (2018) also presents a fairly large scatter, which the authors ascribe to telluric blending and weakness of the [OI] line at 630nm. However, this line is not expected to suffer large non-LTE effects and the agreement with our non-LTE abundances is significantly better than with our LTE abundances. The LTE [Na/H] abundances derived by the other two groups are consistently somewhat higher than our non-LTE abundance trend and Bertelli Motta et al. (2018) estimate that their Na LTE abundances are indeed overestimated by 0.1-0.15 dex. The [Mg/H] abundances agree well for unevolved stars, while the red giants show a disagreement of > 0.2 dex between the three groups, which cannot be attributed to non-LTE effects. For [Al/H], our abundances tend to fall between results of the other two groups, but there is satisfactory agreement on the increasing abundance trend with evolutionary phase. The [Si/H] abundances of the other two groups are higher than ours and the predicted abundance trend slightly steeper. We note that Bertelli Motta et al. (2018) suspect that their Si analysis suffers from an unknown bias, elevating the abundances in giants with respect to dwarfs. The [Fe/H] abundances are in good agreement between all three studies for turn-off stars and subgiants, but not for giants, as mentioned above.
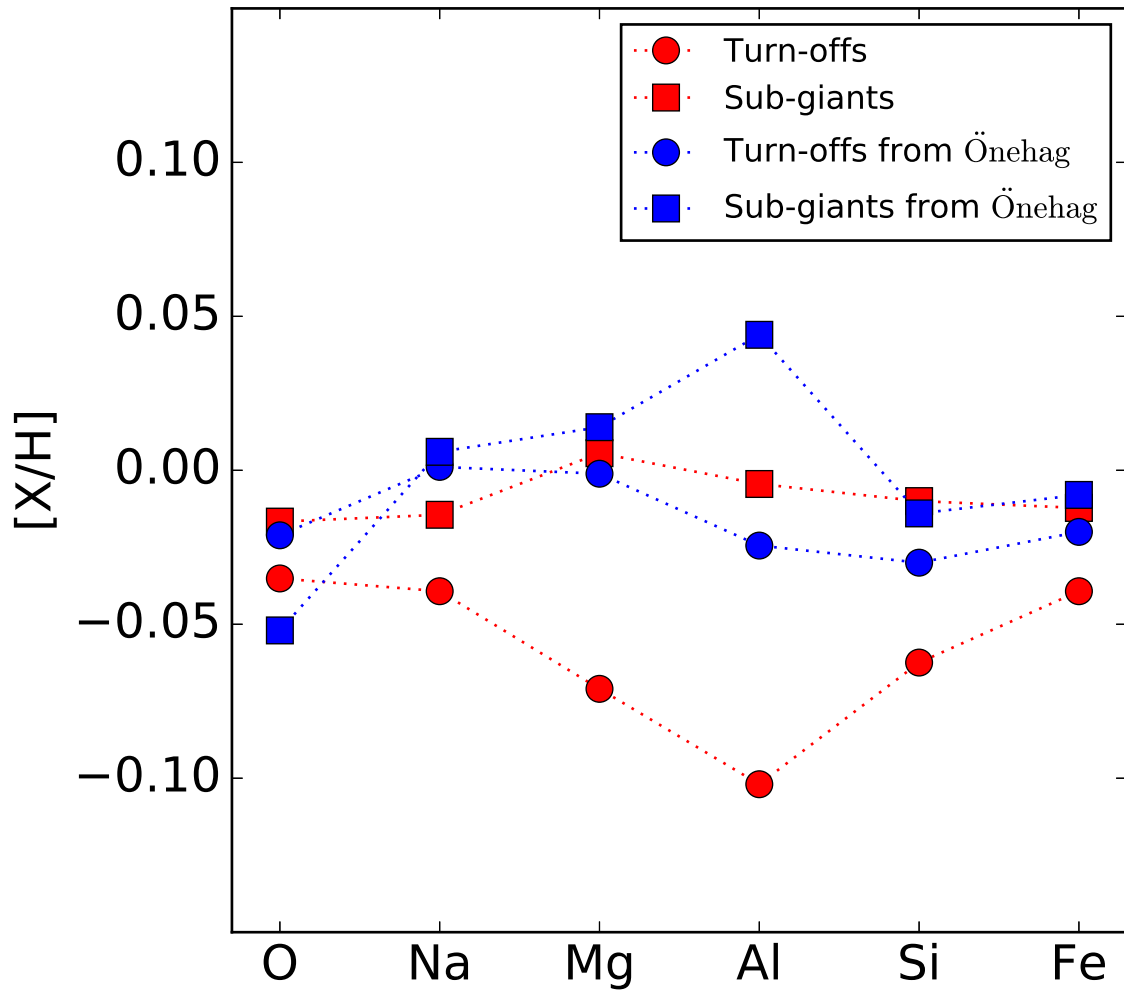
Figure 2.11: A comparison between our non-LTE abundance patterns of turn-off, subgiant and giant stars and those from Önehag's turn-off and early subgiant stars.

2.6 Conclusion

We have presented a comprehensive determination of the M67 elemental abundances of lithium, oxygen, sodium, magnesium, aluminium, silicon, and iron. We analysed lines using non-LTE and LTE calculations with 1D hydrostatic MARCS model atmospheres based on high resolution, high quality spectra from the GALAH survey.

We have accounted for non-LTE effects in the line formation of different elements. For lithium, non-LTE effects are not prominent. However, the large scatter (0.21 dex) in lithium abundances in stars with similar stellar parameters (i.e. mass, metallicity and age) may indicate that the stars in this cluster could have different initial angular momentums to which would naturally result in different levels of lithium depletion. In addition, we found a lithium-rich subgiant in our sample, which we note is a spectroscopic binary. It could be a potential candidate to study unusual lithium induced by tidal effects.

We found that the scatter in mean abundance is reduced for all the elements under the assumption of non-LTE, compared to under LTE, because non-LTE analyses flattens the trends in surface abundances with effective temperature (see Fig. 2.7). However, abundance differences between stars in different evolutionary phases are not fully erased by non-LTE effects. The star-to-star abundance scatter for similar stars appears largely unaffected by non-LTE analysis.

We compared our observed abundance trends with the trends predicted by the atomic diffusion model of Dotter et al. (2017), assuming solar metallicity and approximately solar age. Our non-LTE results match well with model prediction for turn-off stars and subgiants within the errors, however, they fail to meet the predicted trend for later phase red-giant and red-clump stars. One possible reason for this differences could be caused by the poor determination of stellar parameters for those giant stars.

To increase the accuracy of our abundance measurements further, 3D hydrodynamical model atmospheres should be considered. Such modelling is important for late type atmospheres, where the spectral line form at the top of the convective region, and eliminates the need for the artificial broadening parameters, such as microturbulence and macroturbulence. (e.g. Asplund et al. 2000). Performing a 3D non-LTE study is beyond the scope of the present work. We note however that 3D corrections for the same lines can go in opposite directions for turn-offs and giants. Consequently, it is possible that a 3D non-LTE analysis would find significantly flatter or steeper abundance trends than those presented in Sect. 2.4.3 (Korn et al. 2007).

Finally, we underline the necessity to include accurate non-LTE corrections in order to obtain more reliable abundances to study abundance evolution and chemical tagging. Our analysis shows that, due to the potential influence of both systematic abundance errors and of stellar evolution effects, the method of connecting stars in the field to a common birth location by chemical similarity is significantly more reliable for stars in the same evolutionary phase.

Table 2.3:: Fundamental parameters of the sample stars from the spectroscopic analysis of GALAH data. The columes from left to right show the GALAH ID, the star identifier in the 2MASS catalogue, the type of the star,the effective temperature, the surface gravity, the stellar metallicity, the micro-turbulence, the projected surface rotational velocity and radial velocity. Note that $v \sin \iota$ is actually a combined measurement from both $v \sin \iota$ and v_{mac}, since they have a degenerate influence effect on spectral line broadening and cannot been disentangled.

GALAH ID	2MASS ID	Group	T_{eff} (K)	$\log g$	Metallicity	ξ (km s^{-1})	$v \sin \iota$ (km s^{-1})	RV (km s^{-1})
6561552	08505344 + 1144346	Main-sequence	5837	4.43	−0.05	0.93	8.81	34.65
6560101	08511833 + 1143251	Turn-off	6141	4.11	−0.07	1.07	7.70	34.06
6577714	08514522 + 1156552	Turn-off	6138	4.11	−0.08	1.09	8.30	34.62
6554484	08514493 + 1138589	Turn-off	6137	4.16	0.01	1.08	7.68	33.36
6577148	08505439 + 1156290	Turn-off	6133	3.93	−0.08	1.08	9.20	33.97
6569011	08511534 + 1150143	Turn-off	6131	3.87	−0.05	1.08	9.15	34.14
6565966	08504766 + 1147525	Turn-off	6127	4.18	−0.06	1.08	7.76	34.85
6565326	08511476 + 1147238	Turn-off	6126	3.86	−0.03	1.08	9.54	35.38
6574584	08514122 + 1154290	Turn-off	6122	3.82	−0.07	1.07	10.32	34.50
6571679	08512830 + 1152175	Turn-off	6121	3.82	−0.11	1.07	8.85	34.49
6567547	08514082 + 1149055	Turn-off	6110	4.30	0.02	1.05	8.35	34.54
6555602	08505973 + 1139524	Turn-off	6108	4.05	−0.10	1.07	7.07	33.75
6561039	08514597 + 1144093	Turn-off	6106	4.18	−0.08	1.06	9.09	33.75
6570179	08505474 + 1151093	Turn-off	6098	4.16	−0.15	1.05	7.40	34.61
6564123	08514641 + 1146267	Turn-off	6094	4.09	−0.04	1.05	8.91	34.53
6573044	08513119 + 1153179	Turn-off	6092	4.28	−0.07	1.02	7.37	34.02
6575508	08505762 + 1155147	Turn-off	6088	4.16	−0.14	1.03	7.94	34.19
6558150	08514465 + 1141510	Turn-off	6074	3.98	−0.12	1.03	9.18	33.18
6568768	08513923 + 1150038	Turn-off	6071	3.79	−0.11	1.04	14.49	36.38
6573727	08505600 + 1153520	Turn-off	6066	4.16	−0.11	1.03	7.85	35.18
6573191	08512742 + 1153265	Turn-off	6062	3.84	−0.10	1.04	7.89	33.98
6572337	08512015 + 1152479	Turn-off	6060	4.24	−0.03	1.05	7.83	34.24
6569861	08510857 + 1150530	Turn-off	6058	4.24	−0.09	1.03	7.21	35.74
6564445	08512205 + 1146409	Turn-off	6055	3.93	−0.08	1.04	9.63	35.61
6567617	08512595 + 1149089	Turn-off	6052	4.07	−0.10	1.02	9.09	35.12
6559497	08511810 + 1142547	Turn-off	6051	4.05	−0.03	1.04	7.12	34.15
6568479	08520785 + 1149500	Turn-off	6050	4.16	−0.10	1.04	8.72	33.72
6572560	08515963 + 1152576	Turn-off	6048	3.69	−0.07	1.02	8.48	34.32
6572187	08512552 + 1152388	Turn-off	6046	4.07	−0.02	1.03	7.53	34.95
6560653	08513012 + 1143498	Turn-off	6046	4.24	−0.09	1.02	8.19	34.35
6567233	08511164 + 1148505	Turn-off	6040	4.26	−0.02	1.02	6.58	36.38
6569167	08520741 + 1150221	Turn-off	6034	3.94	−0.05	1.02	8.23	35.22
6565967	08510156 + 1147501	Turn-off	6032	4.18	−0.01	1.02	6.68	33.59
6562672	08504760 + 1145228	Turn-off	6032	4.24	−0.16	1.00	6.46	34.56
6571851	08510492 + 1152261	Turn-off	6025	4.28	−0.10	1.01	6.95	35.13
6568307	08514914 + 1149435	Turn-off	6016	3.76	−0.06	1.01	8.38	34.80
8436138	08504976 + 1154244	Turn-off	5995	4.24	−0.09	0.99	6.64	33.53
6571594	08505569 + 1152146	Turn-off	5995	3.77	−0.04	1.00	7.53	34.62
6579199	08520330 + 1158046	Turn-off	5980	4.22	0.01	0.99	6.64	33.66
6562188	08512080 + 1145024	Turn-off	5942	4.16	−0.08	0.96	8.51	35.09
6567847	08511854 + 1149214	Turn-off	5932	3.74	−0.06	0.97	7.35	35.08
6563234	08510325 + 1145473	Turn-off	5929	3.70	−0.03	0.98	6.72	35.63
9077970	08513540 + 1157564	Subgiant	5563	3.78	−0.01	0.89	7.00	33.71
6568921	08510106 + 1150108	Subgiant	5558	3.74	−0.05	0.89	6.49	33.23
6574583	08510018 + 1154321	Subgiant	5441	3.75	0.04	0.90	7.18	34.13
6562991	08521134 + 1145380	Subgiant	5408	3.75	−0.03	0.91	7.40	33.40
6569862	08511564 + 1150561	Subgiant	5299	3.76	−0.04	0.93	6.16	34.51
6567693	08504994 + 1149127	Subgiant	5200	3.61	−0.15	0.97	6.19	34.21
6577630	08514883 + 1156511	Subgiant	5166	3.68	−0.05	0.98	8.01	34.92
6562765	08512935 + 1145275	Subgiant	5140	3.55	−0.07	1.00	6.74	33.81
6569012	08515611 + 1150147	Subgiant	5113	3.69	0.07	1.04	7.41	35.89
6571766	08505816 + 1152223	Red-giant	5056	3.55	−0.08	1.05	5.85	34.58
6565104	08510839 + 1147121	Red-giant	5029	3.45	−0.04	1.06	5.52	34.27
6579331	08511897 + 1158110	Red-giant	5026	3.44	−0.04	1.07	6.47	34.69
6573364	08513577 + 1153347	Red-giant	5020	3.33	−0.05	1.07	7.07	34.76
6563655	08512156 + 1146061	Red-giant	4913	3.13	0.04	1.17	6.68	35.28
6570514	08514235 + 1151230	Red-giant	4900	3.25	−0.02	1.18	7.66	34.85
6568851	08514234 + 1150076	Red-giant	4898	3.04	−0.05	1.17	7.68	34.73
6565879	08514507 + 1147459	Red-giant	4881	3.06	−0.07	1.19	7.49	32.79
6569711	08511704 + 1150464	Red-giant	4839	2.86	−0.12	1.24	6.46	34.35
6575356	08515952 + 1155049	Red-clump	4824	2.62	−0.08	1.23	7.78	35.38
6577481	08514388 + 1156425	Red-clump	4822	2.54	−0.08	1.21	7.56	33.82
6573728	08512618 + 1153520	Red-clump	4793	2.55	−0.10	1.24	6.98	34.90
6566179	08512280 + 1148016	Red-clump	4787	2.52	−0.06	1.25	7.55	34.23
6569393	08512898 + 1150330	Red-clump	4771	2.67	−0.08	1.28	7.48	34.20
6572270	08511269 + 1152423	Red-clump	4761	2.53	−0.11	1.24	6.94	35.14

Table 2.4:: Non-LTE chemical abundances of the sample stars in M67. Abundances were derived relative to non-LTE values of solar analysed in this work.

GALAH ID	Group	A(Li)$_{\mathrm{NLTE}}$	[O/H]$_{\mathrm{NLTE}}$	[Na/H]$_{\mathrm{NLTE}}$	[Mg/H]$_{\mathrm{NLTE}}$	[Al/H]$_{\mathrm{NLTE}}$	[Si/H]$_{\mathrm{NLTE}}$	[Fe/H]$_{\mathrm{NLTE}}$
6561552	Main-sequence	–	0.15 ± 0.12	-0.08 ± 0.04	-0.02 ± 0.04	0.03 ± 0.03	-0.01 ± 0.03	-0.03 ± 0.05
6560101	Turn-off	2.68 ± 0.05	-0.02 ± 0.12	-0.07 ± 0.04	-0.06 ± 0.03	-0.22 ± 0.03	-0.03 ± 0.03	-0.04 ± 0.04
6577714	Turn-off	2.66 ± 0.05	-0.08 ± 0.12	-0.10 ± 0.03	-0.11 ± 0.03	-0.03 ± 0.03	-0.05 ± 0.03	-0.06 ± 0.04
6554484	Turn-off	2.68 ± 0.05	-0.09 ± 0.12	0.02 ± 0.04	-0.05 ± 0.03	-0.05 ± 0.02	-0.06 ± 0.03	0.04 ± 0.04
6577148	Turn-off	–	-0.02 ± 0.11	-0.02 ± 0.04	-0.09 ± 0.04	-0.15 ± 0.03	-0.05 ± 0.03	-0.04 ± 0.04
6569011	Turn-off	2.34 ± 0.05	-0.03 ± 0.12	0.02 ± 0.04	-0.05 ± 0.03	-0.08 ± 0.03	-0.05 ± 0.03	-0.02 ± 0.04
6565966	Turn-off	2.54 ± 0.05	-0.08 ± 0.12	-0.05 ± 0.04	-0.09 ± 0.03	-0.04 ± 0.03	-0.07 ± 0.03	-0.04 ± 0.04
6565326	Turn-off	2.42 ± 0.05	-0.03 ± 0.12	0.04 ± 0.04	-0.06 ± 0.03	-0.03 ± 0.02	-0.03 ± 0.03	0.01 ± 0.04
6574584	Turn-off	–	-0.09 ± 0.12	-0.02 ± 0.04	-0.02 ± 0.03	-0.11 ± 0.03	-0.07 ± 0.03	-0.02 ± 0.04
6571679	Turn-off	–	-0.03 ± 0.12	0.00 ± 0.04	-0.06 ± 0.04	-0.17 ± 0.03	-0.07 ± 0.03	-0.06 ± 0.04
6567547	Turn-off	2.52 ± 0.05	-0.01 ± 0.12	-0.01 ± 0.04	-0.08 ± 0.03	-0.06 ± 0.03	-0.01 ± 0.03	0.03 ± 0.04
6555602	Turn-off	–	-0.01 ± 0.12	-0.07 ± 0.04	-0.15 ± 0.03	-0.13 ± 0.03	-0.11 ± 0.03	-0.08 ± 0.05
6561039	Turn-off	2.70 ± 0.05	0.07 ± 0.11	-0.07 ± 0.04	-0.03 ± 0.03	-0.12 ± 0.03	-0.03 ± 0.03	-0.05 ± 0.04
6570179	Turn-off	2.44 ± 0.05	-0.02 ± 0.11	-0.13 ± 0.03	-0.15 ± 0.03	-0.24 ± 0.03	-0.14 ± 0.03	-0.14 ± 0.05
6564123	Turn-off	2.38 ± 0.05	-0.05 ± 0.11	-0.06 ± 0.03	-0.03 ± 0.03	-0.12 ± 0.03	-0.07 ± 0.03	-0.01 ± 0.04
6573044	Turn-off	2.45 ± 0.05	-0.03 ± 0.12	-0.05 ± 0.04	-0.10 ± 0.03	-0.14 ± 0.03	-0.05 ± 0.03	-0.03 ± 0.05
6575508	Turn-off	2.23 ± 0.05	-0.02 ± 0.11	-0.14 ± 0.03	-0.13 ± 0.04	-0.22 ± 0.03	-0.10 ± 0.03	-0.12 ± 0.04
6558150	Turn-off	2.52 ± 0.05	-0.03 ± 0.12	-0.02 ± 0.04	-0.12 ± 0.03	-0.15 ± 0.02	-0.08 ± 0.03	-0.07 ± 0.04
6568768	Turn-off	–	0.00 ± 0.12	-0.03 ± 0.04	-0.03 ± 0.03	-0.09 ± 0.03	-0.09 ± 0.03	-0.05 ± 0.05
6573727	Turn-off	2.47 ± 0.05	-0.09 ± 0.12	-0.11 ± 0.03	-0.14 ± 0.03	-0.09 ± 0.03	-0.07 ± 0.03	-0.08 ± 0.04
6573191	Turn-off	–	-0.02 ± 0.11	-0.01 ± 0.04	-0.11 ± 0.03	-0.11 ± 0.03	-0.10 ± 0.02	-0.06 ± 0.04
6572337	Turn-off	2.35 ± 0.05	-0.05 ± 0.12	-0.02 ± 0.04	-0.08 ± 0.04	0.05 ± 0.03	-0.05 ± 0.03	-0.03 ± 0.04
6569861	Turn-off	2.26 ± 0.05	-0.03 ± 0.11	-0.10 ± 0.04	-0.12 ± 0.03	-0.22 ± 0.03	-0.10 ± 0.03	-0.06 ± 0.04
6564445	Turn-off	2.22 ± 0.05	-0.16 ± 0.12	0.00 ± 0.04	0.00 ± 0.04	-0.17 ± 0.03	-0.03 ± 0.02	-0.06 ± 0.04
6567617	Turn-off	2.68 ± 0.05	-0.03 ± 0.12	-0.05 ± 0.04	-0.07 ± 0.04	-0.05 ± 0.03	-0.04 ± 0.03	-0.07 ± 0.04
6559497	Turn-off	2.58 ± 0.05	-0.06 ± 0.12	0.02 ± 0.04	-0.05 ± 0.04	-0.10 ± 0.02	-0.01 ± 0.02	0.00 ± 0.04
6568479	Turn-off	1.71 ± 0.05	-0.09 ± 0.12	-0.06 ± 0.04	-0.09 ± 0.03	-0.11 ± 0.02	-0.08 ± 0.03	-0.08 ± 0.04
6572560	Turn-off	2.51 ± 0.05	-0.06 ± 0.12	0.04 ± 0.03	-0.02 ± 0.03	-0.09 ± 0.03	-0.06 ± 0.03	-0.02 ± 0.04
6572187	Turn-off	2.06 ± 0.05	0.02 ± 0.12	0.00 ± 0.04	-0.05 ± 0.03	-0.07 ± 0.03	-0.04 ± 0.03	0.00 ± 0.04
6560653	Turn-off	2.43 ± 0.05	-0.11 ± 0.12	-0.08 ± 0.04	-0.12 ± 0.03	-0.06 ± 0.03	-0.10 ± 0.03	-0.06 ± 0.04
6567233	Turn-off	2.65 ± 0.05	0.02 ± 0.12	0.02 ± 0.04	-0.02 ± 0.03	-0.07 ± 0.02	-0.03 ± 0.03	-0.01 ± 0.05
6569167	Turn-off	2.45 ± 0.05	-0.05 ± 0.12	-0.06 ± 0.03	-0.04 ± 0.03	-0.15 ± 0.03	-0.04 ± 0.03	-0.02 ± 0.04
6565967	Turn-off	2.62 ± 0.05	-0.01 ± 0.12	0.02 ± 0.04	-0.06 ± 0.03	-0.03 ± 0.03	-0.03 ± 0.03	0.02 ± 0.04
6562672	Turn-off	2.42 ± 0.05	-0.05 ± 0.12	-0.17 ± 0.03	-0.15 ± 0.03	-0.14 ± 0.03	-0.17 ± 0.03	-0.13 ± 0.04
6571851	Turn-off	2.34 ± 0.05	-0.06 ± 0.11	-0.09 ± 0.04	-0.12 ± 0.03	-0.12 ± 0.03	-0.06 ± 0.03	-0.08 ± 0.04
6568307	Turn-off	–	-0.05 ± 0.12	0.01 ± 0.04	0.00 ± 0.04	-0.08 ± 0.03	-0.04 ± 0.03	-0.02 ± 0.04
8436138	Turn-off	2.34 ± 0.05	-0.06 ± 0.12	-0.08 ± 0.03	-0.11 ± 0.03	-0.12 ± 0.04	-0.08 ± 0.03	-0.05 ± 0.04
6571594	Turn-off	2.13 ± 0.05	-0.01 ± 0.12	-0.02 ± 0.03	-0.01 ± 0.03	0.04 ± 0.03	-0.03 ± 0.02	-0.01 ± 0.04
6579199	Turn-off	2.21 ± 0.05	-0.02 ± 0.12	-0.10 ± 0.03	-0.06 ± 0.03	-0.02 ± 0.03	-0.06 ± 0.03	0.03 ± 0.05
6562188	Turn-off	–	0.12 ± 0.11	-0.07 ± 0.04	-0.05 ± 0.03	-0.16 ± 0.02	-0.11 ± 0.03	-0.05 ± 0.05
6567847	Turn-off	–	-0.01 ± 0.12	0.01 ± 0.03	-0.08 ± 0.03	-0.10 ± 0.05	-0.04 ± 0.02	-0.02 ± 0.04
6563234	Turn-off	–	-0.01 ± 0.12	0.05 ± 0.04	0.05 ± 0.04	-0.06 ± 0.04	-0.03 ± 0.03	0.00 ± 0.04
9077970	Subgiant	–	0.12 ± 0.13	0.02 ± 0.04	0.00 ± 0.03	-0.07 ± 0.02	0.03 ± 0.03	0.02 ± 0.04
6568921	Subgiant	–	0.05 ± 0.12	0.01 ± 0.04	0.02 ± 0.03	-0.01 ± 0.02	0.00 ± 0.03	-0.02 ± 0.04
6574583	Subgiant	–	-0.01 ± 0.13	0.08 ± 0.04	0.08 ± 0.03	0.10 ± 0.03	0.04 ± 0.03	0.07 ± 0.04
6562991	Subgiant	–	0.00 ± 0.13	-0.04 ± 0.04	0.01 ± 0.04	-0.04 ± 0.03	0.00 ± 0.03	-0.01 ± 0.04
6569862	Subgiant	–	0.01 ± 0.13	-0.04 ± 0.04	-0.05 ± 0.04	0.01 ± 0.03	0.03 ± 0.04	-0.02 ± 0.04
6567693	Subgiant	–	0.12 ± 0.13	-0.14 ± 0.04	-0.08 ± 0.04	-0.09 ± 0.03	-0.10 ± 0.04	-0.12 ± 0.04
6577630	Subgiant	–	-0.14 ± 0.13	-0.02 ± 0.05	-0.08 ± 0.04	-0.02 ± 0.02	-0.07 ± 0.04	-0.05 ± 0.04
6562765	Subgiant	–	-0.15 ± 0.13	-0.06 ± 0.05	-0.02 ± 0.04	-0.02 ± 0.03	-0.04 ± 0.04	-0.05 ± 0.04
6569012	Subgiant	–	-0.15 ± 0.14	0.06 ± 0.05	0.17 ± 0.04	0.10 ± 0.03	0.02 ± 0.05	0.07 ± 0.04
6571766	Red-giant	–	0.04 ± 0.14	-0.08 ± 0.04	0.01 ± 0.04	0.02 ± 0.02	-0.06 ± 0.05	-0.07 ± 0.05
6565104	Red-giant	–	-0.09 ± 0.14	-0.04 ± 0.04	0.00 ± 0.04	0.06 ± 0.03	0.01 ± 0.05	-0.03 ± 0.05
6579331	Red-giant	–	0.20 ± 0.14	-0.05 ± 0.06	-0.02 ± 0.04	0.02 ± 0.03	0.00 ± 0.04	-0.04 ± 0.04
6573364	Red-giant	–	-0.05 ± 0.14	-0.03 ± 0.05	-0.03 ± 0.04	-0.01 ± 0.03	-0.01 ± 0.04	-0.01 ± 0.05
6563655	Red-giant	–	-0.04 ± 0.15	0.02 ± 0.04	0.11 ± 0.04	0.18 ± 0.03	0.05 ± 0.05	0.03 ± 0.05
6570514	Red-giant	–	-0.08 ± 0.14	-0.05 ± 0.04	-0.11 ± 0.04	-0.02 ± 0.03	0.01 ± 0.05	-0.06 ± 0.04
6568851	Red-giant	–	0.00 ± 0.15	-0.09 ± 0.05	-0.12 ± 0.04	0.06 ± 0.03	-0.05 ± 0.05	-0.07 ± 0.05
6565879	Red-giant	–	0.07 ± 0.15	-0.09 ± 0.05	-0.15 ± 0.04	0.10 ± 0.03	-0.01 ± 0.05	-0.09 ± 0.04
6569711	Red-giant	–	0.00 ± 0.14	-0.05 ± 0.04	-0.19 ± 0.04	0.00 ± 0.04	-0.10 ± 0.05	-0.13 ± 0.05
6575356	Red-clump	–	-0.06 ± 0.14	0.04 ± 0.05	-0.12 ± 0.04	0.05 ± 0.03	-0.03 ± 0.05	-0.08 ± 0.05
6577481	Red-clump	–	-0.22 ± 0.15	0.05 ± 0.04	-0.09 ± 0.05	0.01 ± 0.03	-0.03 ± 0.05	-0.07 ± 0.05
6573728	Red-clump	–	-0.13 ± 0.15	0.05 ± 0.05	-0.08 ± 0.04	0.00 ± 0.04	-0.03 ± 0.04	-0.09 ± 0.05
6566179	Red-clump	–	0.12 ± 0.15	0.12 ± 0.05	-0.03 ± 0.05	0.06 ± 0.03	0.02 ± 0.05	-0.05 ± 0.05
6569393	Red-clump	–	0.07 ± 0.15	-0.07 ± 0.04	-0.14 ± 0.05	0.00 ± 0.03	-0.01 ± 0.05	-0.10 ± 0.05
6572270	Red-clump	–	0.00 ± 0.15	0.06 ± 0.05	-0.13 ± 0.04	0.03 ± 0.03	-0.01 ± 0.05	-0.08 ± 0.05

Table 2.5:: LTE chemical abundances of the sample stars in M67. Abundances were derived relative to non-LTE values of solar analysed in this work.

GALAH ID	Group	A(Li)$_{\text{LTE}}$	[O/H]$_{\text{LTE}}$	[Na/H]$_{\text{LTE}}$	[Mg/H]$_{\text{LTE}}$	[Al/H]$_{\text{LTE}}$	[Si/H]$_{\text{LTE}}$	[Fe/H]$_{\text{LTE}}$
6561552	Main-sequence	–	0.33 ± 0.10	0.07 ± 0.05	-0.03 ± 0.04	0.06 ± 0.02	0.00 ± 0.03	-0.02 ± 0.05
6560101	Turn-off	2.68 ± 0.05	0.32 ± 0.10	0.11 ± 0.04	-0.09 ± 0.03	-0.21 ± 0.02	-0.02 ± 0.03	-0.03 ± 0.04
6577714	Turn-off	2.66 ± 0.05	0.24 ± 0.10	0.07 ± 0.04	-0.14 ± 0.03	-0.02 ± 0.02	-0.04 ± 0.03	-0.05 ± 0.05
6554484	Turn-off	2.68 ± 0.05	0.22 ± 0.10	0.19 ± 0.04	-0.07 ± 0.03	-0.04 ± 0.02	-0.05 ± 0.03	0.05 ± 0.04
6577148	Turn-off	–	0.37 ± 0.10	0.16 ± 0.04	-0.13 ± 0.03	-0.14 ± 0.02	-0.04 ± 0.03	-0.03 ± 0.04
6569011	Turn-off	2.34 ± 0.05	0.37 ± 0.10	0.20 ± 0.04	-0.10 ± 0.03	-0.07 ± 0.02	-0.04 ± 0.03	0.00 ± 0.04
6565966	Turn-off	2.54 ± 0.05	0.22 ± 0.10	0.13 ± 0.04	-0.11 ± 0.03	-0.03 ± 0.03	-0.07 ± 0.03	-0.03 ± 0.04
6565326	Turn-off	2.42 ± 0.05	0.37 ± 0.10	0.23 ± 0.04	-0.10 ± 0.03	-0.02 ± 0.02	-0.02 ± 0.03	0.03 ± 0.04
6574584	Turn-off	–	0.29 ± 0.11	0.16 ± 0.04	-0.06 ± 0.03	-0.11 ± 0.02	-0.06 ± 0.03	0.00 ± 0.04
6571679	Turn-off	–	0.38 ± 0.10	0.19 ± 0.03	-0.10 ± 0.03	-0.17 ± 0.02	-0.06 ± 0.03	-0.04 ± 0.04
6567547	Turn-off	2.52 ± 0.05	0.26 ± 0.10	0.16 ± 0.04	-0.10 ± 0.03	-0.05 ± 0.02	0.00 ± 0.02	0.04 ± 0.04
6555602	Turn-off	–	0.32 ± 0.10	0.11 ± 0.04	-0.18 ± 0.03	-0.13 ± 0.02	-0.10 ± 0.03	-0.07 ± 0.04
6561039	Turn-off	2.70 ± 0.05	0.39 ± 0.10	0.07 ± 0.04	-0.06 ± 0.03	-0.11 ± 0.02	-0.02 ± 0.03	-0.05 ± 0.05
6570179	Turn-off	2.44 ± 0.05	0.28 ± 0.10	0.04 ± 0.04	-0.18 ± 0.03	-0.23 ± 0.03	-0.13 ± 0.03	-0.14 ± 0.04
6564123	Turn-off	2.38 ± 0.05	0.26 ± 0.10	0.11 ± 0.04	-0.05 ± 0.03	-0.11 ± 0.02	-0.06 ± 0.02	0.00 ± 0.05
6573044	Turn-off	2.45 ± 0.05	0.24 ± 0.10	0.13 ± 0.04	-0.12 ± 0.03	-0.13 ± 0.03	-0.04 ± 0.03	-0.03 ± 0.04
6575508	Turn-off	2.23 ± 0.05	0.29 ± 0.10	0.03 ± 0.04	-0.16 ± 0.03	-0.21 ± 0.02	-0.08 ± 0.03	-0.11 ± 0.05
6558150	Turn-off	2.52 ± 0.05	0.30 ± 0.10	0.17 ± 0.04	-0.15 ± 0.03	-0.14 ± 0.02	-0.07 ± 0.03	-0.06 ± 0.05
6568768	Turn-off	–	0.39 ± 0.10	0.14 ± 0.04	-0.07 ± 0.03	-0.09 ± 0.03	-0.08 ± 0.03	-0.04 ± 0.04
6573727	Turn-off	2.47 ± 0.05	0.18 ± 0.10	0.05 ± 0.04	-0.17 ± 0.03	-0.08 ± 0.02	-0.06 ± 0.03	-0.07 ± 0.04
6573191	Turn-off	–	0.35 ± 0.10	0.18 ± 0.04	-0.14 ± 0.04	-0.10 ± 0.02	-0.09 ± 0.02	-0.05 ± 0.05
6572337	Turn-off	2.35 ± 0.05	0.21 ± 0.11	0.16 ± 0.04	-0.10 ± 0.03	0.06 ± 0.03	-0.04 ± 0.03	-0.01 ± 0.04
6569861	Turn-off	2.26 ± 0.05	0.24 ± 0.10	0.06 ± 0.04	-0.15 ± 0.03	-0.21 ± 0.02	-0.09 ± 0.02	-0.05 ± 0.04
6564445	Turn-off	2.22 ± 0.05	0.13 ± 0.10	0.19 ± 0.04	-0.03 ± 0.03	-0.16 ± 0.03	-0.02 ± 0.02	-0.05 ± 0.04
6567617	Turn-off	2.68 ± 0.05	0.27 ± 0.11	0.14 ± 0.04	-0.10 ± 0.03	-0.04 ± 0.03	-0.02 ± 0.03	-0.06 ± 0.05
6559497	Turn-off	2.58 ± 0.05	0.24 ± 0.10	0.20 ± 0.04	-0.08 ± 0.03	-0.08 ± 0.02	0.00 ± 0.03	0.01 ± 0.05
6568479	Turn-off	1.71 ± 0.05	0.17 ± 0.11	0.07 ± 0.04	-0.12 ± 0.03	-0.10 ± 0.03	-0.07 ± 0.03	-0.07 ± 0.04
6572560	Turn-off	2.50 ± 0.05	0.36 ± 0.11	0.23 ± 0.04	-0.07 ± 0.03	-0.08 ± 0.03	-0.04 ± 0.03	0.00 ± 0.04
6572187	Turn-off	2.05 ± 0.05	0.30 ± 0.10	0.18 ± 0.04	-0.07 ± 0.03	-0.05 ± 0.03	-0.02 ± 0.03	0.01 ± 0.05
6560653	Turn-off	2.43 ± 0.05	0.13 ± 0.10	0.09 ± 0.04	-0.14 ± 0.03	-0.04 ± 0.02	-0.09 ± 0.03	-0.05 ± 0.05
6567233	Turn-off	2.65 ± 0.05	0.28 ± 0.10	0.19 ± 0.05	-0.04 ± 0.03	-0.05 ± 0.02	-0.02 ± 0.03	0.00 ± 0.04
6569167	Turn-off	2.45 ± 0.05	0.28 ± 0.11	0.12 ± 0.04	-0.08 ± 0.03	-0.14 ± 0.03	-0.02 ± 0.03	0.00 ± 0.04
6565967	Turn-off	2.62 ± 0.05	0.28 ± 0.11	0.20 ± 0.04	-0.08 ± 0.03	-0.01 ± 0.02	-0.02 ± 0.02	0.03 ± 0.04
6562672	Turn-off	2.42 ± 0.05	0.20 ± 0.10	-0.01 ± 0.04	-0.17 ± 0.03	-0.13 ± 0.03	-0.16 ± 0.02	-0.12 ± 0.05
6571851	Turn-off	2.34 ± 0.05	0.17 ± 0.10	0.08 ± 0.04	-0.14 ± 0.03	-0.11 ± 0.02	-0.04 ± 0.03	-0.06 ± 0.05
6568307	Turn-off	–	0.32 ± 0.11	0.21 ± 0.04	-0.06 ± 0.03	-0.07 ± 0.02	-0.03 ± 0.03	0.01 ± 0.04
8436138	Turn-off	2.34 ± 0.05	0.18 ± 0.10	0.10 ± 0.04	-0.12 ± 0.04	-0.10 ± 0.03	-0.06 ± 0.02	-0.04 ± 0.05
6571594	Turn-off	2.12 ± 0.05	0.37 ± 0.10	0.18 ± 0.04	-0.05 ± 0.03	0.06 ± 0.02	-0.01 ± 0.02	0.02 ± 0.05
6579199	Turn-off	2.21 ± 0.05	0.23 ± 0.10	0.06 ± 0.04	-0.09 ± 0.03	0.00 ± 0.03	-0.05 ± 0.03	0.04 ± 0.04
6562188	Turn-off	–	0.40 ± 0.10	0.10 ± 0.04	-0.07 ± 0.03	-0.14 ± 0.02	-0.09 ± 0.02	-0.04 ± 0.05
6567847	Turn-off	–	0.35 ± 0.11	0.20 ± 0.04	-0.12 ± 0.04	-0.07 ± 0.04	-0.03 ± 0.03	0.00 ± 0.04
6563234	Turn-off	–	0.35 ± 0.11	0.26 ± 0.04	0.00 ± 0.03	-0.04 ± 0.03	-0.01 ± 0.03	0.03 ± 0.04
9077970	Subgiant	–	0.36 ± 0.12	0.21 ± 0.04	-0.02 ± 0.03	-0.02 ± 0.02	0.05 ± 0.03	0.05 ± 0.04
6568921	Subgiant	–	0.29 ± 0.12	0.20 ± 0.04	0.00 ± 0.03	0.03 ± 0.02	0.01 ± 0.03	0.01 ± 0.05
6574583	Subgiant	–	0.17 ± 0.12	0.25 ± 0.05	0.07 ± 0.03	0.15 ± 0.03	0.06 ± 0.03	0.11 ± 0.05
6562991	Subgiant	–	0.17 ± 0.12	0.13 ± 0.05	0.00 ± 0.04	0.01 ± 0.03	0.02 ± 0.03	0.02 ± 0.05
6569862	Subgiant	–	0.16 ± 0.13	0.13 ± 0.05	-0.05 ± 0.03	0.06 ± 0.02	0.05 ± 0.03	0.01 ± 0.05
6567693	Subgiant	–	0.29 ± 0.12	0.03 ± 0.05	-0.07 ± 0.03	-0.03 ± 0.03	-0.09 ± 0.04	-0.09 ± 0.05
6577630	Subgiant	–	-0.02 ± 0.13	0.14 ± 0.05	-0.07 ± 0.03	0.04 ± 0.03	-0.06 ± 0.04	-0.02 ± 0.05
6562765	Subgiant	–	-0.03 ± 0.13	0.10 ± 0.05	-0.01 ± 0.03	0.05 ± 0.03	-0.02 ± 0.04	-0.02 ± 0.04
6569012	Subgiant	–	-0.03 ± 0.13	0.24 ± 0.05	0.18 ± 0.03	0.16 ± 0.03	0.04 ± 0.04	0.10 ± 0.05
6571766	Red-giant	–	0.17 ± 0.13	0.08 ± 0.07	0.03 ± 0.04	0.09 ± 0.03	-0.04 ± 0.04	-0.03 ± 0.05
6565104	Red-giant	–	0.04 ± 0.13	0.14 ± 0.06	0.02 ± 0.04	0.14 ± 0.03	0.03 ± 0.05	0.04 ± 0.05
6579331	Red-giant	–	0.37 ± 0.13	0.14 ± 0.06	0.00 ± 0.04	0.10 ± 0.03	0.02 ± 0.05	0.01 ± 0.05
6573364	Red-giant	–	0.09 ± 0.13	0.18 ± 0.06	-0.02 ± 0.04	0.07 ± 0.03	0.01 ± 0.04	0.05 ± 0.06
6563655	Red-giant	–	0.10 ± 0.14	0.23 ± 0.05	0.12 ± 0.04	0.27 ± 0.03	0.07 ± 0.04	0.09 ± 0.05
6570514	Red-giant	–	0.05 ± 0.14	0.15 ± 0.05	-0.09 ± 0.04	0.05 ± 0.04	0.04 ± 0.04	-0.01 ± 0.05
6568851	Red-giant	–	0.15 ± 0.14	0.13 ± 0.06	-0.11 ± 0.04	0.15 ± 0.03	-0.02 ± 0.05	-0.02 ± 0.05
6565879	Red-giant	–	0.21 ± 0.14	0.15 ± 0.06	-0.13 ± 0.04	0.19 ± 0.03	0.01 ± 0.05	-0.02 ± 0.04
6569711	Red-giant	–	0.14 ± 0.14	0.18 ± 0.06	-0.17 ± 0.04	0.10 ± 0.04	-0.07 ± 0.05	-0.06 ± 0.05
6575356	Red-clump	–	0.13 ± 0.15	0.28 ± 0.05	-0.12 ± 0.04	0.15 ± 0.03	0.01 ± 0.05	0.00 ± 0.05
6577481	Red-clump	–	-0.07 ± 0.15	0.29 ± 0.05	-0.10 ± 0.04	0.12 ± 0.03	0.01 ± 0.04	0.01 ± 0.05
6573728	Red-clump	–	0.05 ± 0.14	0.28 ± 0.05	-0.07 ± 0.03	0.10 ± 0.03	0.00 ± 0.05	-0.01 ± 0.05
6566179	Red-clump	–	0.29 ± 0.14	0.34 ± 0.05	-0.03 ± 0.04	0.18 ± 0.03	0.05 ± 0.05	0.04 ± 0.05
6569393	Red-clump	–	0.25 ± 0.15	0.16 ± 0.05	-0.13 ± 0.04	0.10 ± 0.03	0.03 ± 0.05	-0.04 ± 0.05
6572270	Red-clump	–	0.16 ± 0.15	0.28 ± 0.05	-0.12 ± 0.04	0.15 ± 0.04	0.03 ± 0.05	0.00 ± 0.05

Chapter 3

Stellar lithium depletion from the Spite plateau to the dip and beyond

The following chapter contains a modified version of an article that will be submitted to Nature Astronomy. Gao et al. in prep.

3.1 Introduction

Lithium (Li) in late-type stellar atmospheres has been well studied both theoretically and observationally, because the unique properties of this light element make it important for many fields in astrophysics. However, there are still some unsolved problems to be addressed.

3.1.1 Cosmological Lithium Problem

Most famously, Li can be regarded as an important cosmological indicator, since it can be produced in the early Universe. Over the past decade, WMAP measurements of the cosmic microwave background (CMB) radiation have allowed a precise determination of the cosmic ratio of baryons to photons (Hinshaw et al. 2013), a quantity directly related to the fractions of the light elements produced by Big Bang nucleosynthesis (BBN) (Burles et al. 2001). The primordial abundances of light elements for ^{4}He (Aver et al. 2015), ^{3}He (Bania et al. 2002) and D (Cooke et al. 2018) inferred from the observation data have a good agreement with the predictions from standard BBN. However, the primordial ^{7}Li abundance deduced

from unevolved metal-poor stars in the Galaxy (that fall on the so-called "Spite plateau", at A(Li) [1] $\approx$ 2.2; see Spite & Spite 1982; Spite et al. 2015) show three times lower than the predicted value (A(Li) = 2.75 ± 0.02; see Pitrou et al. 2018), leading to the Cosmological Lithium Problem. This long-recognized discrepancy has also led to suggestions of non-standard cosmological physics Holder et al. (2010) or decaying exotic particles in the early Universe Bailly et al. (2009); Pospelov & Pradler (2010).

3.1.2   Galactic Lithium Enrichment

Furthermore, the Li abundances found in meteoritic (A(Li) = 3.26 Lodders et al. 2009) and young clusters (e.g. Sestito & Randich 2005) can be used to investigate the Li enrichment of the Galaxy. Except for Big Bang production, there are many mechanisms of Li production have been proposed (Cosmic ray spallation by Reeves et al. 1970; novae by Arnould & Norgaard 1975; core collapse supernovae by Arnould & Norgaard 1975; AGB stars by Sackmann & Boothroyd 1992; RGB stars by Sackmann & Boothroyd 1999). However, it is very difficult to constrain the contribution of each source based on current limited observations, especially for the stellar production sources. Moreover, according to current Galactic chemical evolution (GCE) models, not enough Li is yielded from all those sources to match the observations (Prantzos 2012).

3.1.3   Lithium Dip in Main-sequence stars

On the other hand, Li is a fragile element that can be easily destroyed by proton capture reactions at relatively low temperatures ($\sim 2.5 \times 10^6$ K) in stellar interiors Pinsonneault (1997). It thus can also be regard as a tracer for particle transport in stars to constrain stellar evolution models. From the observational side, Li abundances derived from Population I stars show a significant drop in the main-sequence stars in which effective temperature located in a narrow range of 300 K centered around 6700 K. Within this narrow temperature range, the depletion in Li can reach a factor of 100 relative to stars out of this region. This striking feature called the "lithium dip" (Li dip), was first observed in the open cluster Hyades by Wallerstein et al. (1965) and later confirmed by Boesgaard & Tripicco (1986). Since the first observations, the presence of the Li dip has also been found in the older clusters NGC 752 and M67 (Balachandran 1995), but not in the youngest open

---

[1]A(Li) = $\log \frac{n_{\text{Li}}}{n_{\text{H}}} + 12$, where n_{Li} and n_{H} are the the number densities of lithium and hydrogen, respectively.

clusters (Boesgaard et al. 1988; Balachandran et al. 2011) – those with ages less than about 100 Myr. This is a strong evidence that these large Li reductions took place while the stars are on the main-sequence, rather than during the pre-main-sequence phase.

On the warm side of the dip, the Li abundances increase sharply with effective temperature. For T_{eff} larger than ~ 6900 K, the Li abundances seem to remain constant, compatible with the Galactic value (i.e., the meteoritic value) for the main-sequence cluster stars (Michaud & Charbonneau 1991; Boesgaard et al. 2016). However, few abundance determinations are available for stars in this "quiet zone" (see the definition in Fig. 3.1), since the lithium line is too weak and broad to be determined in most of these hot stars due to fast rotation. On the cool side of the dip, the Li abundances increase gradually with decreasing effective temperature until reaching a sort of plateau, which extends from ~ 6400 to ~ 6000 K. Stars in this "inactive zone" seem to experience a slightly uniform Li depletion but not drastically as dip stars (in the "active zone").

In addition, the lithium dip has been observed among the field stars as well (e.g. Randich et al. 1999; Lambert & Reddy 2004; Bensby & Lind 2018). Thus, to study the behaviour of Li in field stars as a function of stellar parameters can also provide valuable information about Li depletion. A large gap named the "Li desert" in the A(Li)-T_{eff} plane has been confirmed by analysing the late-type field stars (e.g. Lambert et al. 1991; Chen et al. 2001; Ramírez et al. 2012; Aguilera-Gómez et al. 2018). Stars show a bimodal distribution in Li abundances between 5900 K and 6600 K. The group with high-Li shows an increasing trend of Li with T_{eff} and [Fe/H]; while the low-Li group is thought to be post-main-sequence stars that have evolved from the Li dip, since a tight correlation between mass and metallicity for these stars has been found. However, in order to obtain large sample, most of the studies collected other literature measurements into a compilation, which may enlarge the systematic errors in the stellar parameters and abundances analysis. The feature of Li desert could be also due to the observational bias. Therefore, to have a better understanding of the Li evolution, a large sample of stars with homogeneous measurements is needed.

3.1.4   Theoretical Studies for Lithium Dip

Li depletion occurred on the main-sequence stage contradicts the predictions by standard stellar evolution models, which conclude that Li should not be destroyed on the surface of late-type stars because of their shallow surface convection zones (e.g. Deliyannis et al. 1990; Pinsonneault 1997). In order to meet observational

constraints such as the complicated Li abundance pattern in the clusters and field stars, several physical processes describing Li depletion have been proposed.

Michaud (1986) proposed microscopic diffusion as an explanation for the Li dip. Stars with T_{eff} >6900 K, the upward radiative acceleration dominates over gravitational settling, leading to sustain the lithium abundances on the surface. In the temperature range of the dip, lithium would settle below the convetive zone and be underabundances due to the dominant gravitational settling. In stars cooler than 6400 K, the rise of the Li abundance on the cool side of the dip can be explained by the increase of the convective envelope, which leads to longer diffusion timescales and thus to slower surface lithium depletion. By adjusting two free parameters, the mixng length (control the effective temperature of the dip) and mass loss rate (reduce the Li overabundances on the warm side of the dip), they reproduced the general feature of the Li dip. However, several observation facts contradict with the pure microscopic diffusion hypothesis: for example, in this scenario, Li is not destroyed but settled just below the convective zone. As a result, Li should be dredged up to the surface as the star evolves off the main-sequence. This Li dredge-up is not observed in open cluster stars (Deliyannis et al. 1997; Balachandran 1995).

Boesgaard (1987) discovered that there is a drastically drop in projected rotation velocity at the Li dip region of Hyades cluster. Thus, rotation-induced mixing was been investigated by many theoretical works and suggested to play an important role on the dip stars. Talon & Charbonnel (1998) considered meridional circulation and shear turbulence in the transport of angular momentum. The transport of chemicals was computed due to the rotation-induced mixing as described by (Zahn 1992). In this framework, they well reproduced the warm side of the Li dip, while the cool side of the dip whose characteristic is a more gradual rise fails to be explained by their model. Based on their model, the deeper convective envelope on the cool side of the Li dip will produce a strong magnetic torque to spin down the outer layer more efficiently, resulting in too much Li depletion due to the enhanced mixing. Since their model also fails to reproduce the flat rotation profile in the Sun, they suspected that Li dip should be a transition region where another unknown process start to participate in the transport of angular momentum on the cool side.

Garcia Lopez & Spruit (1991) then suggested that internal gravity waves (IGWs) that generated by the convective envelope of a star could effectively produce a weak mixing in the radiative interior. Talon & Charbonnel (2005) developed a model that incorporate not only atomic diffusion and rotational mixing, but also the contribution of IGWs to the transport of angular momentum and chemical elements. They found that the generation of IGWs and its efficiency in extracting angular momentum from stellar interior strongly depend on the effective temperature. On

the warm side of Li dip, no IGWs can be generated, while on the cool side of the dip, IGWs are activated and efficiently extract angular momentum from the core to reduce the rotation-induced mixing, leading to the rise of the surface Li. Their model has successfully reproduced the morphology of the Li dip in the Hyades, both regarding the amplitude of the Li depletion and the dispersion at a given effective temperature.

3.1.5 Motivations in this work

Earlier studies of lithium in unevolved field stars have typical sample sizes of 200-2000 stars in total Lambert & Reddy (2004); Ramírez et al. (2012); Bensby & Lind (2018); Aguilera-Gómez et al. (2018), which covered only a small range in stellar properties and contained very few stars on the warm side of the lithium dip. The observational landscape has drastically changed in the last few years. The GALAH surveyDe Silva et al. (2015), has amassed a sizable number of spectroscopic observation of field stars in the solar neighbourhood, enabling us to study the Li evolution comprehensively.

The aim of the present study is to investigate the behaviour of Li among late-type stars including main-sequence, turn-off and early subgiant, based on the largest sample so far covering a wide range of metallicities and ages with a homogeneous Li determination from GALAH survey. We will mainly focus on the study of stars that locate on both sides of the Li dip, i.e., stars in the quiet and inactive zones. Stars in the quiet zone has the least Li-depletion, which can be used as best indicators of Galactic Li enrichment. Stars in the inactive zone correspond to Spite plateau stars at low metallicity. It is of great importance for cosmology and BBN to understand how much Li was depleted by these stars.

3.2 Observations and Analysis

Our baseline sample is around $650\,000$ FGK field stars in the solar neighbourhood observed by the large scale spectroscopic GALAH survey (De Silva et al. 2015). The spectral resolving power of the surveys $R = \frac{\lambda}{\Delta\lambda} \approx 28\,000$ is sufficiently matched to the stellar absorption lines under study. The observational data is taken from GALAH iDR3 (Buder et al. in prep.).

We first filter the dataset according to the quality control flags described by Buder et al. (in prep.). In brief, GALAH applies the dimensionality reduction method
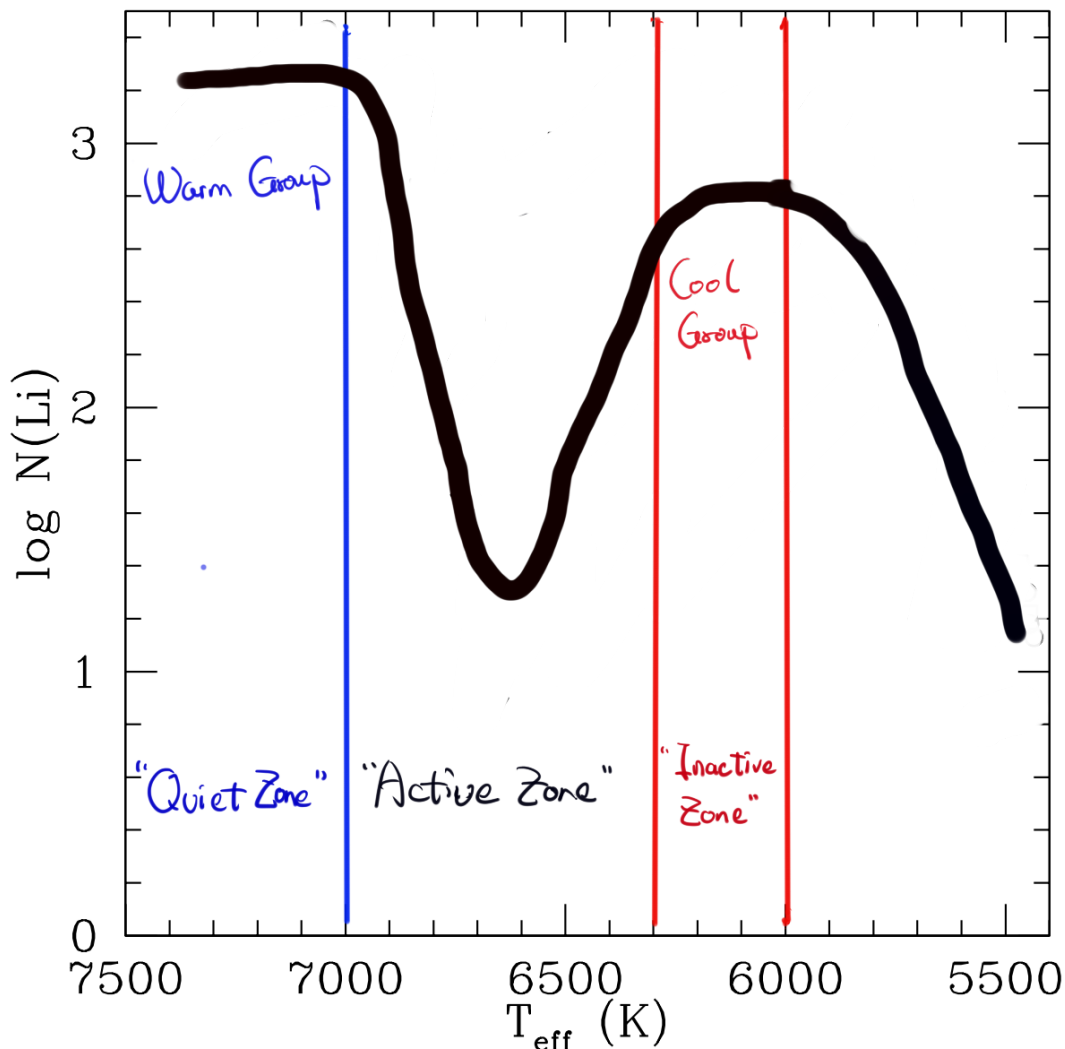
Figure 3.1: **Schematic plot of Li dip in main-sequence stars.** The general feature of the Li dip is drawn based on the observations of Hyades. Here We name three different effective temperature regions as "Quiet zone", "Active zone" and "Inactive zone" based on the theory of Talon & Charbonnel (2005). In this thesis, the warm side of the Li dip usually refers to the stars located in the quiet zone; the cool side of the Li dip refers to the stars in the inactive zone. In quiet zone: stars have shallow convective zone and not slowed down efficiently. The rotational-induced mixing counteract the effect of atomic diffusion. In active zone: on the left side of the zone, rotational-induced mixing dominant the transport of angular momentum, resulting in a Li depletion by enhanced mixing; on the right side of the zone, IGWs start to be generated by the surface convection zone to counteract the angular momentum by rotational mixing. In inactive zone: IGWs are fully activated and dominant the angular momentum transport.

t-SNE (Maaten & Hinton 2008) to help separate distinct groups of spectra with different spectral features. All groups of spectra then have been assigned different flag indices for which a reasonable physical category can be sorted out. With the help of GALAH flag information, we can identify those targets for which good quality spectra are available, whilst excluding spectroscopically resolved binaries, and observations with fitting inaccuracies, low S/N ratio, strong emission lines or reduction issues, etc. (see Buder et al. 2018). For this work, since our primary goal is to investigate the Li evolution among the late-type stars, we mainly target the dwarf and subgiant stars with a $T_{\rm eff}$ ranging from 5900 to 7200 K and covering a large range of metallicity from [Fe/H] = +0.5 to [Fe/H] = −3.0, which includes the Spite plateau at the metal-poor end. After all these selections, we finally obtained a set of 65 431 stars with Li detections and a set of 47 033 stars with upper limit for Li.

The stellar parameters $T_{\rm eff}$, [Fe/H], as well as projected rotational velocities $v \sin \iota$, and line-of-sight radial velocity RV, in our sample were determined simultaneously in a homogeneous way by fitting the observed neutral and ionized lines of Sc, Ti, Fe that were unblended and that had reliable atomic data, as well as the $T_{\rm eff}$-sensitive H and H lines, using the GALAH analysis pipeline (for more details see Chapter 2 and Buder et al. 2018). Surface gravities ($\log g$) were constrained consistently and simultaneously by the fundamental relation between the absolute magnitude (obtained from the Gaia-measured parallax (e.g. Lindegren et al. 2018)), mass and effective temperature (e.g. Buder et al. 2019). Stellar masses and ages were estimated by a Bayesian implementation of isochrone fitting (Lin et al. 2018).

Having obtained the optimal stellar parameters, Li abundances were then derived by spectral synthesis fitting in the context of departures from LTE in the formation of resonance Li I 670.8 nm doublet. The non-LTE departure coefficients come from the model described in Lind et al. (2009a). We consider Li to be detected when the line depression ($i.e.$, $D \equiv 1 - \frac{F_\lambda}{F_c}$) is deeper than 2σ of the flux error within line mask, and at least 5% below the normalised continuum flux. In all other cases, the measurement is considered as an upper limit. To determine the Li upper limits of those measurements, since the line is not strong enough, we estimate an upper limit from an artificial line strength assumption and empirical A(Li) values that are estimated from a fitted correlation of line depression and $T_{\rm eff}$ for our given sample and observation setup. For this, we first assume the line strength to be two the flux error and 5% of the normalised flux and then use the empirically estimated correlation, as follows:

$$A(\mathrm{Li}) = 1.20 \times \log_{10}(\mathrm{D}) + 4.90 \times (\mathrm{T_{eff}}/5900(\mathrm{K})) - 1.25 \qquad (3.1)$$

Note that this relation is only applicable to GALAH resolution spectra within a narrow range of temperature ($5900\,\mathrm{K} \le T_{\rm eff} \le 7200\,\mathrm{K}$) and line depression less than

0.32. For stars with $v \sin \imath$ larger than 20 km s^{-1}, a 0.04 dex offset needs to be added into Equation 3.1 due to the large effect of rotational broadening.

3.3 Results

The right and left panels of Fig. 3.2 show the locations of stars with Li upper limits and detections in the HR diagram, respectively. Comparing the two panels, a clear gap can be seen among the distribution of stars for which Li could be detected (Fig. 3.2.b). However, this is not seen in the corresponding distribution of stars for which only upper limits on the lithium abundance could be obtained (Fig. 3.2.a). Most of the stars with Li upper limits are concentrated in a region, along a tilted line from $T_{\rm eff} \sim 6300$ to 6600 K, with surface gravity $\log g$ approximately ranging from 3.8 to 4.3 dex. we interpret this as the "lithium dip" region: the concentrated region of Li upper limits on the density plots marks the evolutionary track of Li dip stars, i.e., covering the main-sequence stars that are experiencing sever Li depletion and those stars evolve to the turn-offs and subgiants. We delineate groups of stars that are cooler and warmer than the lithium dip (as marked; see Fig. 3.2) for comparison and interpretation.

Therefore, we try to characterise the Li dip region based on the morphological features of Li upper limits in the HR diagram. In the right panel of Fig. 3.2, we first narrow down the $\log g$ range of our sample $(3.7 - 4.4 \, {\rm dex})$ to reduce the evolutionary effects on Li. Our sample now consists of upper main-sequence stars, turn-off stars and early subgiants. Note that once a star evolves off the main-sequence, its convective envelope will increase in depth and bring up Li-depleted material from the interior to dilute the surface abundance. However, this process is expected to be happening gradually. Before the onset of the first dredge up, on the early subgiant branch a significant decrease in Li is not expected to be observed, which has been confirmed by the open cluster (e.g. Balachandran 1995) and globular cluster observations (e.g. Lind et al. 2009b). Therefore, Li abundance differences and dispersion in subgiants are mostly established during the main-sequence. The severe Li depletion exhibited by subgiants immediately past the main-sequence turn-off reflect that stars have undergone extensive depletion on the main-sequence and have evolved from the Li dip.

Moreover, we remove all the stars with $T_{\rm eff}$ less than 6000 K, as the cooler stars undergo strong and rapid Li depletion, due to the larger convective envelopes (e.g. Bensby & Lind 2018). We then plot the density contours on the distribution of probability density estimation of Li upper limits by applying Gaussian kernel

density estimation (KDE). Finally, we define the boundaries of the Li dip region by using linear fits in the left and right edges of the outermost (lowest density) contour. Considering the systematic uncertainties in effective temperature, we further relax the estimated gradient of each boundary to 1σ standard error. The central area that is characterised by all the pink lines is defined as Li-dip star region; stars to the left and right boundaries of dip region are classified as warm and cool group stars, respectively. Stars that lie outside these three regions are removed from the final sample. The region selection based on the upper limits is also applied to the Li detection stars.

Stars on left side of the dip region mostly belong to the quite zone, where Li is barely depleted and remain normal at the surface due to interaction between weak mixing and microscopic diffusion. Stars on right side of the dip region mostly come from the inactive zone, where Li is stably depleted because of stabilising IGWs dominant the transport of angular momentum. Additionally, the most recent observations of the Hyades cluster (Boesgaard et al. 2016) and model predictions (Charbonnel & Talon 2005b) all agree that the warm side of the dip is somewhat more enhanced in Li than the cool side. For the first time we can now attempt to quantify this abundance difference with a large field sample.

To reduce the effects of possible pollution of the warm and cool regions by stars from the Li dip region, we henceforth restrict our sample to stars with confirmed Li detections in either group. The left panel of Fig. 3.3 shows detected Li measurements as a function of [Fe/H] in the warm and cool groups. Black squares and asterisks separately represent the average Li abundances of corresponding metallicity bin in hot and cool groups, respectively. The corresponding location of warm and cool group targets are shown in the red and blue boxes on the right panel of Fig. 3.3. Stars in the cool group with low metallicity ([Fe/H] ≤ -1 dex) have ages in excess of 11 Gyr and reveal the Spite Plateau (Spite & Spite 1982), showing low and near-constant Li abundances. In contrast, the warm group stars with higher masses have evolved off the main-sequence after such a long period. Most of the warm group stars begin to show up with [Fe/H] $\gtrsim -1.0$. Up to $-1.0 \lesssim$ [Fe/H] $\lesssim -0.5$, the warm group shows a similar constant lithium plateau, but elevated by almost three times that of the cool group (0.45 dex). Remarkably, the warm group plateau in this metallicity regime is fully consistent with the predictions of SBBN. This suggests that both Galactic enrichment and stellar destruction have been insignificant in this population of stars. At higher metallicities $-0.5 \lesssim$ [Fe/H] $\lesssim +0.3$, the difference in average Li abundances between the warm and cool groups still keeps a constant value of around 0.45 dex, with both the warm and cool groups showing a steady increasing trend due to Galactic enrichment (Prantzos et al. 2017). From the observational
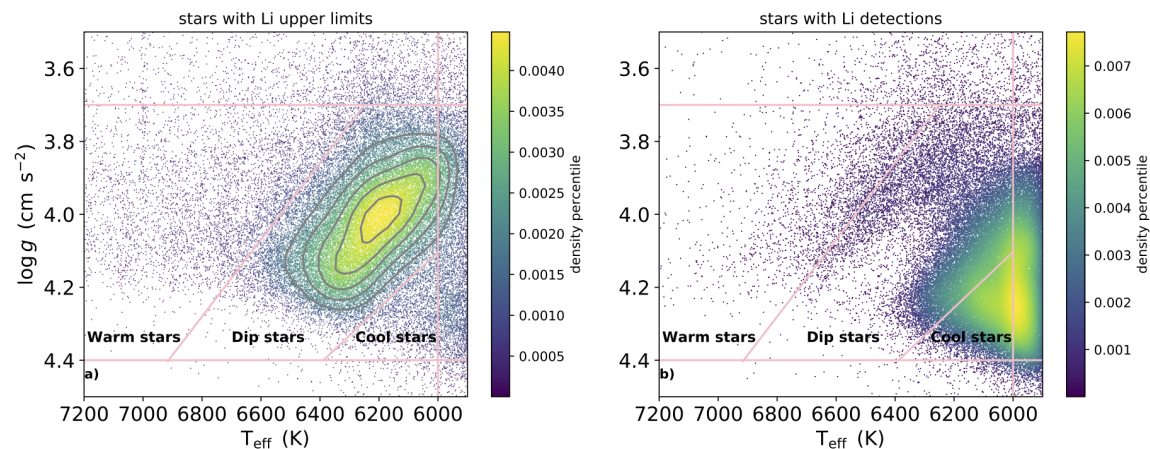
Figure 3.2: **Loci of the sample stars with lithium upper limits and lithium detections in the T_{eff}-$\log g$ panel, respectively.** *Left panel*: Loci of stars with lithium upper limits. The colour bar represents density distribution of stars, with bright colours implying high density. To characterise the lithium dip region, we first narrow down the $\log g$ range of our sample $(3.7 - 4.4 \, \text{dex})$. Moreover, we remove all the stars with T_{eff} less than $6000 \, \text{K}$, as those stars undergo strong and rapid lithium depletion, due to their larger convective envelopes. Then the contours are overplotted based on the density percentile of lithium upper limit stars. Finally, we define the boundaries of the lithium dip region by using linear fits in the left and right edges of the outermost contour with a density percentile of 0.002. Considering the systematic uncertainties in effective temperature, we further relax the estimated gradient of each boundary to 1σ standard error. The central box that is characterised by the pink lines is defined as the lithium-dip star region; stars to the left and right boundaries of the lithium-dip region are classified as warm and cool group stars, respectively. Stars that lie outside these three regions are removed from the final sample. *Right panel*: Loci of stars with lithium detections. The region selection based on the upper limits is also applied to the lithium detection stars.

side, we thus find that stars that fall in the warm group region of the main-sequence retain more of their initial Li than stars in the cool group. The Li abundance difference is typically 0.45 ± 0.02 dex, independent of metallicity.

For $0.3 \lesssim$ [Fe/H] $\lesssim 0.5$, average Li abundances seem to flatten and even start to decrease in cool group stars. Delgado Mena et al. (2015) also found a similar behaviour in average Li abundances from the upper envelope in their sample for metallicity higher than solar. They suspected that the flattening observed at high [Fe/H] may be caused by a balance between a higher initial Li produced by Galactic Li enrichment, and a stronger depletion of Li as a result of deepening of stellar convective zone. However, due to the lack of enough warm group stars in this high metallicity regime, the average Li abundance with a relative high standard error appears to overturn and significantly decrease. Considering that the uncertainties in this regime are very large, we decide not to take into account these stars when comparing the differences between two groups.

The colour gradient of the lithium abundances (Fig. 2b) reveals differences between the three groups. Because most of our sample are centered around the solar metallicity, we overplotted the evolutionary tracks of three different masses in solar metallicity on the distribution of our targets, which match the corresponding warm, dip and cool star regions quite well. Especially for the lithium-dip region, the theoretical models support our speculation that we have captured the evolutionary track of lithium-dip stars in our observations.

3.4   Discussion

3.4.1   Galactic enrichment

Fig. 3.4 shows that there is a difference in mean ages between the warm group (young) and cool group (old) stars, because of the sample selection method. The age difference is largest at low metallicity (up to 7 Gyr) and steadily decreases to become insignificant at the highest metallicities. The age difference may lead one to speculate that Galactic chemical evolution has elevated the initial lithium abundances in the warm group compared to the cool. However, the Galactic enrichment is more metallicity-dependent (the enriched medium where the stars were born) rather than age-dependent, otherwise, the offset between the two groups at a given metallicity would be very far from constant. Our data imply that such enrichment scales with increasing metallicity and only becomes noticeable at higher metallicity where [Fe/H] > -0.5.
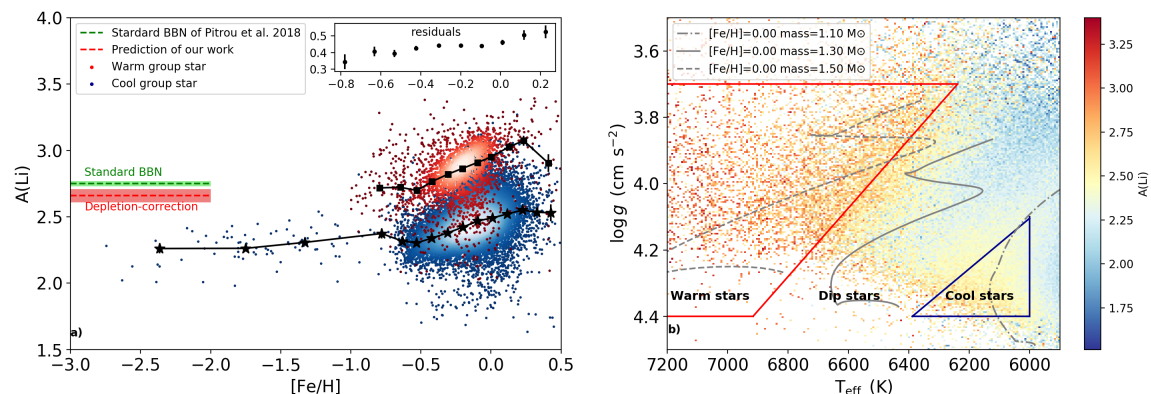
Figure 3.3: **Li trends as a function of metallicity between the observed warm group and cool group stars.** *Left panel*: Observational data of Li from the warm and cool groups as a function of [Fe/H]. Only detections are retained in each group and plotted as colour-coded density. Black squares and asterisks separately represent the average Li abundances of the corresponding metallicity bins in the warm and cool groups, respectively. The error bars represent the uncertainties of the mean, most of them are too small to be shown. The residual of the mean Li abundances between the warm and cool groups in the corresponding metallicity range is shown as an inset in the upper right corner. The average difference is 0.45 ± 0.02 (depletion-correction). The primordial Li abundances from the standard BBN (Pitrou et al. 2018) and our prediction by applying the depletion-correction onto the mean abundances of metal poor stars are shown as green and red dashed lines, respectively. The corresponding shaded areas represent the standard error of the mean. *Right panel*: All the stars with Li detections and upper limits are colour-coded by the A(Li) in the T_{eff}-$\log g$ panel. The corresponding location of warm and cool group targets are shown in the red and blue boxes, respectively. The colour gradient of Li abundance clearly shows the Li differences between the three regions. Evolutionary tracks of different masses in the solar metallicity are overplotted in the corresponding regions.
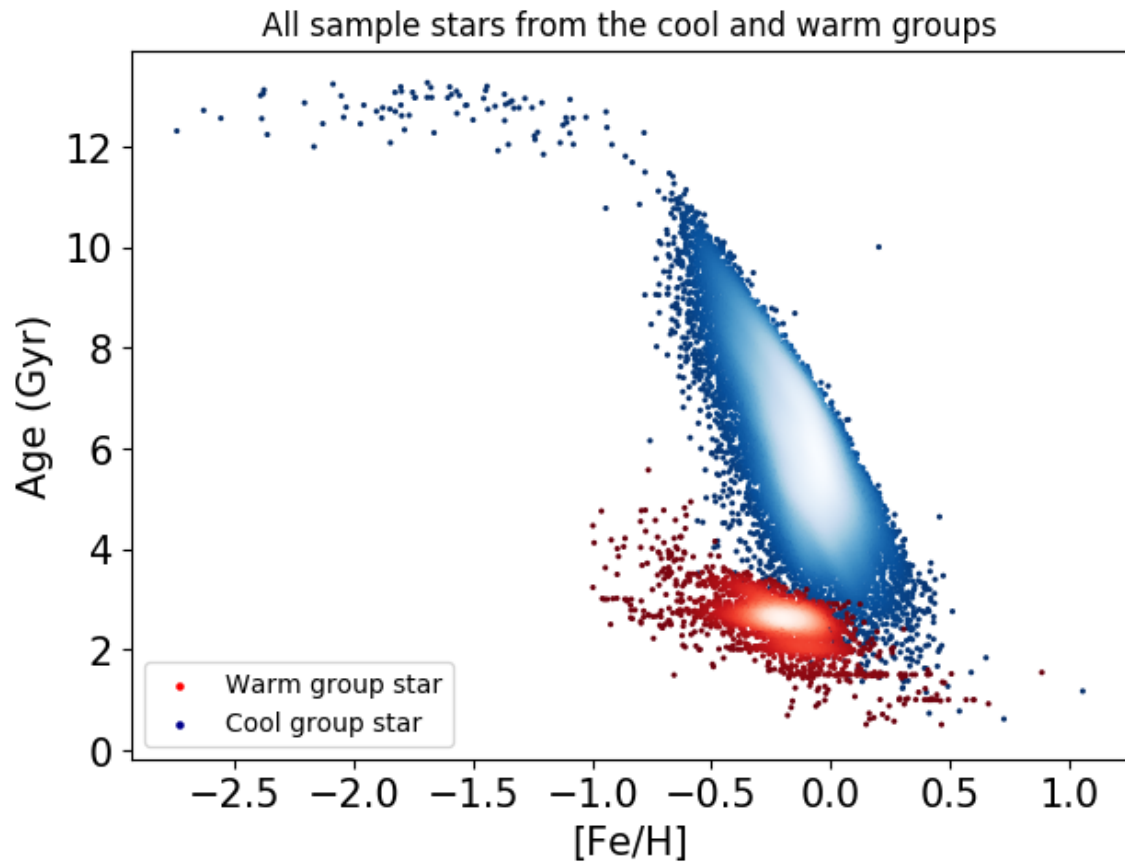
Figure 3.4: **Stellar ages vs. metallicity for all the warm and cool group stars.** The mean ages of the two groups differ strongly with metallicity, from being essentially coeval at very high metallicity to more than 7 Gyrs apart at low metallicity.

From the theoretical side, there are still many uncertainties involved in modelling Li production in GCE. For instance, Li have more than two confirmed types of sources: primodial nucleosynthesis, cosmic rays and stellar production. The stellar production also could come from the novae, red giants, AGB and neutrio-nucleosynthesis in core-collapse super novae, which is still not well known at present. The contribution from all these different sources needs to be well constrained from observations. Additionally, the primordial Li abundance is not well determined for the initial Li in the model, which can strongly affect the results of chemical evolution calculations. Therefore, our observation data of warm group stars can provide a very important constraint for the Galactic Li enrichment.

Prantzos et al. (2017) simulated the evolution of Li in solar neighbourhood (8 kpc from Galactic center) by assuming SBBN as initial Li abundance and low-mass red giants as the main stellar source with radial migration included. A combination of Li production source (i.e., low-mass red giants, that is a long-lived sources with timescale > 1 Gyr), star formation rate early on (decreases in the outer disc) and radial migration (long-lived red giants have time to migrate from inner disc to in-situ and enrich the medium with Li) determines when to break the plateau of Li primordial value (where Galactic enrichment becomes significant). The model prediction shows the high SBBN Li plateau extends till [Fe/H] ~ 0.5 (see the red solid line in the bottom panels of Fig.2 by Prantzos et al. 2017), which is in perfectly agreement with our warm plateau stars.

In addition, it is worth to notice that recent observation of lithium abundance from the low metallicity interstellar medium ([Fe/H] ~ -0.5) of the Small Magellanic Cloud (Howk et al. 2012) and warm stars in open cluster NGC 2243 ([Fe/H] $= -0.52$; an estimated age of 4.3 Gyr; François et al. 2013) are in good agreement with the measurements in our warm stars, showing the sBBN predictions without obvious Galactic lithium enrichment, which can also put strong constraints on the models of Galactic Li enrichment.

3.4.2 Stellar depletion

In this section, we will discuss if the offset (hereafter we call it "depletion correction") obtained from the comparison of cool and warm groups ($-1.0 \lesssim$ [Fe/H] $\lesssim 0.3$) in our observations is applicable to the very metal-poor regime of the Spite plateau stars.

In theory, the generation and amplitude of Li depletion in Population I main-sequence stars strongly depend on the structure of the stellar convective envelope, which in turn depends on the effective temperature of the stars (see Fig. 3.1).

Balachandran (1995) made a comparison of Li-dip features in four different clusters (Praesepe, Hyades, NGC 752 and M67), covering ages between 50 Myr and 5 Gyr, and metallicities between [Fe/H] = −0.15 and +0.12. It is worth to note that the general shape of Li-dip (Li versus T_{eff}) in the Hyades ([Fe/H] = 0.12) and Praesepe ([Fe/H] = 0.04), which are of the same age (750 Myr) but different metallicity, appear to be identical. This indicates that the structure of Li-dip is independent of metallicity at the same age, therefore the depletion of cool stars in the very metal-poor regime should show similar in morphology to that seen for the open clusters. In addition, in the comparison of the four clusters, there is no clearly change in the position of temperature of the Li-dip, nor the shape of the warm edge of the dip with age that have been found. It confirms that Li in the warm stars remain constant with time. However, the cool edge has been discerned that becomes less steep with age, which may indicate that Li of cool group stars in the inactive zone can decrease with age. Therefore, except for the temperature that determines the Li depletion mechanism in each region, stellar ages could be regarded as a secondary regulation for the Li depletion.

As we have mentioned, the age differences between our warm and cool group stars could be very large, especially at the low metallicity (see Fig. 3.4). This may introduce some systematic errors into our depletion correction if the stellar age has a big influence on the Li depletion of cool group stars. For a sanity check, we divide the warm and cool groups into different subgroups based on the metallicity of stars, respectively. In Fig. 3.5 we show Li abundances as a function of stellar age in 12 different metallicity bin for the warm and cool group stars in our sample. From this plot we can confirm that Li follows a linear decrease with stellar age in cool group stars and the the slope of the decreasing trend (depletion rate) becomes a little steeper (larger) as the metallicity increases. For a fair comparison between warm and cool group stars in each metallicity bin, we directly compare the difference between the two groups at the same age (2 Gyr): for the warm groups, we took the mean value of their Li abundances; for the cool groups, we extrapolated the Li abundance at the same age using the linear fitting trend. Therefore, the intrinsic differences at the same age between the two groups should be about ∼ 0.2 dex, which could be applicable to the very metal poor regime (Spite plateau stars). However, the amount of depletion due to ages should also be considered to restore the primordial Li abundances. Then we also extrapolated the linear decreasing trend to the age of Spite plateau stars (∼ 12 Gyr). As we can see in Fig. 3.5, the extrapolated Li abundances show a perfectly agreement with lithium plateau value (A(Li) = 2.22) until [Fe/H] = −0.2 and the amount of depletion from 2 Gyr to 12 Gyr is about 0.3 dex. For [Fe/H] > −0.2 dex, the amount of depletion at the same period become a bit larger due to the higher depletion rate (steeper decreasing trend) in metal rich

stars. As a consequence, a combination of the intrinsic differences caused by the different depletion mechanisms due to the different T_{eff} and the extended depletion with age from cool group stars, leads to the consistent result with the depletion correction deduced from the direct comparison. We also note that the offset showing a slightly trend with metallicity in Fig. 3.3 is the result of the changes of depletion rate of cool group stars in high metallicity.

Additionally, we also stress that theoretical work presented in the literature show that it is indeed possible to reduce lithium in the same way at low and high metallicity. For examples, the models include rotational-induced mixing attempted to reproduce the characteristic features observed in young (Hyades, Li dip) and old stars (Pop II cool stars) in a consistent way (Vauclair 1988), indicating the Spite plateau stars have experienced the Li destruction but failing to explain the low dispersion. The model with coupling atomic diffusion and rotation-induced mixing, has reproduced the Li and Be dip feature in Hyades (Théado & Vauclair 2003) and the lithium plateau in halo stars with low dispersion (Théado & Vauclair 2001) by assuming near solid rotation of stars. Recent studies by Palacios et al. (2003); Talon & Charbonnel (2004) considered more realistic models by allowing rotation braking. Except for diffusion and rotational-induced mixing, they introduce the internal gravity waves (IGWs) into the models as well. In low-mass/Pop II stars, the IGWs become fully activated around $T_{\text{eff}} < 6300\,\text{K}$. Stars can become a near solid body rotator on a short timescale due to the dominant angular momentum transport by IGWs. As a result, the lithium depletion is independent of the initial angular momentum distribution, leading to a low dispersion of lithium abundances from star to star. The Li dip in Haydes is also been reproduced by the same model (Talon & Charbonnel 2005).

It is also great of importance to know if there is still any warm stars alive today in the metallicity range of Spite plateau. Because we did not have any kind of these warm stars in our observation data, thus we plot an evolutionary track of a 0.8 $M_\odot$, [Fe/H] $= -3.0$ metal-poor stars in the HR diagram (see Fig. 3.6). The star ended up in the warm region with a comparable age (11.2 Gyr) of cool Spite plateau stars. However, stellar evolution of the warm metal-poor star is quite different with the warm stars of higher metallicity in our sample. It has gone across the Li-dip region before it became a warm star, which means a severe depletion is expected to occur. Therefore, it could be highly possible that we can not observe Li detections from those warm metal-poor stars, even they could still be alive today.
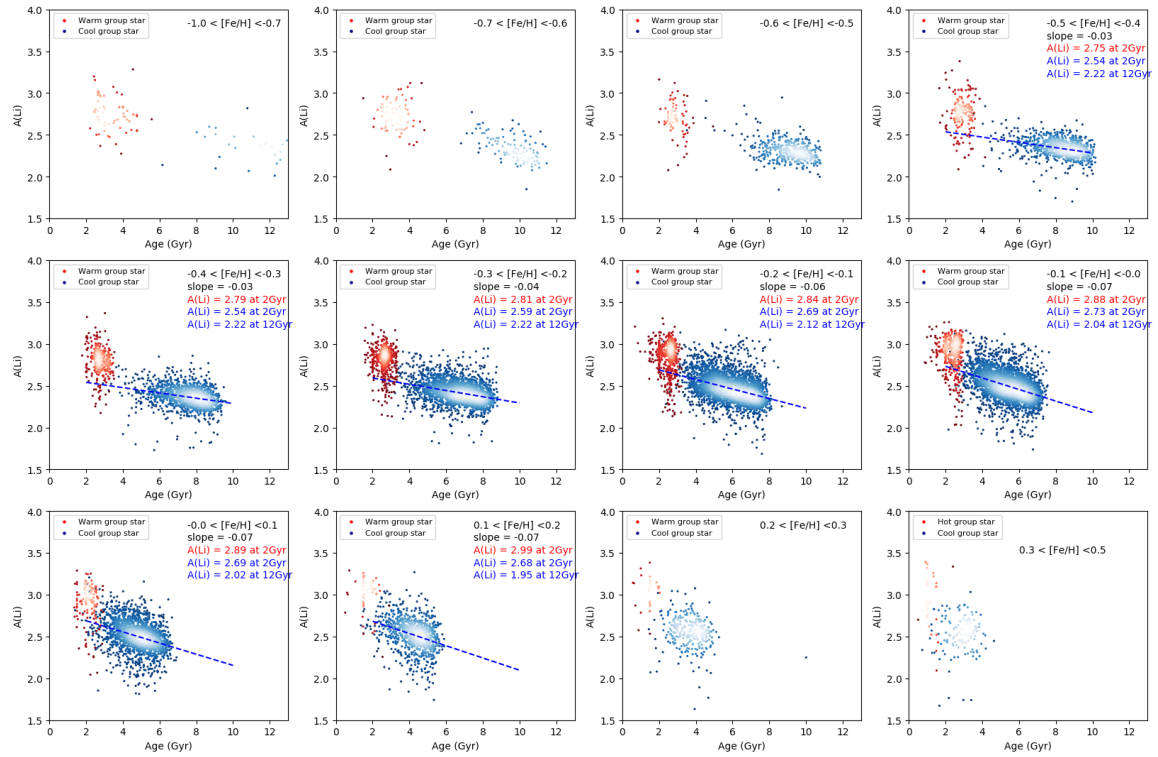
Figure 3.5: **Li as a function of stellar age for cool and warm group stars in the sample, in different metallicity bins.** A linear fit has been applied to the cool group stars in each panel in which has enough number of stars.
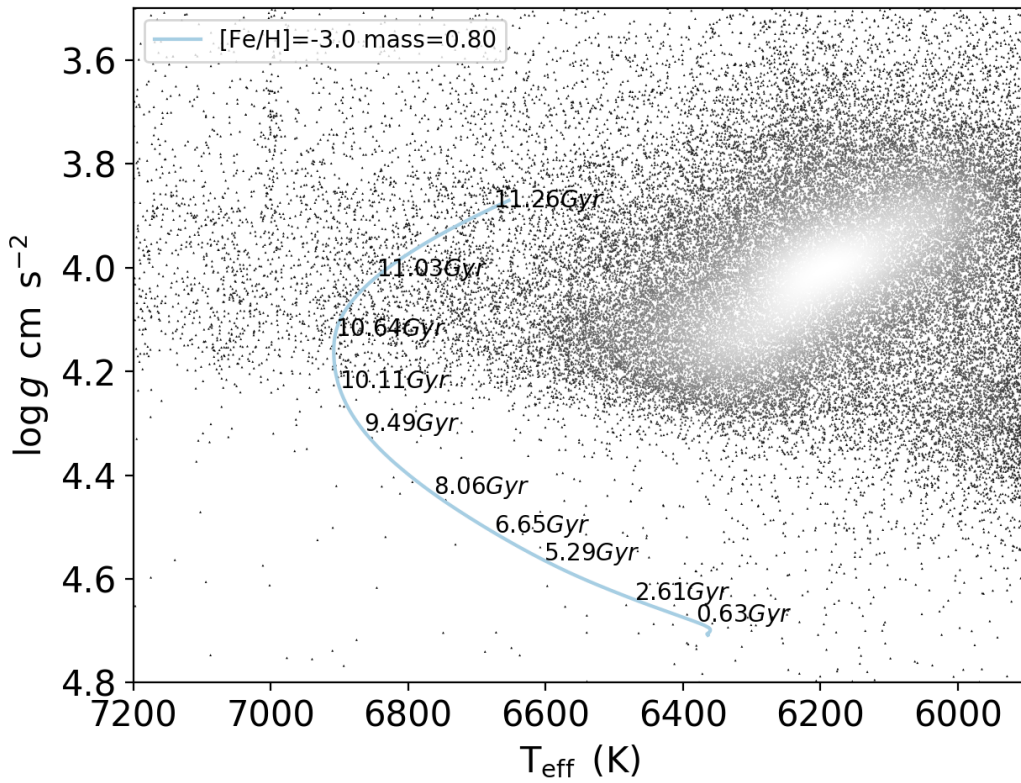
Figure 3.6: An evolutionary track of a 0.8 M$_\odot$, $[\mathrm{Fe/H}] = -3.0$ metal-poor stars are shown in the HR diagram. Stars with Li upper limits of our sample are also overplotted.

3.5 Conclusion

In this work we investigated the behaviour of Li among late-type stars including MS, turn-offs and early subgiants, based on the largest sample so far covering a wide range of metallicities with a homogeneous Li determination from GALAH survey. To reduce the complex behaviour of Li-dip stars, we only extracted the warm and cool group stars, which are on the warm and cool side of dip region, respectively. We summarize the implications that can be obtained from our result as follow:

- Firstly, our warm and cool groups can be used to empirically constrain lithium depletion mechanisms within stars. We confirmed that Li depletion in the warm group stars is negligible, because of their consistency with the predictions of SBBN at low metallicity. A nearly constant offset of the differences of the mean Li abundances (0.45 ± 0.02 dex; depletion correction) between the warm and cool group stars at each metallicity has been found. The metallicity-independent depletion correction can be interpreted as a combined result of the intrinsic differences caused by the T_{eff}-dominant depletion mechanism and the extended depletion with age from cool group stars. The depletion rate keeps almost constant at low metallicity ([Fe/H] < -0.2) resulting in the uniform Li depletion in the Spite plateau nearly independent of metallicity, however, becomes faster at higher metallicity.

- Secondly, it can be applied to constrain BBN and understand how much Li was depleted by Spite plateau stars. We can extrapolate the behaviour of stars in the metallicity regime $-1 \lesssim$ [Fe/H] $\lesssim 0.3$ to lower metallicity, we can put a lower bound to how much Li was probably lost from the atmospheres of stars on the Spite plateau. Spite et al. (2012) and Spite et al. (2015) collected all the field turn-off stars with available Li measurements in the literature. By selecting stars with a temperature higher than $5900\,\mathrm{K}$ and a metallicity between [Fe/H] = -2.8 and [Fe/H] = -2, they found the Li abundance is remarkably constant with the very small scatter (A(Li) $\approx 2.2 \pm 0.06$; lithium plateau). In the same metallicity interval, we find the mean Li abundance of our plateau stars is A(Li) = 2.21 ± 0.04. Since the depletions correction are stable between the two groups, we can apply it directly to our plateau stars to estimate the true primordial Li abundance (A(Li) = 2.71 ± 0.04), which is compatible with newest improved primordial Li of standard BBN (A(Li) = 2.75 ± 0.02 Pitrou et al. 2018) within the standard errors.

- Thirdly, it can impose strong constraints on Galactic chemical evolution (GCE) of Li. Due to the fact that Spite plateau stars belong to the cool group, which

have already experienced a large uniform depletion and do not reflect the true primordial value of Li, we also suggest to apply the predicted Li abundance of SBBN instead of Spite plateau as initial value in the GCE models. By comparison of mean Li abundances of two group stars, it will help to determine the turning point where Li abundances break the plateau and the Galactic Li production becomes significant ([Fe/H] ~ -0.5). The model prediction by assuming SBBN as initial Li value and low-mass red giants as main stellar sources (Prantzos et al. 2017) shows the high SBBN Li plateau extends till [Fe/H] ~ 0.5 , which is in perfectly agreement with our warm plateau stars.

Chapter 4

Lithium enrichment of the Galactic thick and thin disks

The following chapter contains a draft version of an article that is prepared to be submitted.

4.1   Introduction

In principle, one would expect the observed surface abundances in low-mass stars reflect the corresponding chemical composition of their progenitor gas where those stars originally formed. These information will be very helpful to constrain the chemical evolution models. However, Li as a special and fragile element that can be easily destroyed at a relatively low temperature ($\sim 2.5 \times 10^6$ K) in stellar interior, will complicate the situation. In Chapter 3, we have mentioned the complex behavior of Li abundances in late-type stars, namely, Li can vary drastically over a small range of effective temperature during the main-sequence. Moreover, a significant difference between the current photospheric Li abundance in the Sun (A(Li) = 1.05 ± 0.10 Asplund et al. 2009) and the protosolar value that measured in meteorites (A(Li) = 3.26 ± 0.05 Asplund et al. 2009), also indicates a large internal Li destruction. To constrain the observations, more complicated mechanisms and physical mixing processes need to be taken into account in stellar evolution model (e.g. Michaud et al. 2015; Pinsonneault 2010; Talon & Charbonnel 2010). The difficulty of linking the two aspects between theories and observations, makes it hard to apply the stellar Li abundances into Galactic chemical evolution (GCE) models (e.g. Romano et al.

1999), which leads to anther puzzling topic, i.e., Galactic Li evolution.

Li is also a unique light element that has more than two sites of production: primordial nucleosynthesis, spallation reactions in cosmic rays and stellar production (e.g. Prantzos et al. 1993; Romano et al. 2001; Travaglio et al. 2001; Prantzos 2012). Among these sources, the first two have been well constrained by observations and can contribute less than 30% of the meteoritic Li abundance (Prantzos 2012), which means most of the solar system Li may originate from the thermonuclear reaction in stellar interior. Many candidates have been proposed to be responsible for the majority of stellar Li production. For instance, core-collapse supernova (CCSN, through ν-induced nucleosynthesis; Domogatskii et al. 1978), novae (through explosive hydrogen envelope burning; Starrfield et al. 1978), intermediate-mass stars on asymptotic giant branch (AGB, through hot-bottom burning; Sackmann & Boothroyd 1992), low-mass stars on red giant branch (RGB, shell H-burning; Sackmann & Boothroyd 1999). However, the relative importance of these different kinds of stellar sources for the Li enrichment is difficult to determine by current observations and still somewhat debatable (e.g. Travaglio et al. 2001; Prantzos 2012)

The contribution of Li production from CCSNe ought to be inefficient at a Galactic level and no observations have been found to support this mechanism (Romano et al. 1999; Nomoto et al. 2013). Fu et al. (2018) found a anticorrelation between Li and α abundances ($[\alpha/\mathrm{Fe}]$) in the main-sequence field stars, indicating the contribution of Li enrichment from CCSNe should be insignificant. Since CCSNe are the main producer of the α elements, a positive correlation between Li and α abundances is expected to be seen if CCSNe are also responsible for a major Li production. Recent detection of Li in the spectra of the nova outburst events, have revived the interest that nova systems could be potentially the major source of the enriched Li observed in the young stellar populations (Izzo et al. 2015; Tajitsu et al. 2015, 2016). Furthermore, Cescutti & Molaro (2019) and Grisoni et al. (2019) all adopted novae as the main Li producer into the chemical evolution models to account for the observed increase of Li abundances with stellar metallicity in the thin disk. However, Prantzos et al. (2017) emphasized that the contribution of novae to the Galactic Li evolution could still be very uncertain, due to the unknown past rate of novae (their dependence on metallicity) and the problem of the overproduction of minor CNO isotopes in all novae models. Instead, they considered the other two types of sources into their GCE models including radial migration: long-lived RGB (a few Gyr) and short-lived AGB stars (several 10^8 yr). They concluded that long-live RGB as the stellar Li source can reproduce the Li evolution in thick and thin disks very well.

The current discrepancy of primordial Li between the predictions of SBBN

(Pitrou et al. 2018) and the observed Spite plateau (Spite & Spite 1982) makes it impossible to determine the initial Li in GCE models. Since the initial value of Li has a strong influence on the calculations of chemical evolution, a direct comparison between observations and models would not be straightforward. Therefore, most of studies would usually consider both cases (high Li from SBBN and low Li from the Spite plateau) in their simulation (see e.g. Prantzos et al. 2017; Grisoni et al. 2019; Cescutti & Molaro 2019, and references therein). Fortunately, our study in Chapter 3 concluded that SBBN prediction is highly to be the primordial value, as the Spite plateau stars have been confirmed to experience a Li depletion of about 0.45 dex.

The unknown origin of thick and thin disks is another problem to impede understanding Galactic Li evolution. Since the relation between thick and thin disks are not clearly identified, it is hard to have a universal separation between the two types of disks, which depends on the definition one adopts for thin and thick disks (Kawata & Chiappini 2016). Different separation criteria can lead Li to behave quite differently in the thin and thick disks. Ramírez et al. (2012) presented a first attempt to compare Li abundances in the Galactic thick and thin disks, using a kinematical criterion as defined in Bensby et al. (2003) to separate the two disks in their sample. They found that the maximum (upper envelope) Li abundance of thick disk stars appears to be nearly constant till to $[\text{Fe/H}] \sim -0.1$ and have a similar value to that of Spite plateau halo stars, suggesting that the enrichment histories of thick disk stars have been erased from their stellar atmospheres. On the other hand, the Li trend in the thin disk stars shows an apparent enrichment with increasing metallicity. Delgado Mena et al. (2015) examined their sample by using both kinematical (Bensby et al. 2003) and chemical criteria (Adibekyan et al. 2012) to separate the stellar populations. They also found that Li trends behave differently in the two disks, however, Li abundances in their thick disk stars start to show a decrease with metallicity from $[\text{Fe/H}] \sim -0.5$ rather than being flat. Guiglion et al. (2016) using the AMBRE project data and Fu et al. (2018) using the Gaia-ESO survey data both adopted the same chemical criterion as described in Recio-Blanco et al. (2014) to separate the thin and thick disc stars. They both showed that the Li abundances increase slightly with metallicity for the thick disk stars, while a steeper increase for the thin disk stars. It indicates that the two disks should have experienced Li enrichment, but with different sources. All these studies seem to show a general agreement that there is an increase of Li in the thin disk, but have different conclusions about how Li evolves in the thick disks, especially towards higher metallicities.

More recently, Bensby & Lind (2018) carried out a detailed comparison

with different selection criteria (kinematical, chemical and age) by investigating a well-studied sample of 714 nearby F and G dwarf, turn-off and subgiant stars in the Galactic disk. They summarized that kinematical selection criteria is not a good choice to separate the stellar populations, since the velocity distributions are widely overlapped between the two disks, especially at high metallicities. On another hand, chemical selection criteria are commonly used due to the distinct α-elements abundance trends of two disks (e.g. Adibekyan et al. 2012; Bensby et al. 2014). However, the separation also becomes more difficult at higher metallicities, as the α abundance trends converge towards solar metallicities. Therefore, applying either kinematical or chemical criteria in the selection of stellar populations, will result in more contamination of thin disk stars into the thick disk sample with increasing metallicity. They found that the Li trend in their thick disk shows a steady decrease at metallicities above [Fe/H] ~ -1.0, by using a more robust stellar age criteria to select the thin and thick disk samples. It indicates that no significant Li production in the Galactic thick disk during the first few billion years and the main source for Li production could be the long-lived low-mass RGB stars.

In addition, in order to have a comprehensive study of the Li behavior in the Galactic disk, statistically significant and homogeneously analysed samples covering a wide range of metallicities are needed. However, very few studies reported their Li analysis based on few hundreds of stars (e.g. Ramírez et al. 2012; Delgado Mena et al. 2015). More recently, Guiglion et al. (2016) and Fu et al. (2018) investigated the Galactic Li evolution for a much larger sample of a few thousands of stars based on the homogeneous analysis of high-resolution spectra.

In this work, we will construct the largest available catalog of Li abundances of nearby FGK dwarf and subgiant stars for the study of Galactic Li evolution based on the wealthy of available data from GALAH iDR3. Then we will have a detailed study of chemical evolution of Li abundance in different local disk stellar populations. In the last, we will compared our observational data with chemical evolution models and try to figure out how Galactic Li enrichment has proceeded in the thin and thick disks.

4.2   Observation data

Our baseline sample for this study of the Galactic Li evolution is from the same dataset as used in Chapter 3. The total catalogue contains more than 650 000 field stars in the solar neighbourhood that have been collected by spectroscopy survey of GALAH (De Silva et al. 2015) and its sister surveys TESS-HERMES (Sharma

et al. 2017) and K2-HERMES (Sharma et al. 2019). The stellar parameters and Li abundances are derived from the spectra with a resolving power of $R \approx 28\,000$ in GALAH iDR3 using the GALAH spectrum synthesis analysis pipeline (see Chapter 2 or Buder et al. 2018, for a detailed description of the method).

4.3   Sample selection

To investigate the history of Galactic Li enrichment, we aim to select the stars that have the least internal destruction or well-constrained/determined Li depletion from the GALAH iDR3 catalogue. Evolved giant stars should be excluded in the first place, because their surface Li abundances no longer contain the information of Galactic Li enrichment history and have significantly decreased at this stage due to the dilution driven by the first dredge-up and destruction by the deepening surface convective zone. We thus set the surface gravity $\log g = 3.7\,\mathrm{dex}$ as the lower bound of our sample to separate the dwarf and giant stars, same as the criterion used in Fu et al. (2018). We also set the upper bound of the surface gravity as $\log g = 4.4\,\mathrm{dex}$ to reduce any possible contamination of pre-main-sequence stars. For this work, we mainly focus on the sample with a T_{eff} ranging from 5900 to 7200 K and covering a large range of metallicity from $[\mathrm{Fe/H}] = +0.5$ to $[\mathrm{Fe/H}] = -3.0$.

Our sample mainly consists of main-sequence, turn-off and slightly evolved subgiant stars. However, main-sequence stars within a narrow range of T_{eff} centered around 6700 K can experience a huge Li depletion, known as Li dip stars (see e.g. Boesgaard & Tripicco 1986; Balachandran 1995; Boesgaard et al. 2016). Because dip stars are still not well-constrained by stellar evolution models currently and their temperature would be different from their main-sequence temperature as they evolved off the main-sequence. Therefore, it is very difficult to totally remove them from our sample. To exclude the Li dip stars in our sample, we applied the same selection method as described in Chapter 3. In brief, we rule out the majority of Li dip stars based on the morphology of Li upper limits in the HR diagram (see the detailed division in Fig. 3.2). The warm and cool group stars on both sides of the Li-dip region have been retained.

In Chapter 3 we have made a huge progress in understanding the Li depletion histories by comparing the warm group with cool group stars. We concluded that Li abundances in warm group stars are barely depleted and remain the initial value at the surface, while Li abundances in cool stars show a stable depletion at the surface. The depletion correction we found between the two groups can be summarized as: $D_{\mathrm{cor}} = \Delta\mathrm{Li}_{\mathrm{int}} + \Delta\mathrm{Li}_{\mathrm{evo}}$, where $\Delta\mathrm{Li}_{\mathrm{int}}$ represents the intrinsic difference between the

two groups at a given age due to the different Li depletion mechanisms dominated by the T_{eff}. $\Delta\text{Li}_{\text{evo}}$ stands for the long-term evolution difference mainly because of age differences between the two groups, coming from the cool group stars with a slow depletion rate. This means that T_{eff} can be regarded as a key parameter to trace the stellar Li destruction at a given age and stellar age can be a secondary effect for the extent of depletion of cool group stars in the long-term evolution.

For the first time, we have constructed a catalog of stars that have experienced the least and stable amount of lithium depletion from the selected warm and cool group stars in Chapter 3. our sample can be used as the reliable tracers of Galactic Li enrichment and is very suited to study systematic differences in the chemical evolution of Li between the thin and thick disks. To reduce the contamination from the minority of bulge stars in our sample, we also remove any stars with a galactic latitude $|b|$ less than 10°. Note that our data set also includes a small fraction of halo stars, which can be used to connect with the low metallicity regime relating to the primordial Li abundance. In this study, we simply regard stars with [Fe/H] < -1 as local halo stars. Our final sample is composed of mainly the nearby Galactic disk stars and a small fraction of local halo stars: 2460 stars with Li detection and 4946 stars with Li upper limits from warm group and 14982 stars with Li detection and 1746 stars with Li upper limits from cool group.

4.4   Results

In Fig. 4.1 shows how the Li abundances of all the warm and cool group stars in our sample vary with stellar effective temperature, surface gravity, mass and age. It is clear to be seen that the two groups are well-separated in every stellar parameter space. We stress that our sample includes not only main-sequence stars, but also includes turn-off and slightly evolved subgiants. The stellar parameters of those evolved stars will be changed as they moved off main-sequence stage, which could lead to an extension distribution of the stellar parameters. For instance, the extended distribution of effective temperature of warm group stars in the A(Li)-T_{eff} panel. Another reason makes the data of field stars more difficult to be interpreted than cluster data is the mixture of ages and metallicities. We note that the "Li desert" reported by some recent studies (e.g. Chen et al. 2001; Ramírez et al. 2012; Aguilera-Gómez et al. 2018), a small region around $T_{\text{eff}} \approx 6050\,\text{K}$ and A(Li)$\approx$1.8 sparsely populated by stars, is not shown in our sample. We suspect that it could be caused by the observational selection effect due to the small sample in their studies.

No strong correlation between Li abundances and surface gravity have been
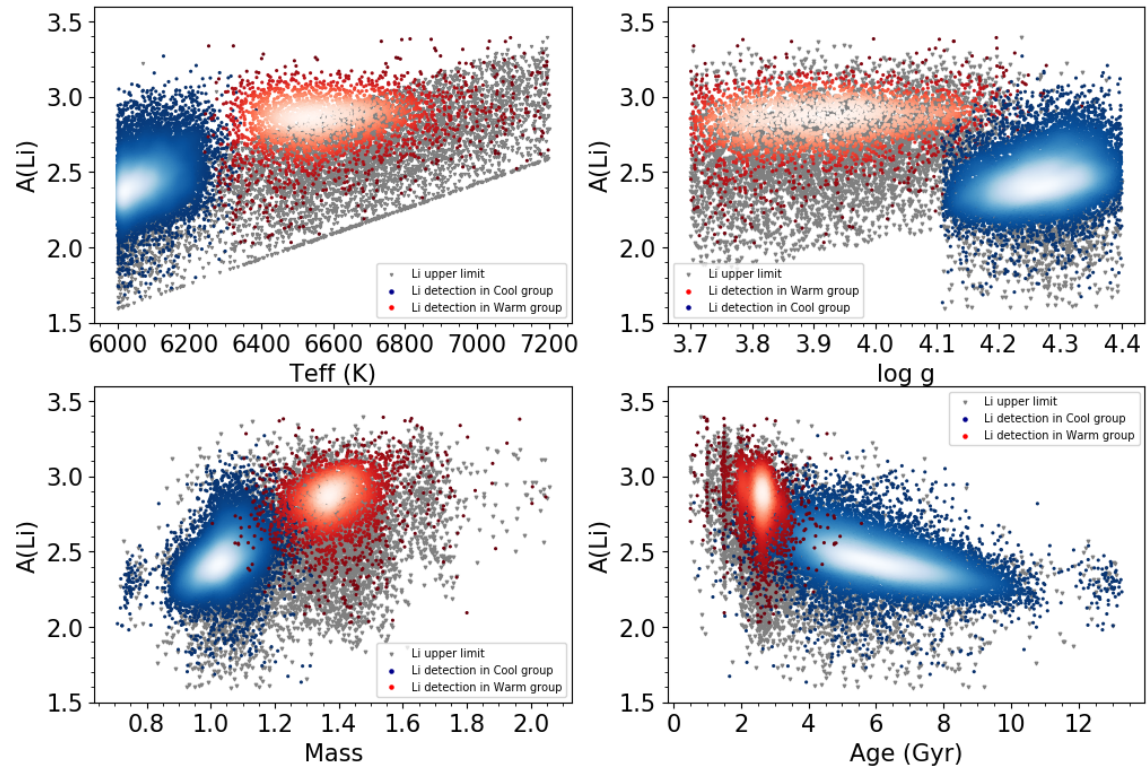
Figure 4.1: **Li abundances versus effective temperature, surface gravity, stellar mass and age for all the warm and cool group stars.** In each panel, Li detections in each group are plotted as colour-coded density, with brighter colours implying higher density. All the 6 692 stars that only have upper limit Li abundances are plotted as grey downward triangles.

found in each group in the A(Li)-log g panel of Fig. 4.1. Most of warm stars located at log $g \lesssim 4.1$ show an essential higher Li abundance than the cool stars at higher surface gravities. A(Li)-Mass panel shows most of the cool group stars have a mass lower than $1.25 \, M_\odot$, while warm stars have a higher mass. A clear correlation in A(Li) versus stellar mass and age has been found in cool group stars. The differences of Li abundance could be partly caused by the subtle bias of stellar mass. The age relation in cool stars shows Li abundances stay constant for the first few billion years and start to increase with decreasing age around eight billion years ago, indicating the period when the Galactic Li enrichment becomes significant.

As we mentioned in the introduction, it is not straightforward to have a well-defined criterion using either kinematical or chemical method to separate the Galactic thick disk from thin disk stars, especially at high metallicities. In this work, we applied the robust age criteria in Bensby et al. (2014) and Bensby & Lind (2018) to separate our sample into old (> 8 Gyr) and young (< 8 Gyr) subsamples, corresponding to the thick and thin disks, respectively. Fig. 4.2 shows Li abundances of true measurements and upper limits as a distribution of metallicity for the thick and thin disks. Our data clearly indicate different trends for the two disks. Both warm and cool stars in the thin disk show an apparent and similar increase with metallicity. For the warm stars, the Li abundances stars at a level comparable to the SBBN primordial value and increase towards solar metallicity. On the other hand, although the thick disk overlaps with the thin disk in metallicity, stars in thick disk are systematicaly older than the thin disk. Therefore, the warm stars with higher masses are not found in the thick disk. In contrary to the Li pattern of thin disk, the old thick disk sample consist of stars from cool group appear to have a nearly constant mean Li abundance, of which is similar to that of the Spite plateau exhibited by very metal-poor stars. At the metal-rich end, the Li trend shows a slight increase. In general, it indicates that there is no significant Li enrichment during the earlier phases of the thick disk.

However, Bensby & Lind (2018) showed that Li trend of thick disk to be clearly decreasing with metallicity using the same age criteria. We speculate that the reason for the apparent Li decrease in their thick disk, could be that many stars with temperature below $5900 \, K$ have been included in their sample. Li in those cooler stars will experience a higher degree of depletion due to the larger convection zones. The larger depletion from stellar itself will result in removing any signature from the history of Galactic Li enrichment.

In Fig. 4.3, we show the Li abundances versus metallicity in our halo stars. Those stars with Li measurements are marked in grey, showing a comparable value to the Spite plateau. For the stars with Li upper limits, we found that there are a
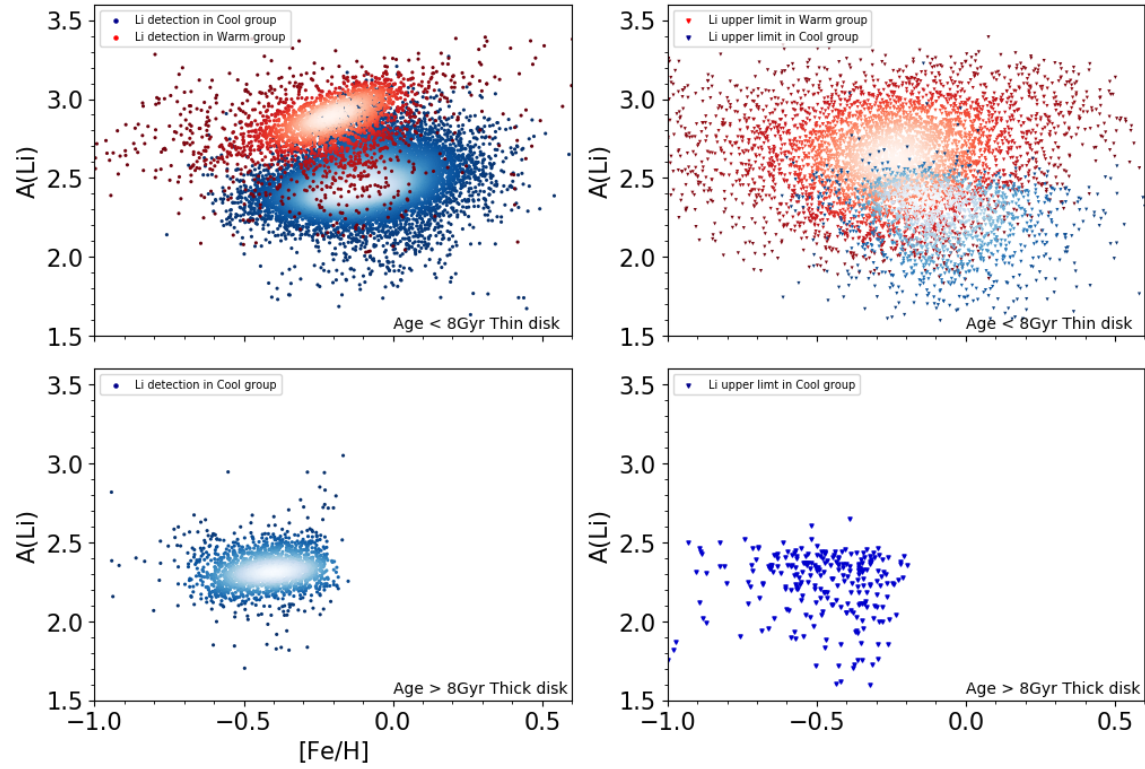
Figure 4.2: **Li abundances of measurements and upper limits as a function of metallicity for the thin (top panels) and thick disks (bottom panels).** The separation of the Galactic populations are based on the stellar age (8 Gyr). Warm and cool stars in the thin disk are depicted with red and blue density symbols (top panels). Downward triangles represent upper limits on Li. Thick disk only contain cool group stars (bottom panels).

number of very young ($\sim 4-6\,$Gyr) metal-poor stars covering a range of stellar mass $0.9 M_\odot \lesssim M \lesssim 1.3 M_\odot$ in this Spite plateau regime. Their stellar ages would be very suspicious if they are at the lower main-sequence, due to the large uncertainties. However, it would be interesting to have a further investigation on them, since we expect to find any warm group stars in this metal-poor regime (see discussion in Chapter 3).
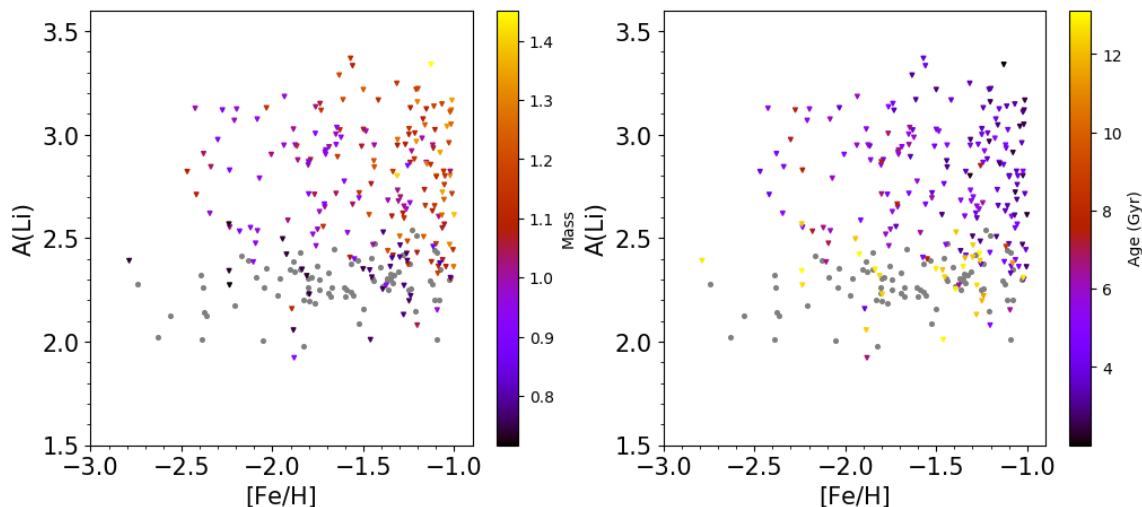
Figure 4.3: **Li abundances of measurements and upper limits as a function of metallicity in Galactic halo stars.** Stars with Li measurements are shown as grey circle. Stars with Li upper limits are colour-coded based on their stellar masses (left panel) and ages (right panel), respectively.

Fig. 4.4 shows the comparison of our measured Li with predicted Li from different GCE models as a function of metallicity. We bridge our sample from the very metal-poor to the super-solar metallicity by including all the measured Li of halo, thick and thin stars. Since Li depletion during the evolution of main-sequence is not well-understood, which is a important link between the interstellar medium (ISM) Li abundances and the current abundances measured in field stars. Therefore, a direct comparison of model results to observations with a large dispersion, is not straightforward. A conventional way for probing the Galactic Li evolution is to take the upper envelope of thin disk stars over the metallicity range as the initial Li value to match with the model results. For example, many recent studies used the same method by selecting the six stars with the highest Li in each [Fe/H] bin and then calculating their mean values to track the enrichment trend (Lambert & Reddy 2004; Delgado Mena et al. 2015; Guiglion et al. 2016; Fu et al. 2018). We stress that in our sample we have selected the stars with the least amount of depletion (warm group stars) and stars with well-determined Li depletion (cool group stars) by excluding
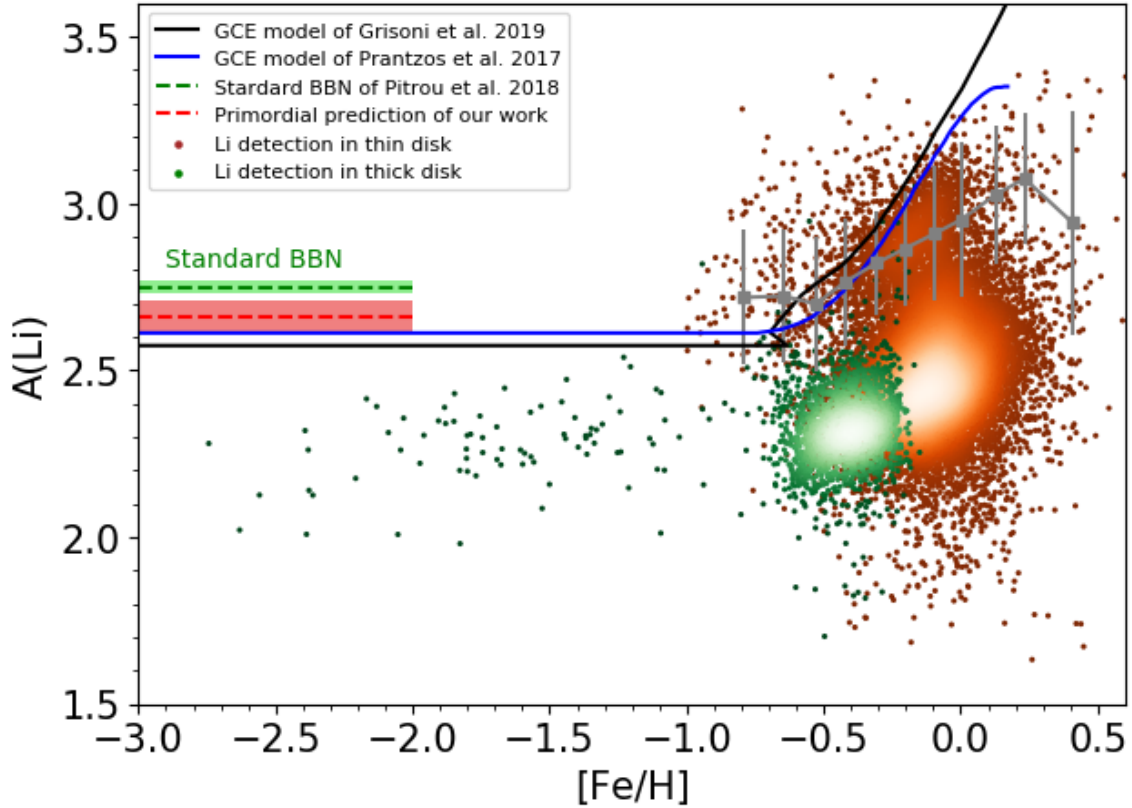
Figure 4.4: **A comparison of measured and predicted Li abundance as a function of metallicity in the solar neighbourhood.** All the measured Li abundances from thick, thin and halo stars are plotted as colour-coded density. The blue and black solid lines denote the Li predictions of GCE models from Prantzos et al. (2017) and Grisoni et al. (2019), respectively. The primordial Li abundances from SBBN (Pitrou et al. 2018) and our prediction in Chapter 3 are provided as green and red dashed lines, respectively. Grey squares represent the mean Li abundances of each metallicitiy bin in warm thin-disk stars. The error bars display the corresponding $1-\sigma$ dispersion.

most of stars have experienced severe Li depletion (Li-dip stars). Therefore, we take the mean Li abundances of each metallicitiy bin of warm stars in thin disk as the initial values, instead of taking the upper envelope in this study. The general Li trend shows a high plateau comparable to primordial value of SBBN at low metallicity, a steay increase with metallicity above -0.6, and a sudden decrease at super-solar metallicity that was also been pointed out by recent studies (e.g. Delgado Mena et al. 2015; Guiglion et al. 2016; Fu et al. 2018; Bensby & Lind 2018)

Since we have confirmed the surface Li abundances of the Spite Plateau do not in fact reflect their initial value, but have experienced a depletion of about $0.45\,$dex based on the statistically significant observational GALAH data in Chapter 3. Therefore, both GCE models we applied here are all assuming the high primordial Li abundance of SBBN as the initial value. However, we note that the initial value of both models are still lower than the newest updated SBBN predition by around $0.15\,$dex.

The model of Grisoni et al. (2019) takes into account novae as the main-source, which lead to contribute the Li enrichment in the thin disk formed on a relatively long timescale. The significant Galactic enrichment takes place, where the formation of the inner halo and thick disks has finished, at around $[\text{Fe/H}] \sim -0.8$ that is earlier than our general Li trend, Moreover, the model prediction keep rising after the meteoritic value is reached, which fails to match the with observations at super-solar metallicity.

The model of Prantzos et al. (2017) adopted low-mass RGB stars as the main Li production source including radial migration. The effect of radial migration can transfer the source of inner disk to the outer disk and enrich the local Li, leading to break the primordial value earlier in that area. The slope of the Li enrichment also depends on the star formation rate in the same zone. The presence of radial migration makes the model more complex but also more flexible to be tuned, which means the break point or the slope of Li enrichment can be changed by adjusting the radial migration and star formation rate early on to match the observation data. The mean Li trend in our warm stars show a general agreement within the consideration of error.

4.5   Conclusion

In this work, we selected construct a catalogue that used for the study of Galactic Li evolution using the GALAH iDR3 data. The sample consist of stars with the

negligible Li depletion and stars the well-determined Li depletion from the warm and cool group defined in Chapter 3, respectively. 17 442 of the sample have a determined Li measurement and the rest 6 692 stars we present upper limits to their Li abundances. The warm and cool group stars in our sample are well-separated with the stellar effecitve temperature, surface gravity, mass and age. Li desert reported by other recent studies are not shown up in our sample.

We separate our sample into the thick (> 8 Gyr) and thin disks (< 8 Gyr) based on the age criteria used in Bensby & Lind (2018). Our data show clearly different trends between the two disks. The Li abundances increase with metallicity in the thin disk, while the thick disk show a nearly constant Li trend comparable to the Spite plateau value, which reflects the different Li enrichment histories. In the last, we take a comparison of our measured Li abundance to the predicted Li results from two GCE models. Our mean Li trend in the warm thin-disk stars shows a general agreement with the prediction from the model of Prantzos et al. (2017), which takes into account low-mass RGB stars as the main Li production source including radial migration.

Chapter 5

Conclusion and Outlook

5.1 Conclusion

The aim of this thesis is to improve the understanding of physical processes that influence the surface chemical abundances in low-mass stars. As tools, we applied the high-precision analysis to extract chemical information from the GALAH spectra by performing detailed 1D non-LTE calculations.

In Chapter 2 we investigated the evolutionary effects on chemical abundances in old open cluster M67. In this case, 66 member stars covering main-sequence turn-off, subgiant, red giant, and red clump stars are been selected from the the GALAH high-resolution, high-quality spectra seven elements have been analysed from the spectra using 1D non-LTE and LTE, respectively. we found abundance trends with stellar effective temperature in all of the analysed elements. Even non-LTE analysis tends to flatten the abundance trends that seen in LTE, but still remained noticeable. This indicates that the surface chemical composition does not exactly match the bulk chemical composition, but rather it varies with stellar evolutionary phase. By comparing with atomic diffusion models, the abundance trends in $\log g$ for most elements show good agreement with the model predictions. We thus concluded that the process of atomic diffusion poses a non-negligible effects during the main-sequence phase, which leads to chemical inhomogeneities in open clusters.

In Chapter 3 we used GALAH iDR3 data including over 100,000 stars in the solar neighbourhood to study the Li depletion among late-type stars. Our sample was separated into two groups corresponding to the cool and warm side of the so-called "Li dip" region in the HR diagram. The cool group stars correspond to the "Spite plateau" stars in the low metallicity regime. We discovered that stars

97

either side of the dip show similar trends of lithium versus metallicity, but are offset in lithium by a factor of 2.8, with the "warm stars" (hotter than the dip) having higher lithium abundances. The metallicity-independent offset can be interpreted as a combined result of the intrinsic differences caused by the T_{eff}-dominant depletion mechanism and the extended depletion with age from cool group stars.

We confirmed that Li depletion in the warm group stars is negligible, because of their consistency with the predictions of BBN at low metallicity $-1 \lesssim [\mathrm{Fe/H}] \lesssim -0.5$. While the surface Li abundances of these Spite Plateau do not in fact reflect their initial (SBBN) Li abundances. Since the offsets are stable between the two groups in the metallicity regime $-1 \lesssim [\mathrm{Fe/H}] \lesssim 0.3$, we extrapolated the offset directly to our plateau stars to estimate the true primordial Li abundance (A(Li) = 2.71 ± 0.04), which is compatible with newest improved primordial Li of standard BBN (A(Li) = 2.75 ± 0.02 Pitrou et al. 2018) within the standard errors. This further strengthens the case for an astrophysical solution to the cosmological lithium problem, reconciling tensions with SBBN.

In Chapter 4 we carried out a follow-up study based on the result and observational data in Chapter 3. We have constructed the largest available catalogue of Li abundances of nearby FGK dwarf and subgiant stars from GALAH iDR3 data for the study of Galactic Li evolution. The final sample consist of warm group stars with the negligible Li depletion and cool group stars with the stable Li depletion: including $17\,442$ stars with determined Li measurements and $6\,692$ stars with upper limits to their Li abundances. We further separate our sample into the thick (> 8 Gyr) and thin disks (< 8 Gyr) based on the age criteria used in Bensby & Lind (2018). Our main finding is that the evolution trends of Li in the Galactic thin and thick disks show distinctly different, which reflects the different Li enrichment histories: the Li abundances increase with metallicity in the thin disk, starting to show an apparent enrichment at metallicity around $[\mathrm{Fe/H}] = -0.6$; while the thick disk show a nearly constant Li trend comparable to the Spite plateau value, indicating that there is no significant Li enrichment during the early phase of the thick disk formation. By comparing our measured Li abundance with the predicted Li results from two GCE models. Our mean Li trend in the warm thin-disk stars shows a general agreement with the prediction of the model by Prantzos et al. (2017), which takes into account low-mass RGB stars as the main Li production source including radial migration.

5.2 Outlook

5.2.1 High-accuracy stellar element abundances : 3D non-LTE analysis

In Chapter 2 we investigated the atomic diffusion effects on chemical inhomogeneities in open cluster M67 in the context of 1D non-LTE analysis. Even though the model predictions can generally match the elemental abundance trends, however, because of the small amplitude of its effects, it is hard to totally remove the abundance trends for all the elements and also could be difficult to disentangle them from other possible systematic bias in the analysis.

It may be necessary, however, to further increase the accuracy of the stellar abundance analysis. The next level of accuracy can be attained by using 3D hydrodynamical model atmospheres, while simultaneously accounting for departure from LTE; i.e. by performing so-called 3D non-LTE abundance analyses. Such modelling is very important for atmospheres of late-type stars, where the spectral line form at the top of the convective region. The artificial broadening parameters, such as microturbulence and macroturbulence are not necessary any more (e.g. Asplund et al. 2000). Consequently, it is possible that a 3D non-LTE analysis would provide unbaised results and find significantly flatter or steeper abundance trends than those presented in Korn et al. (2007).

In Chapter 3 we tried to provide a very promising solution to the Cosmological Li problem through finding clues for Li depletion in the Spite plateau from the astronomical side. Another possible way to overturn the Li depletion and also SBBN is to find observation evidence of ^{6}Li measurements in any metal-poor stars. Since this fragile Li isotope are more easily to be destroyed than ^{7}Li (Brown & Schramm 1988), moreover, SBBN does not produce ^{6}Li in the early universe (Cyburt et al. 2016). ^{6}Li measurements are difficult and could be very controversial due to its slight depression and asymmetry feature in the red wing of resonance line of Li. 3D non-LTE modelling are thus needed to precisely disentangle the line feature (Asplund et al. 2006; Cayrel et al. 2007; Lind et al. 2013).

5.2.2 Bridge the whole evolution picture of Li : from extremely metal-poor to super-solar metallicity

Thanks to the advent of large stellar spectroscopic surveys, such as, APOGEE (Majewski et al. 2017), Gaia-ESO (Smiljanic et al. 2014), and GALAH (De Silva

et al. 2015), an unprecedented amount of observational data, often of exquisite quality, is available. In this thesis, we have presented the current largest available Li abundances of nearby FGK field stars using GALAH iDR3 data, covering from the Spite plateau exhibited by very metal-poor stars to the super-solar metallicity. The huge data set with well-determined stellar parameters and Li abundances challenge our understanding in not only stellar evolution, but also in Galactic chemical evolution. In order to fully understand the observed Li abundances, many theorists have made a lot of efforts to build a consistent stellar evolution model to explain the Li depletion from old (metal-poor stars at the Spite plateau) to young stars (main-sequence stars in young clusters) (e.g. Vauclair 1988; Pinsonneault et al. 1999; Théado & Vauclair 2001, 2003; Talon & Charbonnel 2005).

However, as more observational data become available and both the metal-rich and metal-poor tails of the stellar distribution function are further populated, more unexpected patterns in Li abundances become apparent. At extremely metal-poor regime ($[Fe/H] \lesssim -3$), Li abundances start to bend down and fall below the Spite plateau with a large dispersion (e.g. Sbordone et al. 2010; Meléndez et al. 2010; Bonifacio et al. 2015). A decreasing trend of Li for super-solar metallicity stars has been confirmed in many recent studies (e.g. Delgado Mena et al. 2015; Guiglion et al. 2016; Bensby & Lind 2018). It is thus clear that our understanding of Li depletion in stellar atmospheres is still far from complete. More data in both the metal-rich and metal-poor regimes (combined with accurate 1D/3D non-LTE methods; Sect. 5.2.1) will be needed to pin down the stellar and Galactic evolution of Li comprehensively.

5.2.3 Li-rich giant stars

Another Li puzzle under investigation concerns the existence of Li-rich giants. A number of Li-rich giants have been observed in both our Galaxy (Monaco et al. 2011; D'Orazi et al. 2015; Casey et al. 2016) and Local Group dwarf galaxies (Domínguez et al. 2004; Kirby & Cohen 2012). The high Li abundance ($A(Li) \gtrsim 2$) at the surface of those giant stars contradicts the expectations ($A(Li) \sim 1$ or even lower for massive stars) from canonical stellar evolution (Charbonnel & Zahn 2007), which implies that there could be another mechanism to produce or preserve their Li abundances. In brief, two scenario have been proposed : internal nucleosynthesis and mixing up to the surface (Cameron & Fowler 1971; Charbonnel & Balachandran 2000; Palacios et al. 2001) or external merge of massive planet/dwarf (Denissenkov & Weiss 2000; Carlberg et al. 2010). It will be interesting to address the Li-giant mystery using accurate 1D/3D non-LTE methods (Sect. 5.2.1), together with the extremely large set of high quality data from GALAH (Sect. 5.2.2).

First Author Publications

Gao, X., Lind, K., Amarsi, A. M., Buder, S., et al. (2018). The GALAH Survey: Verifying abundance trends in the open cluster M67 using non-LTE spectroscopy. MNRAS, 481:2666.
This publication was used in this thesis.

Gao, X. (in prep. a). (2019). Cosmological lithium preserved in the atmospheres of warm dwarf stars. Nature Astronomy.
This publication was used in this thesis.

Publications

Co-Author Publications

Buder, S., Asplund, M., Duong, L., **et al.** (2018), The GALAH Survey: second data release. MNRAS, 478:4513-4552.

References

Adibekyan, V. Z., Sousa, S. G., Santos, N. C., et al. 2012, A&A, 545, A32

Aguilera-Gómez, C., Ramírez, I., & Chanamé, J. 2018, A&A, 614, A55

Amarsi, A. M., & Asplund, M. 2017, MNRAS, 464, 264

Amarsi, A. M., Asplund, M., Collet, R., & Leenaarts, J. 2015, MNRAS, 454, L11

—. 2016a, MNRAS, 455, 3735

Amarsi, A. M., Lind, K., Asplund, M., Barklem, P. S., & Collet, R. 2016b, MNRAS, 463, 1518

Arnould, M., & Norgaard, H. 1975, A&A, 42, 55

Asplund, M. 2005, ARA&A, 43, 481

Asplund, M., Grevesse, N., Sauval, A. J., & Scott, P. 2009, ARA&A, 47, 481

Asplund, M., Lambert, D. L., Nissen, P. E., Primas, F., & Smith, V. V. 2006, ApJ, 644, 229

Asplund, M., Nordlund, Å., Trampedach, R., Allende Prieto, C., & Stein, R. F. 2000, A&A, 359, 729

Aver, E., Olive, K. A., & Skillman, E. D. 2015, , 2015, 011

Badnell, N. R. 2011, Computer Physics Communications, 182, 1528

Bailly, S., Jedamzik, K., & Moultaka, G. 2009, Phys. Rev. D, 80, 063509

Balachandran, S. 1995, ApJ, 446, 203

Balachandran, S. C., Mallik, S. V., & Lambert, D. L. 2011, MNRAS, 410, 2526

Bania, T. M., Rood, R. T., & Balser, D. S. 2002, Nature, 415, 54

REFERENCES

Barklem, P. S. 2016a, A&A Rev., 24, 9

—. 2016b, Phys. Rev. A, 93, 042705

Barklem, P. S., Belyaev, A. K., & Asplund, M. 2003, A&A, 409, L1

Barklem, P. S., Belyaev, A. K., Dickinson, A. S., & Gadéa, F. X. 2010, A&A, 519, A20

Barklem, P. S., Belyaev, A. K., Spielfiedel, A., Guitou, M., & Feautrier, N. 2012, A&A, 541, A80

Bautista, M. A. 1997, A&AS, 122, 167

Belyaev, A. K. 2013, A&A, 560, A60

Belyaev, A. K., & Barklem, P. S. 2003, Phys. Rev. A, 68, 062703

Belyaev, A. K., Yakovleva, S. A., & Barklem, P. S. 2014, A&A, 572, A103

Bensby, T., Feltzing, S., & Lundström, I. 2003, A&A, 410, 527

Bensby, T., Feltzing, S., & Oey, M. S. 2014, A&A, 562, A71

Bensby, T., & Lind, K. 2018, A&A, 615, A151

Bergemann, M., Collet, R., Amarsi, A. M., et al. 2017, ApJ, 847, 15

Berrington, K. A., Burke, P. G., Chang, J. J., et al. 1974, Computer Physics Communications, 8, 149

Bertelli Motta, C., Salaris, M., Pasquali, A., & Grebel, E. K. 2017, MNRAS, 466, 2161

Bertelli Motta, C., Pasquali, A., Richer, J., et al. 2018, MNRAS, 478, 425

Bland-Hawthorn, J., Karlsson, T., Sharma, S., Krumholz, M., & Silk, J. 2010, ApJ, 721, 582

Boesgaard, A. M. 1987, PASP, 99, 1067

Boesgaard, A. M., Budge, K. G., & Ramsay, M. E. 1988, ApJ, 327, 389

Boesgaard, A. M., & King, J. R. 2002, ApJ, 565, 587

Boesgaard, A. M., Lum, M. G., Deliyannis, C. P., et al. 2016, ApJ, 830, 49

Boesgaard, A. M., & Tripicco, M. J. 1986, ApJ, 302, L49

REFERENCES

Bonifacio, P., Caffau, E., Spite, M., et al. 2015, A&A, 579, A28

Brault, J., & Neckel, H. 1987, Tape copy from KIS IDL library

Bressan, A., Marigo, P., Girardi, L., et al. 2012, MNRAS, 427, 127

Brown, E. F., Bildsten, L., & Chang, P. 2002, ApJ, 574, 920

Brown, L., & Schramm, D. N. 1988, ApJ, 329, L103

Brown, T. M., Christensen-Dalsgaard, J., Dziembowski, W. A., et al. 1989, ApJ, 343, 526

Buder, S., Asplund, M., Duong, L., et al. 2018, MNRAS, 478, 4513

Buder, S., Lind, K., Ness, M. K., et al. 2019, A&A, 624, A19

Burke, P. G., Hibbert, A., & Robb, W. D. 1971, Journal of Physics B Atomic Molecular Physics, 4, 153

Burles, S., Nollett, K. M., & Turner, M. S. 2001, ApJ, 552, L1

Cameron, A. G. W., & Fowler, W. A. 1971, ApJ, 164, 111

Canto Martins, B. L., Lèbre, A., de Laverny, P., et al. 2006, A&A, 451, 993

Carlberg, J. K., Smith, V. V., Cunha, K., Majewski, S. R., & Rood, R. T. 2010, ApJ, 723, L103

Casey, A. R., Ruchti, G., Masseron, T., et al. 2016, MNRAS, 461, 3336

Castor, J. I. 2004, Radiation Hydrodynamics

Cayrel, R., Steffen, M., Chand, H., et al. 2007, A&A, 473, L37

Cescutti, G., & Molaro, P. 2019, MNRAS, 482, 4372

Chaboyer, B., Demarque, P., & Pinsonneault, M. H. 1995, ApJ, 441, 876

Chaboyer, B., & Zahn, J.-P. 1992, A&A, 253, 173

Chapman, S., & Cowling, T. G. 1970, The mathematical theory of non-uniform gases. an account of the kinetic theory of viscosity, thermal conduction and diffusion in gases

Charbonneau, P., & Michaud, G. 1988, ApJ, 334, 746

—. 1991, ApJ, 370, 693

REFERENCES

Charbonneau, P., Michaud, G., & Proffitt, C. R. 1989, ApJ, 347, 821

Charbonnel, C., & Balachandran, S. C. 2000, A&A, 359, 563

Charbonnel, C., & Talon, S. 2005a, Science, 309, 2189

Charbonnel, C., & Talon, S. 2005b, in EAS Publications Series, Vol. 17, EAS Publications Series, ed. G. Alecian, O. Richard, & S. Vauclair, 167–176

Charbonnel, C., & Talon, S. 2008, in IAU Symposium, Vol. 252, The Art of Modeling Stars in the 21st Century, ed. L. Deng & K. L. Chan, 163–174

Charbonnel, C., & Zahn, J. P. 2007, A&A, 467, L15

Chen, Y., Girardi, L., Bressan, A., et al. 2014, MNRAS, 444, 2525

Chen, Y. Q., Nissen, P. E., Benoni, T., & Zhao, G. 2001, A&A, 371, 943

Choi, J., Dotter, A., Conroy, C., et al. 2016, ApJ, 823, 102

Cooke, R. J., Pettini, M., & Steidel, C. C. 2018, ApJ, 855, 102

Couvidat, S., García, R. A., Turck-Chièze, S., et al. 2003, ApJ, 597, L77

Cyburt, R. H., Fields, B. D., Olive, K. A., & Yeh, T.-H. 2016, Reviews of Modern Physics, 88, 015004

Dalton, G., Trager, S. C., Abrams, D. C., et al. 2012, in Proc. SPIE, Vol. 8446, Ground-based and Airborne Instrumentation for Astronomy IV, 84460P

de Jong, R. S., Bellido-Tirado, O., Chiappini, C., et al. 2012, in Proc. SPIE, Vol. 8446, Ground-based and Airborne Instrumentation for Astronomy IV, 84460T

De Silva, G. M., Freeman, K. C., Asplund, M., et al. 2007, AJ, 133, 1161

De Silva, G. M., Freeman, K. C., & Bland-Hawthorn, J. 2009, , 26, 11

De Silva, G. M., Sneden, C., Paulson, D. B., et al. 2006, AJ, 131, 455

De Silva, G. M., Freeman, K. C., Bland-Hawthorn, J., et al. 2015, MNRAS, 449, 2604

Delgado Mena, E., Bertrán de Lis, S., Adibekyan, V. Z., et al. 2015, A&A, 576, A69

Deliyannis, C. P., Demarque, P., & Kawaler, S. D. 1990, ApJS, 73, 21

REFERENCES

Deliyannis, C. P., King, J. R., & Boesgaard, A. M. 1997, Astrophysics and Space Science Library, Vol. 212, Lithium in the Old Open Cluster M67: Constraints for the Cause of the Boesgaard li Gap, ed. E. Kontizas, M. Kontizas, D. H. Morgan, & G. P. Vettolani, 201

Denissenkov, P. A., & Weiss, A. 2000, A&A, 358, L49

Domínguez, I., Abia, C., Straniero, O., Cristallo, S., & Pavlenko, Y. V. 2004, A&A, 422, 1045

Domogatskii, G. V., Eramzhian, R. A., & Nadezhin, D. K. 1978, Ap&SS, 58, 273

D'Orazi, V., Gratton, R. G., Angelou, G. C., et al. 2015, ApJ, 801, L32

Dotter, A. 2016, ApJS, 222, 8

Dotter, A., Conroy, C., Cargile, P., & Asplund, M. 2017, ApJ, 840, 99

Drawin, H.-W. 1968, Zeitschrift fur Physik, 211, 404

Duong, L., Freeman, K. C., Asplund, M., et al. 2018, ArXiv e-prints, arXiv:1801.01514

Edvardsson, B., Andersen, J., Gustafsson, B., et al. 1993, A&A, 275, 101

Feng, Y., & Krumholz, M. R. 2014, Nature, 513, 523

François, P., Pasquini, L., Biazzo, K., Bonifacio, P., & Palsa, R. 2013, A&A, 552, A136

Freeman, K., & Bland-Hawthorn, J. 2002, ARA&A, 40, 487

Friel, E. D., Jacobson, H. R., & Pilachowski, C. A. 2010, AJ, 139, 1942

Fu, X., Romano, D., Bragaglia, A., et al. 2018, A&A, 610, A38

Fuhrmann, K. 2004, Astronomische Nachrichten, 325, 3

Gaia Collaboration, Prusti, T., de Bruijne, J. H. J., et al. 2016, A&A, 595, A1

Gao, X., Lind, K., Amarsi, A. M., et al. 2018, MNRAS, 481, 2666

Garaud, P. 2002, MNRAS, 335, 707

García, R. A., Turck-Chièze, S., Jiménez-Reyes, S. J., et al. 2007, Science, 316, 1591

REFERENCES

Garcia Lopez, R. J., & Spruit, H. C. 1991, ApJ, 377, 268

García Pérez, A. E., Asplund, M., Primas, F., Nissen, P. E., & Gustafsson, B. 2006, A&A, 451, 621

Geller, A. M., Latham, D. W., & Mathieu, R. D. 2015, AJ, 150, 97

Gilmore, G., Randich, S., Asplund, M., et al. 2012, The Messenger, 147, 25

Gray, D. F. 2005, The Observation and Analysis of Stellar Photospheres

Grevesse, N., Asplund, M., & Sauval, A. J. 2007, Space Sci. Rev., 130, 105

Grisoni, V., Matteucci, F., Romano, D., & Fu, X. 2019, MNRAS, 489, 3539

Gruyters, P., Nordlander, T., & Korn, A. J. 2014, A&A, 567, A72

Gruyters, P., Lind, K., Richard, O., et al. 2016, A&A, 589, A61

Guiglion, G., de Laverny, P., Recio-Blanco, A., et al. 2016, A&A, 595, A18

Gustafsson, B., Church, R. P., Davies, M. B., & Rickman, H. 2016, A&A, 593, A85

Gustafsson, B., Edvardsson, B., Eriksson, K., et al. 2008, A&A, 486, 951

Hinshaw, G., Larson, D., Komatsu, E., et al. 2013, ApJS, 208, 19

Hobbs, L. M., & Thorburn, J. A. 1991, AJ, 102, 1070

Holder, G. P., Nollett, K. M., & van Engelen, A. e. 2010, ApJ, 716, 907

Holtzman, J. A., Shetrone, M., Johnson, J. A., et al. 2015, AJ, 150, 148

Howk, J. C., Lehner, N., Fields, B. D., & Mathews, G. J. 2012, Nature, 489, 121

Hubeny, I., & Mihalas, D. 2014, Theory of stellar atmospheres: an introduction to astrophysical non-equilibrium quantitative spectroscopic analysis, Vol. 26 (Princeton University Press)

Izzo, L., Della Valle, M., Mason, E., et al. 2015, ApJ, 808, L14

Jørgensen, B. R., & Lindegren, L. 2005, A&A, 436, 127

Kawata, D., & Chiappini, C. 2016, Astronomische Nachrichten, 337, 976

Kirby, E. N., & Cohen, J. G. 2012, AJ, 144, 168

REFERENCES

Kiselman, D. 1993, A&A, 275

Korn, A. J., Grundahl, F., Richard, O., et al. 2007, ApJ, 671, 402

Kos, J., Lin, J., Zwitter, T., et al. 2017, MNRAS, 464, 1259

Kos, J., Bland-Hawthorn, J., Freeman, K., et al. 2018, MNRAS, 473, 4612

Kumar, P., & Quataert, E. J. 1997, ApJ, 475, L143

Kunder, A., Kordopatis, G., Steinmetz, M., et al. 2017, AJ, 153, 75

Kurucz, R. L. 1970, SAO Special Report, 309

Kurucz, R. L. 1995, in Astronomical Society of the Pacific Conference Series, Vol. 78, Astrophysical Applications of Powerful New Databases, ed. S. J. Adelman & W. L. Wiese, 205

Lambert, D. L. 1993, Physica Scripta Volume T, 47, 186

Lambert, D. L., Heath, J. E., & Edvardsson, B. 1991, MNRAS, 253, 610

Lambert, D. L., & Reddy, B. E. 2004, MNRAS, 349, 757

Lewis, I. J., Cannon, R. D., Taylor, K., et al. 2002, MNRAS, 333, 279

Lin, J., Dotter, A., Ting, Y.-S., & Asplund, M. 2018, MNRAS, 477, 2966

Lind, K., Asplund, M., & Barklem, P. S. 2009a, A&A, 503, 541

Lind, K., Asplund, M., Barklem, P. S., & Belyaev, A. K. 2011, A&A, 528, A103

Lind, K., Bergemann, M., & Asplund, M. 2012, MNRAS, 427, 50

Lind, K., Melendez, J., Asplund, M., Collet, R., & Magic, Z. 2013, A&A, 554, A96

Lind, K., Primas, F., Charbonnel, C., Grundahl, F., & Asplund, M. 2009b, A&A, 503, 545

Lindegren, L., Hernández, J., Bombrun, A., et al. 2018, A&A, 616, A2

Lodders, K., Palme, H., & Gail, H.-P. 2009, Landolt Börnstein, 712

Maaten, L. v. d., & Hinton, G. 2008, Journal of machine learning research, 9, 2579

MacLean, B. T., De Silva, G. M., & Lattanzio, J. 2015, MNRAS, 446, 3556

Magrini, L., Randich, S., Romano, D., et al. 2014, A&A, 563, A44

REFERENCES

Majewski, S. R., Schiavon, R. P., Frinchaboy, P. M., et al. 2017, AJ, 154, 94

Martell, S. L., Sharma, S., Buder, S., et al. 2017, MNRAS, 465, 3203

Martin, A. J., Stift, M. J., Fossati, L., et al. 2017, MNRAS, 466, 613

Mathieu, R. D., Latham, D. W., & Griffin, R. F. 1990, AJ, 100, 1859

Maxted, P. F. L., Serenelli, A. M., & Southworth, J. 2015, A&A, 577, A90

Meléndez, J., Casagrande, L., Ramírez, I., Asplund, M., & Schuster, W. J. 2010, A&A, 515, L3

Michaud, G. 1970, ApJ, 160, 641

—. 1977, Nature, 266, 433

—. 1986, ApJ, 302, 650

Michaud, G., Alecian, G., & Richer, J. 2015, Atomic Diffusion in Stars, doi:10.1007/978-3-319-19854-5

Michaud, G., & Charbonneau, P. 1991, Space Sci. Rev., 57, 1

Michaud, G., Fontaine, G., & Beaudet, G. 1984, ApJ, 282, 206

Michaud, G., & Proffitt, C. R. 1993, in Astronomical Society of the Pacific Conference Series, Vol. 40, IAU Colloq. 137: Inside the Stars, ed. W. W. Weiss & A. Baglin, 246–259

Michaud, G., Richard, O., Richer, J., & VandenBerg, D. A. 2004, ApJ, 606, 452

Mihalas, D. 1978, Stellar atmospheres

Mihalas, D., & Mihalas, B. W. 1984, Foundations of radiation hydrodynamics

Monaco, L., Villanova, S., Moni Bidin, C., et al. 2011, A&A, 529, A90

Nomoto, K., Kobayashi, C., & Tominaga, N. 2013, ARA&A, 51, 457

Nordlander, T., Korn, A. J., Richard, O., & Lind, K. 2012, ApJ, 753, 48

Nordlander, T., & Lind, K. 2017, ArXiv e-prints, arXiv:1708.01949

Önehag, A., Gustafsson, B., & Korn, A. 2014, A&A, 562, A102

Önehag, A., Korn, A., Gustafsson, B., Stempels, E., & Vandenberg, D. A. 2011, A&A, 528, A85

REFERENCES

Osorio, Y., & Barklem, P. S. 2016, A&A, 586, A120

Osorio, Y., Barklem, P. S., Lind, K., et al. 2015, A&A, 579, A53

Pace, G., Castro, M., Meléndez, J., Théado, S., & do Nascimento, Jr., J.-D. 2012, A&A, 541, A150

Pace, G., Pasquini, L., & François, P. 2008, A&A, 489, 403

Palacios, A., Charbonnel, C., & Forestini, M. 2001, A&A, 375, L9

Palacios, A., Talon, S., Charbonnel, C., & Forestini, M. 2003, A&A, 399, 603

Pancino, E., Carrera, R., Rossetti, E., & Gallart, C. 2010, A&A, 511, A56

Paquette, C., Pelletier, C., Fontaine, G., & Michaud, G. 1986, ApJS, 61, 197

Pasquini, L., Biazzo, K., Bonifacio, P., Randich, S., & Bedin, L. R. 2008, A&A, 489, 677

Peach, G., Saraph, H. E., & Seaton, M. J. 1988, Journal of Physics B Atomic Molecular Physics, 21, 3669

Pichardo, B., Moreno, E., Allen, C., et al. 2012, AJ, 143, 73

Pinsonneault, M. 1997, ARA&A, 35, 557

Pinsonneault, M. H. 1995, in Liege International Astrophysical Colloquia, Vol. 32, Liege International Astrophysical Colloquia, 65

Pinsonneault, M. H. 2010, in IAU Symposium, Vol. 268, Light Elements in the Universe, ed. C. Charbonnel, M. Tosi, F. Primas, & C. Chiappini, 375–380

Pinsonneault, M. H., Kawaler, S. D., Sofia, S., & Demarque, P. 1989, ApJ, 338, 424

Pinsonneault, M. H., Walker, T. P., Steigman, G., & Narayanan, V. K. 1999, ApJ, 527, 180

Piskunov, N., & Valenti, J. A. 2017, A&A, 597, A16

Pitrou, C., Coc, A., Uzan, J.-P., & Vangioni, E. 2018, Phys. Rep., 754, 1

Pospelov, M., & Pradler, J. 2010, Annual Review of Nuclear and Particle Science, 60, 539

Prantzos, N. 2012, A&A, 542, A67

REFERENCES

Prantzos, N., Casse, M., & Vangioni-Flam, E. 1993, ApJ, 403, 630

Prantzos, N., & Charbonnel, C. 2006, A&A, 458, 135

Prantzos, N., de Laverny, P., Guiglion, G., Recio-Blanco, A., & Worley, C. C. 2017, A&A, 606, A132

Press, W. H. 1981, ApJ, 245, 286

Prieto, C. A. 2016, Living Reviews in Solar Physics, 13, 1

Proffitt, C. R. 1994, ApJ, 425, 849

Proffitt, C. R., & Michaud, G. 1991, ApJ, 380, 238

Ramírez, I., Fish, J. R., Lambert, D. L., & Allende Prieto, C. 2012, ApJ, 756, 46

Randich, S., Gratton, R., Pallavicini, R., Pasquini, L., & Carretta, E. 1999, A&A, 348, 487

Randich, S., Sestito, P., Primas, F., Pallavicini, R., & Pasquini, L. 2006, A&A, 450, 557

Reader, J., Kramida, A., & Ralchenko, Y. 2012, in American Astronomical Society Meeting Abstracts, Vol. 219, American Astronomical Society Meeting Abstracts #219, 443.01

Recio-Blanco, A., de Laverny, P., Kordopatis, G., et al. 2014, A&A, 567, A5

Reeves, H., Fowler, W. A., & Hoyle, F. 1970, Nature, 226, 727

Richer, J., & Michaud, G. 1993, ApJ, 416, 312

Richer, J., Michaud, G., Rogers, F., et al. 1998, ApJ, 492, 833

Romano, D., Matteucci, F., Molaro, P., & Bonifacio, P. 1999, A&A, 352, 117

Romano, D., Matteucci, F., Ventura, P., & D'Antona, F. 2001, A&A, 374, 646

Sackmann, I.-J., & Boothroyd, A. I. 1992, ApJ, 392, L71

—. 1999, ApJ, 510, 217

Sanders, W. L. 1977, A&AS, 27, 89

Sarajedini, A., Dotter, A., & Kirkpatrick, A. 2009, ApJ, 698, 1872

Sbordone, L., Bonifacio, P., Caffau, E., et al. 2010, A&A, 522, A26

REFERENCES

Schatzman, E. 1969, A&A, 3, 331

—. 1993, A&A, 279, 431

Schuler, S. C., King, J. R., & The, L.-S. 2009, ApJ, 701, 837

Scott, P., Asplund, M., Grevesse, N., Bergemann, M., & Sauval, A. J. 2015a, A&A, 573, A26

Scott, P., Grevesse, N., Asplund, M., et al. 2015b, A&A, 573, A25

Sestito, P., & Randich, S. 2005, A&A, 442, 615

Sharma, S., Stello, D., Buder, S., et al. 2017, Monthly Notices of the Royal Astronomical Society, 473, 2004

Sharma, S., Stello, D., Buder, S., et al. 2017, ArXiv e-prints, arXiv:1707.05753

Sharma, S., Stello, D., Bland-Hawthorn, J., et al. 2019, arXiv e-prints, arXiv:1904.12444

Sheinis, A., Anguiano, B., Asplund, M., et al. 2015, Journal of Astronomical Telescopes, Instruments, and Systems, 1, 035002

Skrutskie, M. F., Cutri, R. M., Stiening, R., et al. 2006, AJ, 131, 1163

Smiljanic, R., Korn, A. J., Bergemann, M., et al. 2014, A&A, 570, A122

Smiljanic, R., Romano, D., Bragaglia, A., et al. 2016, A&A, 589, A115

Soderblom, D. R. 2010, ARA&A, 48, 581

Souto, D., Cunha, K., Smith, V. V., et al. 2018, ApJ, 857, 14

Spite, F., & Spite, M. 1982, A&A, 115, 357

Spite, M., Spite, F., & Bonifacio, P. 2012, Memorie della Societa Astronomica Italiana Supplementi, 22, 9

Spite, M., Spite, F., Caffau, E., & Bonifacio, P. 2015, A&A, 582, A74

Starrfield, S., Truran, J. W., Sparks, W. M., & Arnould, M. 1978, ApJ, 222, 600

Steenbock, W., & Holweger, H. 1984, A&A, 130, 319

Tajitsu, A., Sadakane, K., Naito, H., Arai, A., & Aoki, W. 2015, Nature, 518, 381

Tajitsu, A., Sadakane, K., Naito, H., et al. 2016, ApJ, 818, 191

REFERENCES

Takeda, Y. 2003, A&A, 402, 343

Talon, S., & Charbonnel, C. 1998, A&A, 335, 959

—. 2003, A&A, 405, 1025

—. 2004, A&A, 418, 1051

—. 2005, A&A, 440, 981

Talon, S., & Charbonnel, C. 2010, in IAU Symposium, Vol. 268, Light Elements in the Universe, ed. C. Charbonnel, M. Tosi, F. Primas, & C. Chiappini, 365–374

Talon, S., Kumar, P., & Zahn, J.-P. 2002, ApJ, 574, L175

Tang, J., Bressan, A., Rosenfield, P., et al. 2014, MNRAS, 445, 4287

Tassoul, J.-L. 2000, Stellar Rotation

Tassoul, J.-L., & Tassoul, M. 1982, ApJS, 49, 317

Tautvaišiene, G., Edvardsson, B., Tuominen, I., & Ilyin, I. 2000, A&A, 360, 499

Théado, S., & Vauclair, S. 2001, A&A, 375, 70

—. 2003, ApJ, 587, 795

Thoul, A. A., Bahcall, J. N., & Loeb, A. 1994, ApJ, 421, 828

Travaglio, C., Gallino, R., Busso, M., & Gratton, R. 2001, ApJ, 549, 346

Turcotte, S., Richer, J., Michaud, G., Iglesias, C. A., & Rogers, F. J. 1998, ApJ, 504, 539

van Regemorter, H. 1962, ApJ, 136, 906

Vauclair, S. 1988, ApJ, 335, 971

Venn, K. A., & Hill, V. M. 2008, The Messenger, 134, 23

Villanova, S., Carraro, G., & Saviane, I. 2009, A&A, 504, 845

Wallerstein, G., Herbig, G. H., & Conti, P. S. 1965, ApJ, 141, 610

Wenger, M., Ochsenbein, F., Egret, D., et al. 2000, A&AS, 143, 9

Wittenmyer, R. A., Sharma, S., Stello, D., et al. 2017, ArXiv e-prints, arXiv:1712.06774

REFERENCES

Yadav, R. K. S., Bedin, L. R., Piotto, G., et al. 2008, A&A, 484, 609

Yakut, K., Zima, W., Kalomeni, B., et al. 2009, A&A, 503, 165

Yong, D., Carney, B. W., & Teixera de Almeida, M. L. 2005, AJ, 130, 597

Zahn, J.-P. 1992, A&A, 265, 115